Stony Brook University

Templating Biomineralization: Surface Directed Protein Self-assembly and External Magnetic Field Stimulation of Osteoblasts

A Dissertation Presented

by

Xiaolan Ba

to

The Graduate School

in Partial Fulfillment of the

Requirements

for the Degree of

Doctor of Philosophy

in

Materials Science and Engineering

Stony Brook University

May 2011

Stony Brook University

The Graduate School

Xiaolan Ba

We, the dissertation committee for the above candidate for
the Doctor of Philosophy degree, hereby recommend
acceptance of this dissertation.

Miriam H. Rafailovich - Dissertation Advisor
Professor, Department of Materials Science and Engineering

Jonathan C. Sokolov - Chairperson of Defense
Professor, Department of Materials Science and Engineering

Yizhi Meng
Assistant Professor, Department of Materials Science and Engineering

Michael Hadjiargyrou
Associate Professor, Department of Biomedical Engineering

This dissertation is accepted by the Graduate School.

Lawrence Martin
Dean of the Graduate School

Abstract of the Dissertation

Templating Biomineralization: Surface Directed Protein Self-assembly and External Magnetic Field Stimulation of Osteoblasts

by

Xiaolan Ba

Doctor of Philosophy

in

Materials Science and Engineering

Stony Brook University

2011

Biomineralization is a wide-spread phenomenon in the biological systems, which is the process of mineral formation by organisms through interaction between its organic contents and the inorganic minerals. The process is essential in a broad spectrum of biological phenomena ranging from bone and tooth formation to pathological mineralization under hypoxic conditions or cancerous formations. In this thesis I studied biomineralization at the earliest stages in order to obtain a better understanding of the fundamental principals involved. This knowledge is essential if we want to engineer devices which will increase bone regeneration or prevent unwanted mineral deposits.

Extracellular matrix (ECM) proteins play an essential role during biomineralization in bone and engineered tissues. In this dissertation, I present an approach to mimic the ECM in vitro to probe the interactions of these proteins with calcium phosphate mineral and with each other. Early stage of mineralization is investigated by mechanical properties of the protein fibers using Scanning Probe Microscopy (SPM) and Shear Modulation Force Microscopy (SMFM). The development of mineral crystals on the protein matrices is also characterized by Scanning Electron Microscopy (SEM), Transmission Electron Microscopy (TEM) and Grazing Incidence X-ray Diffraction (GIXRD). The results demonstrate complementary actions of the two ECM proteins to collect cations and template calcium phosphate mineral, respectively.

Magnets have been clinically used as an "induction source" in various bone or orthodontic treatments. However, the mechanism and effects of magnetic fields remain unclear. In this dissertation, I also undertake the present investigation to study the effects of 150 mT static magnetic fields (SMF) on ECM development and cell biomineralization using MC3T3-E1 osteobalst-like cells. Early stage of biomineralization is characterized by SPM, SMFM and confocal laser scanning microscopy (CSLM). Late stage of biomineralization is investigated by SEM, GIXRD and energy dispersive X-ray spectroscopy (EDXS). Gene expression during the exposure of SMF is also studies by RT-PCR. The results indicated that exposure to SMF induces osteoblasts to produce larger quantities of HA, with higher degree of crystalline order.

The controlling and understanding of protein on the surface is of great interest in biomedical application such as implant medicine, biosensor design, food processing, and chromatographic separations. The adsorbed protein onto the surface significantly determines the performance of biomaterials in a biological environment. Recent studies have suggested that the preservation of the native secondary structure of protein adsorbed is essential for biological

application. In order to manipulate protein adsorption and design biocompatible materials, the mechanisms underlying protein-surface interactions, especially how surface properties of materials induce conformational changes of adsorbed proteins, needs to be well understood. Here we demonstrated that even though SPS is a necessary condition, it is not sufficient. We show that low substrate conductivity as well as proper salt concentration are also critical in sustained protein adsorption continuously. These factors allow one to pattern regions of different conducting properties and for the first time patterns physiologically relevant protein structures. Here we show that we can achieve patterned biomineralized regimes, both with plasma proteins in a simple and robust manner without additional functionalization or application of electrochemical gradients. Since the data indicate that the patterns just need to differ in electrical conductivity, rather than surface chemistry, we propose that the creation of transient image charges, due to incomplete charge screening, may be responsible for sustain the driving force for continual protein absorption.

Dedicated to

My Beloved Father and Mother

and

My family

Table of Contents

List of Tables

List of Figures

List of Abbreviations:

ALP: alkaline phosphatase

BCA: bicinchoninic acid

CLSM: confocal laser scanning microscopy

COL: type I collagen

COL-EL: mixture of type I collagen and elastin

COL-FN: mixture of type I collagen and fibronectin

ECM: extracellular matrix

EL: elastin

FN: fibronectin

FN-EL: mixture of fibronectin and elastin

FTIR: fourier-transformed Infrared Microscopy

GIXD: grazing incidence X-ray microscopy

HAP: hydroxyapatite

OC: osteocalcin

RT-PCR: real-time polymerase chain reaction

SEM: scanning electron microscopy

SMF: static magnetic field

SMFM: shear modulation force microscopy

SPM: scanning probe microscopy

SPS: sulfonated polystyrene

STXM: scanning transmission X-ray microscopy

TEM: transmission electron microscopy

XANES: X-ray absorption near edge structure

Acknowledgement

I would like to thank many people for their contribution to this work and for making my stay at Stony Brook University a very positive experience.

Firstly, I would like to extend my sincere gratitude to my advisor, Dr. Miriam H. Rafailovich. Dr. Rafailovich has been an inspiration for me both intellectually and personally. Her creativity, sharp intellect and persistence have provided me with numerous challenges, some of which I was able to rise to, but all of which resulted in personal growth and took me to a higher level of thought. Her many suggestions for my project forced me to clarify my thoughts and present them in a logical sequence.

Sincere thanks are due to Dr. Michael Hadjiargyrou, Dr. Yizhi Meng and Dr. John Sokolov for serving on my defense committee and for their valuable comments and suggestions on my dissertation.

I would like to thank Dr. Elaine DiMasi, Dr. Yizhi Meng, Dr. Marcia Simon, Dr. Nadine Pernodet, Dr. Seo-Young Kwak and Dr. Helga Füredi-Milhofer to help me develop my mind and give many valuable suggestions when I faced with difficulties during my research. I would like to thank Dr. Jim Quinn for his generous help in times of need and emergencies related to laboratory equipments. I feel grateful for the help from Dr. Lisa Miller, Dr. Randy Smith and Dr. Megan Bourassa with the FTIR equipment at NSLS at the Brookhaven National Laboratory (BNL), and the help from Dr. Aaron Stein, Dr. Fernando Camino and Dr. Don Elliott with many

facilities and Dr. Lihua Zhang with high resolution TEM in the Center of Functional Nanomaterials (CFN).

Thanks are owed to all my friends and colleagues in my lab who were and are here when I arrived at Stony Brook. They provided a friendly and entertaining environment that I have done my work here very happily. They also provided hours of assistance for any number of things I learned these years. Special thanks to Debby and Lynn for providing me all the academic and research-related help throughout my study.

Lastly and most importantly, I would like to thank my family. My husband and parents have been constantly support and encourage me to pursue this research.

This work is kindly supported by NSF-MRSEC Program (DMR0606387), the Brookhaven National Laboratory-Stony Brook University Seed Grand Program and NIH program (R01 AR52379 & R01 AR49286). Research carried out in part at the Center for Functional Nanomaterials and National Synchrotron Light Source, Brookhaven National Laboratory, which is supported under USDOE Contract DE-AC02-98CH10886.

Chapter 1

Introduction

1.1 Background

Modern medicine uses a variety of synthetic materials and devices to treat medical conditions and diseases. Biomedical devices such as coronary stents, vascular grafts, heart valves, blood bags, blood oxygenators, renal dialyzers, catheters, hip prostheses, knee prostheses, intraocular lenses, contact lenses, cochlear implants, and dental implants have definitely played an important role in transforming lives and improving the quality of living. Advances in protein-based drugs, gene therapy, targeted drug delivery, and tissue engineering have the potential to revolutionize contemporary medicine. Thus, a wide range of synthetic materials are used to evaluate, treat, augment or replace any tissue, organ or function of the body. "Biomaterial" is a term used to categorize such materials and devices that directly "interact" with human tissues and organs [1]. The interactions may involve, for example, platelet aggregation and blood coagulation in the case of blood-contacting devices, immune response and foreign body reactions around biomaterials or devices implanted in the body, or more desirably, structural and functional connection between the implant and the host tissue which is termed osteointegration in the case of dental and bone implants.

Biomaterials interact with biological systems through their surfaces. It is, therefore, vitally important to control the surface properties of a biomaterial so that it integrates well with host tissues - that is, to make the material "biocompatible" [2]. Organic thin films and coatings, particularly those of polymers, are very attractive as biomaterial coatings because they offer great versatility in the chemical groups that can be incorporated at the surface (to control tissue – biomaterial interactions); the coatings also have mechanical properties that are similar to soft biological tissues. The relative ease of processing is another reason for the extensive interest in organic thin films. Biomaterial surfaces can be coated with polymers using simple techniques such as dip-coating, spray-coating, spin-coating, or solvent-casting. Coating techniques involving the chemical grafting of molecules onto the biomaterial surface are also available. Ultra-thin coatings based on self-assembled monolayer s(SAMs), surface-tethered polymers (polymer brushes), or multilayer coatings based on layer-by-layer assembly offer precise control on the location and orientation of chemical groups and biomolecules on the surface of the coating.

Polymer thin films and coatings have a lot of potential biomedical applications. Three main areas are as following: (I) biocompatible coatings for implants (e.g., protein - repellant coatings, antithrombogenic coatings that can prevent blood coagulation around implants, and antibacterial coatings); (II) polymer thin films for tissue engineering; and (III) polymer thin films for drug delivery and gene therapy. In this disertation, emphasis will be placed on the material and processing aspects of the coating, the physic-chemical properties of the coating, and its protein-adsorption and cell-adhesion characteristics in biomimic mineralization *in vitro*.

Polyelectrolyte thin films have been widely explored as functional coating in numerous applications, particularly those involving biomimetic membrane [3, 4], gene/drug delivery [5-7]

and cell adhesion for biomedical applications [8-10]. A variety of external parameters, such as salt concentration, pH and temperature of the subphase and the nature of the absorbing substrate are important for controlling and tuning characteristics of polyelectrolyte. The different characteristics of polyelectrolyte thin films on various surfaces have been reported [11-14]. Especially, the highly charged polyelectrolyte has been extensively studied due to less protein-resistant than uncharged hydrophilic coatings [15]. Here we will highlight sulfonated polystyrene (SPS) thin film with negative charge that have been used to control protein adsorption and cell adhesion onto the substrates we are going to used for our study. In the previous study of our group, Pernodet et al [16] demonstrated that fibronectin undergoes a transition from monolayer to multilayer adsorption with the spontaneous formation of a fibrillar networks at calculated surface charge densities above 0.03 coulombs/m^2 using different sulfonated polystyrene surfaces shown in Fig 1.1. They proposed that the polarization of charge domains on the polyampholytic fibronectin molecules near high charge density surfaces is sufficient to initiate the multilayer adsorption and unfold the protein chain to induce the fibrillogenesis shown in Fig 1.2. Moreover, Meng et al [17] observed the similar networks induced by the presence of MC3T3-E1 cells when the surface charge densities initiating the extracellular matrix (ECM) network formation are comparable to the surface charge density of cell surfaces. Those observations suggest that control of the surface charge density of biomaterials could play a critical role in regulating ECM self-organization, thereby permitting the biomimetic formation of matrices appropriate for directing cell differentiation and tissue development, a critical step in tissue engineering.

1.2 Templating Biomineralization

Biomineralization is a wide-spread phenomenon in the biological systems, which refers to the process of mineral formation by organisms through interactions between its organic

contents and the inorganic minerals [18]. Many organisms have developed sophisticated strategies for directing the growth of the inorganic constituents of their mineralized tissues. Active control mechanisms are effective at almost all levels of structural hierarchy, ranging from the nanoscopic regime - the nucleation of a crystallite at a specific site - up to the macroscopic regime, where the biophysical properties of the mineralized tissue are matched to certain function [19]. ECM plays an important role during biomineralization, which can control the size, shape and composition of minerals. This process is often referred as "templating", but this term has become generic, denoting various proposed mineral-organic interactions including both chemical and structural affinities [20].

The controlled nucleation and growth of crystals from organic templates has been demonstrated by *in vitro* experiments [21-23] and in a number of natural biomineralizating systems [24, 25]. These studies on template crystal growth suggest that nucleation occurs on surfaces which expose repetitive patterns of anionic groups. These anionic groups tend to concentrate the inorganic cations creating local supersaturation followed by oriented nucleation of the crystal. To template the biomimic mineralization *in vitro*, many groups have investigated the preparation of biomimic systems with the use of organic substrates such as Langmuir monolayer/self-assembled monolayer with different functional groups [26-28], hydrogel membrane [29] or biomolecules [30-32]. Self-assembled monolayers functionalized with moieties specific to certain proteins have been shown to control crystallization parameters such as crystallographic polymorphism, nucleation density, orientation, and localization [33-36]. And some studies [37-40] show a similar correlation between the crystallographic orientations of hydroxyapatite when the organic scaffold is made from reconstituted collagen. However, none of

these surfaces imitate the highly organized fibrillar structure characteristic of the ECM. We need to develop a novel way to biomimic mineralization *in vitro* using self-assembled protein fibers.

1.3 Objectives and organization

Although many literatures have demonstrated the ability of extracellular matrix proteins to control the nucleation of minerals during the biomineralization, few studies compare the mechanical properties of different extracellular matrix protein fibers during the early-stage mineralization and reveal their different functions during the control of the nucleation and growth of minerals in the late-stage mineralization. And also it has been know well that the actual cellular ECM fibers are composed of a combination of proteins, primarily Type I collagen and specialized non-collagenous proteins such as fibronectin, elastin and so on. Type I Collagen plays the largest role in biomineralization and gives bone its structure and strength. Elastin, a much softer material, functions more to promote flexibility, and is not as crucial to biomineralization. Fibronectin, an adhesive protein, is conducive to biomineralization but does not induce mineralization as quickly. It requires us to find the fundamental understanding of the biomineralization process when different extracellular matrix proteins combine. In this study, we used those different proteins and combined protein mixtures on the SPS-coated silicon substrates to follow the biomineralization process. The mechanical properties of extracellular matrix protein fibers during early-stage biomineralization process was characterized using atomic force microscopy (AFM) and shear modulation force microscopy (SMFM) which are demonstrated as the sensitive instruments to characterize the elastic properties of the soft-material surface [41].

This dissertation is organized into an introductory chapter and five main chapters as following.

In chapter 2, I follow calcium phosphate mineralization on protein fibers self-assembled *in vitro* from solutions of fibronectin, elastin and their mixture. We probe the surface morphology and mechanical properties of the protein fibers during the early stages. The development of mineral crystals on the protein matrices is also investigated. In physiological mineralization solution, the elastic modulus of the fibers in the fibronectin-elastin mixture increases to a greater extent than that of the fibers from either pure protein. In the presence of fibronectin, longer exposure in the mineral solution leads to the formation of amorphous calcium phosphate particles templated along the self-assembled fibers, while elastin fibers only collect calcium without any mineral observed during early stage. TEM images confirm that small needle-shape crystals are confined inside elastin fibers which suppress the release of mineral outside the fibers during late stage, while hydroxyapatite crystals form when fibronectin is present. The results demonstrate complementary actions of the two ECM proteins fibronectin and elastin to collect cations and template mineral, respectively.

In chapter 3, further STXM and XANES study of biomineralized protein fibers were investigated. Here we demonstrate the capacity of STXM for characterizing directly both the organic content of protein fibers and the mineral at the same time using C K-edge and Ca L-edge absorption. The objective of this study is to determine if spectroscopic signature for mineralized protein fibers can be used to decipher the nature of protein fibers and minerals deposited on the protein fibers.

In chapter 4, the effects of the components of extracellular matrix on the bone formation and the kinetics of crystal growth of calcium phosphate were under investigation. In this study, I reported a method to investigate the role of Type I collagen and the interactions with other ECM proteins such as fibronectin and elastin during biomimic mineralization process *in vitro*. The

early stage of mineralization was characterized by scanning probe microscopy (SPM) and shear modulation force microscopy (SMFM). The late stage of mineralization was investigated by synchrotron grazing incident x-ray diffraction (GIXD) and scanning electron microscopy (SEM). The results demonstrate the cooperative interaction between type I collagen and noncollagenous proteins such as fibronectin or elastin could be essential for the biomineralization.

In chapter 5, I focus on the investigation to study the effects of static magnetic fields (SMF) on extracellular matrix (ECM) development and cell biomineralization on negatively charged polymer thin film. In this *in vitro* study, MC3T3-E1 osteoblast-like cells were exposed to 150 mT SMF in a vertical direction to the dish for up to 28 days. The effects of SMF on cell morphology, proliferation and orientation were characterized by confocal laser scanning microscopy (CSLM). To monitor the subtle changes of cells and ECM protein fibers during the initial stage of biomineralization, SPM and SMFM were used to characterize the morphology and mechanical property. The late-stage of mineralization was characterized by SEM and GIXD. The results show that in the presence of the SMF the modulii of the osteoblasts is higher, than the modulii of cells not exposed to the SMF. GIXD indicates that more biomineralized products are produced in the culture exposed to SMF. The results are consistent with proposed SMF therapies for bone healing.

In the final chapter (Chapter 6), I focus on the controlling protein absorption onto the surface using conductivity of substrates. In our previous work [16], we demonstrated that SPS is a necessary condition for the protein adsorption. However it is not sufficient. Here we show that low substrate conductivity as well as proper salt concentration is also critical in sustained protein adsorption continuously. The morphology of absorbed protein was imaged by SPM and the amount of absorbed protein was quantified by BCA ELISA assay. The results show that the

absorbed amount of FN is increasing with increasing of conductivity while the FN mass is decreasing with increasing of contour ion concentration. These factors allow one to pattern regions of different conducting properties and for the first time patterns physiologically relevant protein structures. Here we show that we can achieve patterned proteins in a simple and robust manner without additional fictionalization or application of electrochemical gradients. Since the data indicate that the patterns just need to differ in electrical conductivity, rather than surface chemistry, we propose that the creation of transient image charges, due to incomplete charge screening, may be responsible for sustain the driving force for continual protein absorption.

Figures:

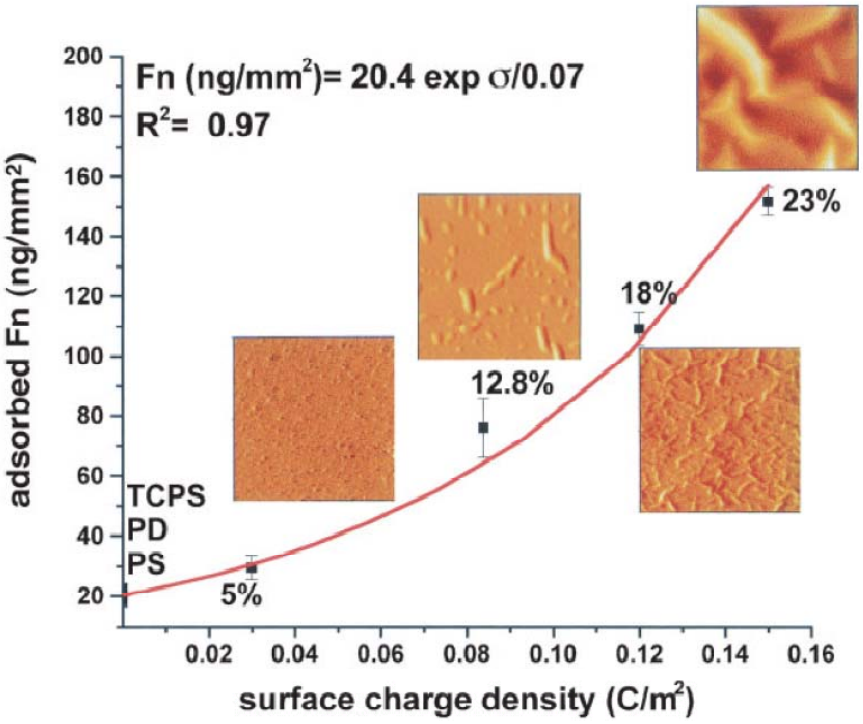

Figure 1.1 Adsorbed fibronectin morphology as a function of surface charge density. after 70 h of incubation with a 100 μg/mL Fn/PBS solution at 37°C, 100% humidity: (a) 0.03 C/m^2 surfaces demonstrate a thin globular layer of protein with peak heights of 80 nm; (b) −0.08 C/m^2 surfaces demonstrate a fusion of adsorbed protein globules achieving peak heights of 150 nm; (c) −0.12 C/m^2 surfaces demonstrate the initiation of fibril formation with peak heights of 280 nm; and (d) −0.15 C/m^2 surfaces demonstrate an extensive Fn network with peak heights reaching 1400 nm. Surfaces were imaged by contact mode AFM in PBS solution; each image is 20 × 20 μm. [16]

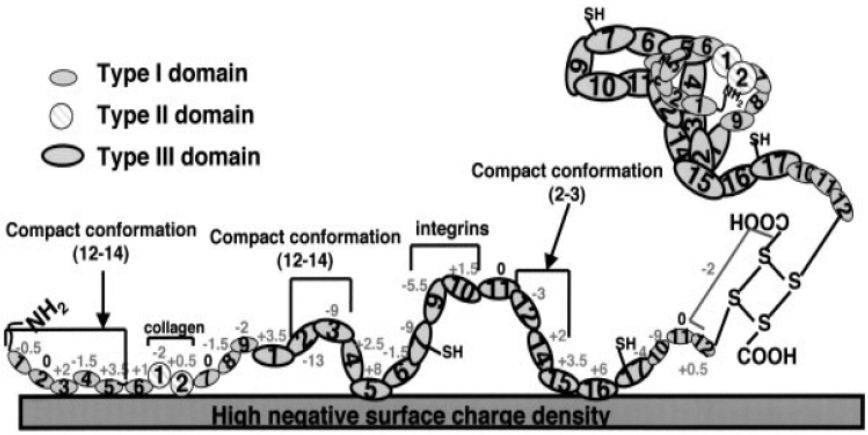

Figure 1.2 Bovine Fibronectin molecular representation. Fn molecules consist of two nearly identical covalently linked subunits, each organized into three types of repeated homologous domains termed type I, II, and III (12 type-I domains, 2 type-II domains, and 15 type-III domains). The structure of bovine Fn, in both solution and on a highly charged surface, is represented in this illustration. The right arm of the molecule is a suggested representation of the folded conformation in solution. The left arm is our proposed representation for unfolded Fn adsorbed onto a highly negatively charged surface. The net charge is indicated for each module. The domains involved in the folded conformation [42] are also indicated. [16]

Chapter 2

Complementary effects of multi-protein components on biomineralization *in vitro*

2.1 Introduction

The extracellular matrix (ECM) is a complex mixture of structural and functional proteins which regulate both physiological and pathological biomineralization processes. During physiological biomineralization, such as bone or dentin formation, specific ECM components are believed to provide the nucleation sites for hydroxyapatite (HAP) and thereby regulate the morphology, size and composition of the mineral deposits [43]. Similarly, in pathological processes, changes in the ECM composition are known to induce such developments as atherosclerotic lesion and vascular calcification [44, 45]. This interplay between bone maintenance and vascular biology has yet to be clearly defined. However, the phenomenon common to both physiological and pathological biomineralization is the initiation of the calcification processes, mediated by ECM proteins in early stages [43]. To understand the fundamental process leading to bone formation or vascular calcification, we have to focus on the development of the ECM and the early stage of biomineral nucleation under the guide of ECM proteins. In this paper, we present an approach to mimic the ECM *in vitro*. We will demonstrate how two non-collagenous proteins can play complementary roles to enhance mineralization when they self assemble together within one fiber.

Fibronectin (FN) and elastin (EL) are abundant in the ECM of connective tissues and calcified tissues. FN is a hydrophilic glycoprotein with a high molecular weight, ~ 550–580 kDa. It is central to the ECM architecture and is involved in many fundamental cell functions such as adhesion, growth, differentiation and migration [46]. FN has been observed to form a prominent fiber network in early stages of matrix-induced endochondral bone formation, during the proliferation of mesenchymal precursor cells [47]. It is ubiquitous during subsequent bone development, highlighting its importance to cellular function during biomineralization. The involvement of FN in early stages of osteogenesis has motivated studies of interactions between FN molecules and apatite particles. Fibrillar FN assembly on sintered hydroxyapatite disks has been observed, dependent upon two bulk solution parameters: protein concentration and ionic strength [48]. The effect of FN on calcium phosphate solution in metastable solution and in agarose gel was probed, but in this study the FN was not in the fibrillar form it takes within the ECM [49]. FN can modify the interfacial energy between surface and mineralization solution and contribute to the early precipitation of biological HAP, a process which occurs during osteointegration of ceramic hydroxyapatite bone implants [49]. FN was further suggested to be the key regulator of arterial calcification via an integrin-based signal pathway [50]. FN has been linked to transplant arteriosclerosis and has been found in the adventitia of rat aortic grafts [51] as well as around calcified lesions in mouse myocardium [52]. After arterial injury, FN in the extracellular matrix may cause exposed vascular smooth muscle cells (VSMC) to re-differentiate into osteoblast-like cells [53, 54].

Knowledge regarding the role of EL, a primary protein with a low molecular weight (~68 kDa) found in connective tissue such as aorta and skin, also hints at a relationship to pathological mineralization. Age-related degradation of EL in the human aorta is directly involved in

elastocalcinosis, or the deposition of HAP in the elastic lamellae of arteries [55]. Recent findings suggest that EL may act as an inhibitor of calcification depending on its protein chemistry and/or structure. The addition of insoluble EL fibers to a collagen scaffold causes calcification in rats one week after implantation, but no calcification occurs when the scaffold contains EL fragments [56]. These discussions indicate that both FN and EL have the potential to control the deposition of biominerals. However, the interactions between the protein and inorganic ions and the cooperative effects, if any, of FN and EL on the deposition of calcium phosphate minerals during biomineralization have hardly been explored.

In the present paper, we demonstrate complementary surface sensitive techniques to study the process of biomimetic mineralization from the earliest stages. Using a charged polymer substrate we show that the two ECM proteins, FN and EL, co-adsorb and self assemble into a common fiber network. Then, by exposing the fibers to calcium phosphate solution at physiological pH and ionic concentration, we are able to track the mineralization process, starting from incorporation of the ions into the proteins, through nucleation of HAP crystals. In previous work we demonstrated that mineralization was templated on FN fibers from supersaturated solution of calcium carbonate [20]. Here we show that templating also occurs from physiological concentration of calcium phosphate solutions. In this case, the concentration is such that nucleation on inert surfaces does not occur. Hence the biomineralization process in this case is assisted by the conformation of the proteins. Since these two proteins are different we also expect their ability to biomineralize to differ. To our aim, Synchrotron-based Scanning Transmission X-ray Microscopy (STXM) can be used to image the calcium in the fibers, as early as seven days' incubation. Grazing incidence synchrotron X-ray diffraction (GIXD), as well as Transmission Electron Microscopy (TEM) is used to determine the crystallinity of the calcium

deposits, while Scanning Electron Microscopy (SEM) with Energy Dispersive X-ray Spectroscopy (EDXS) is used to probe their elemental composition. The earliest evidence of ionic absorption into the protein fibers, however, is tracked indirectly through measurements of the fiber heights and modulii, where significant changes occur within the first few hours of incubation. In previous work we demonstrated that FN and EL nucleated calcium carbonate crystals exclusively in their fibrillar form [20], but their efficiency for biomineralization differed. In the present work, we show that these two proteins can have complementary roles in the nucleation and growth of calcium phosphate mineral. Such differences have important implications for the templating of biominerals by proteins.

2.2 Materials and Methods

2.2.1 Sample preparation

Polished 200 μm thick ‹100› Si wafers were obtained from Wafer World Corporation, West Palm Beach, FL. Si TEM grids having 100 nm thick silicon nitride windows were obtained from Silson Ltd., Northampton, England. Both types of substrates were spin-coated with Sulfonated Polystyrene: SPS, $M_w \sim 175k$ (Polymer Source Inc., Dorval, Canada) which was dissolved in N, N-Dimethylformamide (Sigma-Aldrich, Inc., St. Louis, MO), spun-cast, and vacuum dried as described in our previous work [20]. FN from bovine plasma and EL from bovine neck ligament (Sigma-Aldrich, Inc., St. Louis, MO) were dissolved in Phosphate-Buffered Saline (PBS) without calcium or magnesium (Invitrogen, Carlsbad, CA). Prepared SPS-coated wafers were incubated in the solutions of FN, EL, and FN-EL in PBS buffer (FN: 100 mg/ml, EL: 5 mg/ml, FN-EL: FN 100mg/ml and EL 5mg/ml) for four days at 37°C and 100% RH in 24-well dishes (BD, Franklin Lakes, NJ). After the self-assembled protein network formed,

samples were rinsed three times with deionized (DI) water to remove the unabsorbed protein and salts in the PBS.

Samples were immersed in a metastable calcium phosphate solution [57] which was prepared as follows: Salts were purchased from Mallinckrodt Baker Inc., Phillipsburg, NJ. Solutions were made in HEPES buffer, 1M, (Mediatech Inc., Manassas, VA) and diluted to 25 mM with DI water. NaCl solution (137 mM) in 25 mM HEPES buffer was prepared and the pH was adjusted to 7.4. $CaCl_2$ and Na_2HPO_4 stock solutions with the concentrations of 5.6 mM and 4 mM, respectively, were prepared separately in the above NaCl solution and the pH was readjusted to 7.4. Each of the stock solutions contained in addition 0.05 % (w/v) sodium azide (Sigma-Aldrich, Inc., St. Louis, MO) to avoid bacterial contamination. The metastable calcium phosphate solution was freshly prepared before use by rapidly mixing equal volumes of $CaCl_2$ and Na_2HPO_4 stock solutions. The final composition of metastable calcium phosphate solution is shown in Table 2.1. All the mineralization experiments were carried out at room temperature, at which the solution is known to be metastable and does not precipitate mineral observed by SEM onto bare Silicon wafers or polymer films up to 28 days. After the different mineralization time points (as given in the results section) samples were rinsed by DI water twice, air-dried overnight and stored in a desiccator for further characterization by different methods. An exception is samples examined by scanning probe microscopy, shear modulation force microscopy and confocal laser scanning microscopy, which were examined under wet conditions as described in the following sections.

2.2.2 Scanning Probe Microscopy (SPM) and Shear Modulation Force Microscopy (SMFM)

The early-stage imaging and height measurements were made using a Dimension 3100 SPM (Veeco, Santa Barbara, CA) in contact mode with a silicon nitride tip (Veeco, Santa Barbara, CA). After the specific mineralization time point, the sample was rinsed twice by PBS and then immediately measured, in PBS, with scanning force microscopy in a 35 mm petri-dish (BD, Franklin Lakes, NJ) shown in Fig 2.1A. The fiber height was evaluated using SPM cross-sectional images by measuring fiber heights referenced to flat base regions as shown previously [20]. For each protein, two different samples were imaged for each time point and 30 fibers on each sample were analyzed. The error bars shown for fiber height data represent the standard deviation obtained from approximately 60 measurements.

The mechanical responses of protein fibers during biomineralization were measured by SMFM. Use of the SMFM to measure shear modulus response relies on lateral modulation of the cantilever buried ~3 nm deep into the sample, and measurement of the amplitude response, as detailed previously [20, 41]. The silicon nitride cantilever of the tip with a spring constant of 0.06 N/m was modulated laterally at a sinusoidal frequency of 1400 Hz. A constant normal force of 25 nN was used to maintain contact of the tip with the surface shown in Fig 2.1B. The response amplitude was measured as a function of the driving amplitude, where the response amplitude ΔX is related to the modulus E by Eq 2.1.

$$\Delta X \sim h = \left[\frac{3}{4}\left(\frac{1-\nu^2}{E} \cdot \frac{L}{R^{1/2}}\right)\right] \qquad \text{Eq 2.1}$$

Where ΔX is the response amplitude, E is the elastic modulus of the material, ν is the poisson ratio of the material, h is the height of indentation on the surface of the material, L is the load applied on the surface of the material, R is the tip radius.

By measuring a series of response curves on the sample over the linear range of force applied, a relative measure of the modulus is obtained that can be compared over different sample regions at chosen time during the mineralization process. The SPM tip size and indentation during SMFM measurements are of order 2-3 nm, making it possible to unambiguously probe the modulus of the fibers. Three different sets of readings were taken at different regions with three measurements for each set. Significance of observations is determined by t-tests.

2.2.3 Confocal Laser Scanning Microscopy (CLSM)

FN and EL were individually labelled with Oregon Green 488 protein labelling kit (Invitrogen, Carlsbad, CA) before solution preparation. For the mixture, the labelled FN or EL solution was mixed with unlabelled EL or FN solution to the final concentration of 100 μg/ml FN and 5μg/ml EL. The SPS-coated Si wafers incubated with the above protein solutions for four days were rinsed by PBS twice and kept in a 35 mm petri-dish (BD, Franklin Lakes, NJ) with PBS for imaging by CLSM (Leica, Bannockburn, IL) with a 63× water objective lens.

2.2.4 Grazing Incidence X-ray Diffraction (GIXD)

Grazing incidence X-ray diffraction (GIXD) experiments were carried out on NSLS Beamline X6B at BNL. The X-ray wavelength λ = 0.6525 Å and spot size 0.25 mm vertical × 0.4 mm horizontal were used. The sample was mounted on a goniometer head at a distance of 150 mm from the detector screen. Grazing incidence diffraction patterns with an incident angle of

1.0º were recorded using an X-ray CCD detector (Princeton Instruments, Trenton, NJ). The detector geometry (distance from sample, tilt of detector, center of diffraction pattern) was calibrated using a transmission diffraction pattern of standard Al_2O_3 plate. In addition, synthetic Hydroxyapatite and Amorphous Calcium Phosphate powders (Sigma-Aldrich, Inc., St. Louis, MO) as controls were investigated for reference in both glass capillary tubes (1.0 mm diam.) and as compressed powders on a blank SPS substrate [17].

2.2.5 Scanning Transmission X-ray Microscopy (STXM)

X-ray imaging and spectroscopy were carried out on beamline X1A1 at the National Synchrotron Light Source (NSLS) at Brookhaven National Laboratory (BNL). A monochromatic soft X-ray beam is focused to 50nm by a Fresnel zone plate, and the sample is scanned through the focal point in two dimensions while recording the intensity of transmitted X-rays. The soft X-ray beam with the energy range from 270 ~ 800 eV does not cause mineral sublimation through specimen heating. Samples were assembled onto 100nm-thick Silicon-Nitride membrane windows for X-ray transmission. The carbon K-edge energy calibration was determined using CO_2 and calibrated to peak positions reported by Ma [58] using a Gaussian fit. Energy near the calcium L-edge peaks was calibrated by assigning measured calcite $L_{3,2}$ peak positions to 349.3 eV and 352.6 eV [59, 60].

2.2.6 Transmission Electron Microscopy (TEM)

Samples on Silicon Nitride membrane windows were observed after 7-day and 21-day mineralization intervals by using a JEOL JEM2100F high-resolution analytical TEM (Center for Functional Nanomaterials, BNL) operating at 200 kV. The electron diffraction patterns of the particles were recorded by using a selected-area aperture allowing observation of a circular area

of 1.36-μm diameter. Caution was taken regarding the size and thickness of the examined aggregates, because these parameters may influence the quality of the diffraction patterns.

2.2.7 Scanning Electron Microscopy (SEM)

SEM measurements (Helios Nanolab, FEI, Hillsboro, OR) were conducted at the Center for Functional Nanomaterials, BNL. The morphology of crystals on the protein matrices after 28 days in calcium phosphate mineralization solution was investigated at 15 kV acceleration voltage and 4 mm working distance.

2.3 Results

A 20 nm thick coating of Sulfonated Polystyrene (SPS) polymer on either a clean Si wafer (500 μm thick) or a Si-nitride window (100 nm thick) provides a surface conducive to protein fiber formation [16, 17, 20]. After 4 days of incubation at 37°C, proteins from solution are adsorbed on the SPS-coated silicon surface. As seen by SPM height imaging, both FN (Fig 2.2A) and EL (Fig 2.2C) self-assemble into fiber networks, of slightly different dimension. The SPS coating is necessary: when bare silicon substrates are used, no fibrillar ECM network forms; only small amounts of protein globules, < 300 nm in height, can be imaged [17]. In Fig 2.2B we show the network formed when both proteins are adsorbed. From the SPM image only a single network is apparent. By labelling each protein in turn with Oregon Green 488 and imaging with confocal microscopy, we demonstrate that in the FN-EL mixture the two proteins have combined into one fiber network, with no evidence of phase segregation. A green fluorescent network is visible when either FN (Fig 2.3A) or EL (Fig 2.3B) is labelled. At higher magnification (Fig 2.3A, inset) it appears that FN forms the backbone of the fiber. This is supported by the SPM friction images of each network in Fig 2.3C-E: pure FN, mixed FN-EL, and pure EL have each

been examined. The pure networks show contrast from the softer fiber regions (white) compared to the flat (dark), hard substrate areas between them. In Fig 2.3D we see that the combined FN-EL fibers are not uniform. Instead they have a backbone which is harder (darker) than the sides of the fibers. Based on the confocal images, we postulate that the harder backbone has more FN than the softer sides, which are EL-rich areas. Based on AFM topography shown in Fig 2.2, the combined fibers are thinner (Fig 2.4A) and have a smaller mesh size than either pure protein. This is not surprising since the self recognzition sites on the proteins are can be in different regions than those for the complementary protein, which can lead to different secondary structures. Further study on this aspect using FN fragments is underway, and will be published elsewhere.

Biomineralization in the earliest stages is very challenging to observe since the ion concentration is below detection by traditional methods, such as Energy-Dispersive X-ray Spectroscopy (EDXS) or other ion and X-ray scattering. SPM allows us to measure whether any changes in the morphology or the mechanical properties occur once the fibers are immersed in mineralization media. The fiber heights plotted as a function of incubation time in calcium phosphate mineralization solution are shown in Fig 2.4A. The fiber height of all proteins increases with exposure time, despite the fact that the ions are as yet undetectable in the first 12 hours (Fig 2.4A, closed symbols). During the first 4-hour mineralization, heights of all of the protein fibers increase quickly (>0.05 $\mu m \cdot hr^{-1}$) and then level off near final heights of 1.10 μm, 0.76 μm, and 1.26 μm, which represent increases of 83%, 54%, and 60% for FN, FN-EL, and EL respectively. When placed in Phosphate-Buffered Saline (PBS) for 12 hours, the fiber heights are unchanged (Fig 2.4A, open symbols), indicating that neither water nor other ions swell the fibers. Hence the increase of fiber height is specific to the mineralization ion in the solution, which

indicates that the ions penetrate and restructure the protein fibers almost immediately. Our previous work, in which both pure EL and FN systems were immersed in a calcium chloride control solution, demonstrated that either carbonate [20], or phosphate, as is the case here, are required to produce any time-dependent changes in the SPM experiment.

Structure changes in the fibers can also be sensed by differences in mechanical response. Shear Modulation Force Microscopy (SMFM) measures the relative change in modulus of the fibers. In Fig 2.4B we show the modulii of the fibers as a function of time, where the scale is relative to the response of non-biomineralized EL. From the figure we see the modulus of FN is on average 22% higher than that of the EL, consistent with the lateral force images shown in Fig 2.3D. On the other hand, the modulii of the fibers formed from the FN-EL are 12%, which is slightly smaller, though not significantly that the value for EL. When exposed to the calcium phosphate mineralization solution, the modulii of the FN and the FN-EL fibers begin to increase rapidly, tracking the changes in fiber height shown previously. This modulii increase at a rate of 0.15 hr^{-1} for FN ,0.17 hr^{-1} for FN-EL and only 0.02 hr^{-1} for EL for the first 4 hours, after which the change becomes more gradual, becoming less than 0.02 hr^{-1} for all the fibers. As a result we can see that even though the FN-EL fibers were initially softer than those of EL, they rapidly become harder. During the 12 hour period the modulii of the FN and the FN-EL fibers increased by 66% and 68% respectively, while those of the EL fibers increased only by 8%. The change in fiber modulii in control samples, placed in PBS solutions are shown as open symbols in the figure. Here we can see that no increase and even a slight decrease in modulus occurs with -16% for FN, -7% for FN-EL and EL. The results suggest that mineral ions do not simply adsorb onto the protein fibers non-specifically. Rather, since each of the three networks shows a different behavior on exposure to solution, the interaction may be chemically specific to the protein or

protein combination, as well as on the network structure. The next two questions to answer are: (I) when do mineral nuclei appear; and (II) what makes the response of pure EL different? To study spatially resolved Ca deposition and mineral crystallinity, we turn to x-ray scattering and microscopy methods.

Synchrotron Grazing Incidence X-ray diffraction (GIXD) data from crystals templated by FN and FN-EL are shown in Fig 2.5A and B. Up to 14 days (data of day 7 not shown), no statistically significant diffraction peaks in either profile could be observed above the background. Thus the presence of crystalline hydroxyapatite within the organic matrix could not be detected. At 21 days, the FN-EL matrix generates a pattern of poorly crystalline HAP with one small broad asymmetric peak corresponding to the (211)/ (112) crystal planes. At 28 days, two broad peaks corresponding to the (002) and (211)/ (112) planes of HAP are observed on FN and FN-EL matrices. Using the Scherrer equation, we estimate that the diffraction peaks were obtained from crystallites approximately 10 to 30 nm in size. These values are comparable to those reported for crystals formed in bone [61]. This is only a lower boundary, however, since further details of grain size and strain are not accessible due to the geometry of the GIXD method, which causes additional peak broadening (see appendix A, supplemental Fig 4 of [17]). The EL sample has no X-ray diffraction pattern even after day 28 (Fig 2.4C). These results indicate that only after 28 days of mineralization sufficient bone-like hydroxyapatite is templated on FN and FN-EL to be observed by GIXD. Hence, evidence of biomineralization at earlier stages can only be obtained by other complementary techniques.

Scanning transmission X-ray microscopy (STXM) enables us to obtain protein and calcium distribution maps for self-assembled protein matrices at earlier time points. The synchrotron-based STXM focuses a soft X-ray beam to a 50 nm spot size and photons are

transmitted through the fibers. In this measurement, samples have been rinsed by DI water twice and then air-dried, which has the effect of shrinking the fiber height to less than a micron and enabling the soft x-rays to transmit through them. The small beam is an excellent probe of the micron-scale fibers, sensitive to absorption contrast at the C K-edge and Ca L-edge. Images of the same region on the samples after 7-day mineralization at the C K-edge peak (288.2 eV) and at the Ca L-edge (349.3 eV) are shown in Fig 2.6 (left and right columns for C and Ca edges respectively). At 288.2 eV, the amide carbonyl group in protein absorbs x-rays, making fiber areas appear dark. The morphology is similar to that observed by SPM. The same areas of all three 7-day mineralized films are also shown at the Ca L-edge. When FN is imaged at the Ca edge, the fiber contrast is greatly reduced, due to the fact that the energy is far from the carbon K-edge, and this lower absorption contrast also indicates that the fibers do not contain appreciable calcium. Instead small dense spots (arrows) appear on the fibers, evidence for Ca-bearing particles of a few hundred nm in size. The EL network behaves differently. The EL fibers imaged at the Ca edge show a large absorption contrast, indicating that it is along the fibers that the Ca is located. Moreover, no distinct particles are found in EL images we examined. Therefore, Ca in the EL network appears to absorb into the fibers. The FN-EL mixture shows both of these two features. At the Ca edge, fiber contrast is slightly enhanced, and distinct particles also appear. Our interpretation is that EL absorbs Ca in its fibers, while FN nucleates mineral particles. The combination of FN and EL allows these processes to work together.

To investigate the properties of minerals templated on the protein matrices, we turn to transmission electron microscopy (TEM) and selected-area electron diffraction (SAED) for the same day-7 samples used in STXM. Fig 2.7A shows the TEM images of the three different protein matrices, and the small particles of different shapes present on FN and FN-EL. On the

FN sample, small platelet-shaped particles consisting of needle-shaped subparticles are uniformly present on and near the protein fibers. On the FN-EL sample, small spherical particles are observed which aggregate beside the protein fibers. Despite their appearance, none of the particles on either substrate produce rings in the electron diffraction patterns shown in Fig 2.7B, indicating lack of crystalline order in the particles. Hence the particles formed at the earliest stages of the biomineralization process consist of some type of amorphous calcium containing deposit. The TEM image of EL shows that there are only protein fibers without any particles. In Fig 2.7B we also show a representative diffraction pattern similar to those obtained from several EL samples, which only shows the same type of diffuse scattering pattern as observed for FN and FN-EL.

When mineralization develops into late stage (day 21), minerals with different morphology are observed in the STXM images of the FN-bearing surfaces, shown in Fig 2.8A. However, the calcium-dense area on EL only follows the morphology of the protein network. The detailed morphology and crystal property of different minerals templated on the protein matrices were characterized by TEM shown in Fig 2.8B. Needle-shaped crystals are observed on FN, with clear polycrystalline diffraction rings. On FN-EL, small plate-like crystals surrounding protein fiber produce the weak diffraction rings. On EL, small needle-like crystals with weak diffraction were confined inside the EL fibers and there is no crystal observed in areas between the fibers. All the samples in Fig 2.8C produce different degrees of diffraction patterns exhibiting the (002) and (211) hydroxyapatite (HAP) reflections.

SEM images from the back-scattered electron signal for day-28 mineralization are shown in Fig 2.9. These images are not sensitive for the protein network which has a lower atomic number value than the substrate (Si). Hence we can clearly see when biomineralized deposits,

with higher atomic number, form. In the Fig 2.9, we find that the surfaces are uniformly covered with HAP particles on the FN and FN-EL. No particles are seen on the EL. Even in the low resolution images, we can see that the deposits templated on the FN and FN-EL are different. The FN produces large distinct particle aggregates while the FN-EL produces gradual but more uniform particles. In the inset we show a magnified view of the region shown in Fig 2.9A and B, where we can clearly see that the particles are composed of discrete crystallites with plate and needle morphologies. Pure EL viewed by SEM shows that the production of large coverage of mineral particles has been suppressed; the nanoscale needles viewed by TEM are not numerous enough to provide the electron contrast needed to image them by SEM (Fig 2.9C). HAP went undetected by GIXD as well, suggesting that perhaps only a fraction of the Ca-rich material on EL became crystalline. The raw EDXS response was used to compare Ca/P ratios of these particles. The Ca/P ratios deduced from EDXS measurements calibrated using synthetic HAP as a standard are 1.55±0.12 for FN and 1.46±0.24 (standard deviation of three measurements per sample) for FN-EL. These values are comparable to each other, but less than 1.67 obtained for the HAP standard measured. The proteins nucleate a form of calcium deficient HAP which is consistent with the theory reported by Olszta and et al [62], where they proposed that non-stoichiometry of the HAP bestows the bone mineral solubility for resportion of the bone by osteoclasts during bone remodelling and repair process.

2.4 Discussion

The actions of non-collagenous proteins (NCPs) are central to the fundamental mechanism of biomineralization *in vivo*. Based on our data, we propose that NCP-mediated biomineralization occurs in three stages. The first step involves ionic adsorption into the fibrillar protein matrix, leading to the modification of structural and mechanical properties of protein

fibers (Fig 2.4). The second step is the nucleation of nanometer-size particles, which occurs only on certain proteins. Neither synchrotron GIXD (Fig 2.5) nor TEM (Fig 2.7) detects crystalline order in these particles. The third step is that the nanometer-sized particles grow into micrometer size by further ionic deposition and/or aggregation and undergo phase transformation into HAP crystals (Fig 2.8 and Fig 2.9). With further incubation, particles seen on FN become crystalline and grow significantly larger, while on EL the formation of distinct particles outside the fibers is suppressed.

As we can see in Fig 2.5, the X-ray data exhibit weak peaks on a large background. TEM is more sensitive since the beam can be focused on individual particles. Well defined diffraction rings are observed. To quantify these TEM diffraction patterns, we performed a powder-like integration of the diffracted intensity plotted against momentum transfer q in Fig 2.10A[1]. For comparison, synchrotron powder X-ray data of commercial HAP and ACP also plotted against q, shown in Fig 2.10C. Note that the strong peaks of HAP are in the region q= 1.83 $Å^{-1}$ and 2.25 $Å^{-1}$ which is corresponding to the (002) and (211) planes, while the broad peak in the bulk structure factor of ACP is at q= 2.05 $Å^{-1}$. In TEM data at day 7 (dashed line) no sharp diffraction peaks are present. To clarify the details of peaks near 2.05 $Å^{-1}$, we use the featureless spectrum of EL-7day as a baseline, and all spectra shown in Fig 2.10B have been subtracted by that spectrum. The spectra of FN-7day and FN-EL-7day have a broad peak with its maximum in the same position as the ACP structure factor shown in Fig 2.10B, which suggests that the nanometer-sized particles on FN containing samples incorporate ACP. By day 21, peaks in FN containing samples are clear which correspond to the (002) and (211) planes of HAP. A number of studies point to the possibility that the initially deposited ACP transforms into a crystalline

mineral phase [62-65]. Our study demonstrates how ACP formation may be initiated by NCPs in the early stage of biomineralization *in vitro*, following which it is transformed into HAP.

In our study, we also demonstrate that different NCPs play different roles during the biomineralization process. Based on the above results, we propose to take into account the proteins' relative structural heterogeneity. The FN molecule is a dimer with specific dissimilar domains known to interact with each other when the protein unfolds to form fibrils [65]. Since FN alone can nucleate calcium phosphate crystals from physiological calcium phosphate solution, we surmise that both cations and anions must bind to FN in such a way as to be brought into proximity with each other under our experimental conditions. We propose that FN has specific sites which capture phosphate and calcium, though not in large amounts. When fibrillogenesis occurs, the adjacent FN molecules bring calcium and phosphate in proximity with each other, enhancing nucleation, and eventual crystal growth. However, EL is expected to be very different based on the properties of the molecule. Its hydrophobic subunits are structurally similar to each other, and the extended network is mechanically flexible. This means that even when the conformational change into fibers occurs, the local environment seen by ions near the protein is similar throughout the fiber. We have no evidence that the protein in its globular form interacts with ions. STXM images (Fig 2.6) show that in the fiber structure, calcium is bound to the protein in significant amounts. However, the presence of phosphate in solution is required for this to occur: our previous work showed that EL fibers underwent no detectable changes when immersed in $CaCl_2$ control solutions [20]. Despite the abundance of Ca and the implied proximity of available phosphate, the release of mineral particles outside the protein fibers is evidently suppressed by EL. Although the role of phosphate remains to be determined, an understanding of the cooperative effect in the FN-EL mixture is suggested by our model. The

collection of calcium by EL, and the structural control exerted by FN, work together to nucleate a greater amount of calcium phosphate particles, which are amorphous in the early stages but later transform into calcium deficient apatite crystals. Even though many crystallites are obtained, the TEM and STXM data imply that a significant amount of calcium in the protein mixture remains un-associated with the crystals — either as bound calcium ions or in amorhpous mineral form — based upon the images showing contrast from fibers co-existing with mineral particles.

In summary, our work provides direct evidence that two specific NCPs can combine to provide the molecular design necessary for controlling biomineralization. Our next step is to investigate how FN and EL affect mineralization of collagen, the most abundant component of the ECM. The retarding mechanisms in biomineralization, which are crucial to prevent pathological mineralization in the early stage, are under intense investigation. We emphasize here that an apparent retarded biomineralization, as by EL alone, can become an enhancer of mineralization by sequestering cations, if a complementary protein in the system provides the structure that overcomes barriers to nucleation.

[1] Calibration and resolution of integrated TEM data are not as reliable as the X-ray technique, leading to slight inaccuracy in q values for TEM.

Tables:

Table 2.1 Composition of Metastable Calcium Phosphate Solution

Composition	***concentration (mM)***
Calcium chloride	2.8
Sodium phosphate	2
Sodium chloride	137
Hepes	25
Sodium azide	2.74
Ca/P	1.4

Figures:

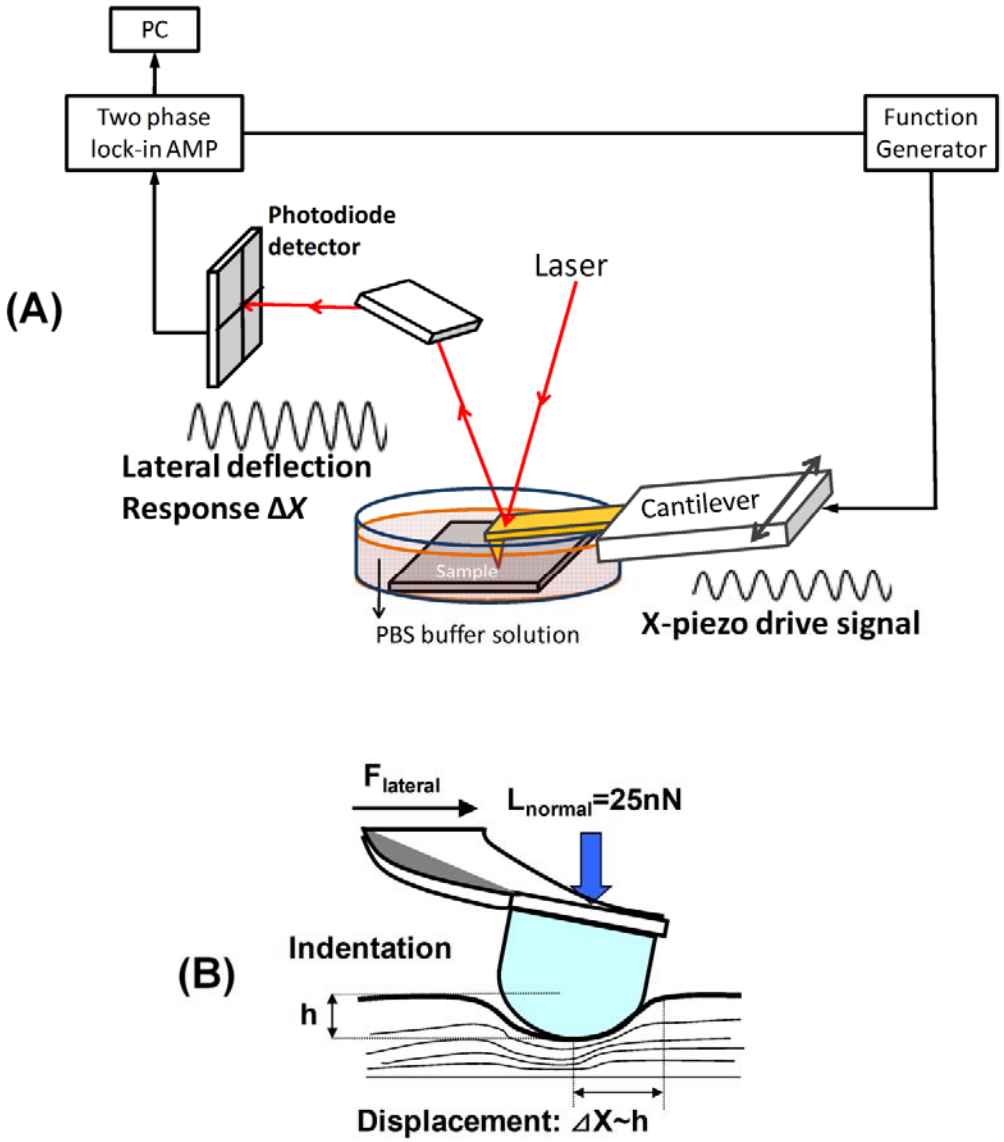

Figure 2.1 (A) Schematic set-up of Scanning Probe Microscopy (SPM) and Shear Modulation Force Microscopy (SMFM) (B) Principle of SMFM

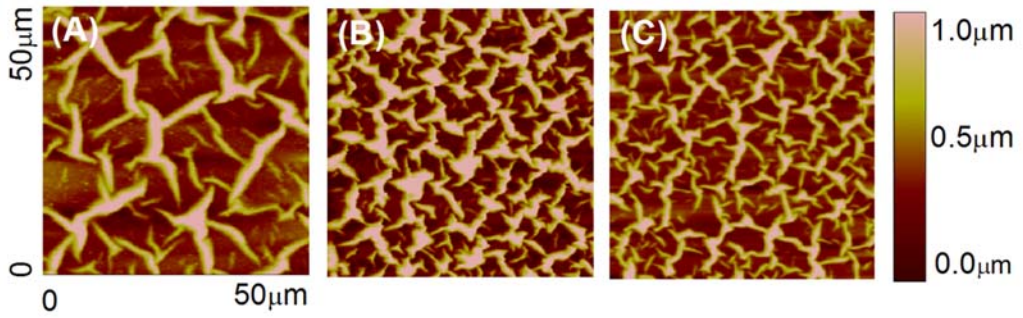

Figure 2.2 Contact mode SPM topography images (50μm×50μm) of self-assembled protein network on SPS-coated silicon wafer after 4-day incubation in protein solutions: (A) FN; (B) FN-EL; (C) EL.

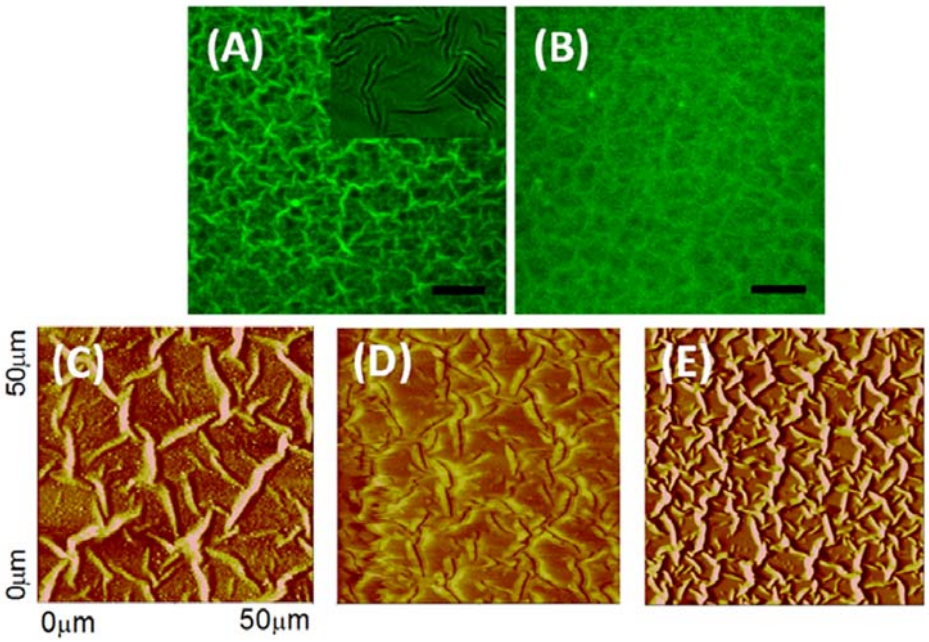

Figure 2.3 Confocal images of two FN-EL samples fluorescently labled with Oregon Green 488 prior to adsorption on SPS coated Si wafers: (A) The FN is labeled with Oregon Green 488 while the EL is unlabelled. Inset: higher magnification image showing FN-rich (green) region on the backbone of the fibers. (B) The EL is labled with Oregon Green 488 while the FN is unlabled. Uniform fluorescence intensity in the fiber patterns in both images indicates that the proteins combine to form uniform common fiber structures, rather than phase separated networks composed of the individual separate two proteins. Scale bar in (A), (B) = 10 μm. Lateral friction images (50μm×50μm) corresponding to (C) a pure FN network network showing fibers of uniform mechanical response which appear soft (white) fibers against the hard (dark) Si wafer background. (D) A mixed FN-EL network, where the fiber backbone appears harder (darker) than the fiber edges (white). This image corresponds to that shown in the inset of (A) and hence we infer that the backbone is stiffer since it is enriched in the FN, the stiffer of the two proteins. (E) Uniform fibers of the smaller EL network, which also appear softer (white) than the surrounding flat regions (dark).

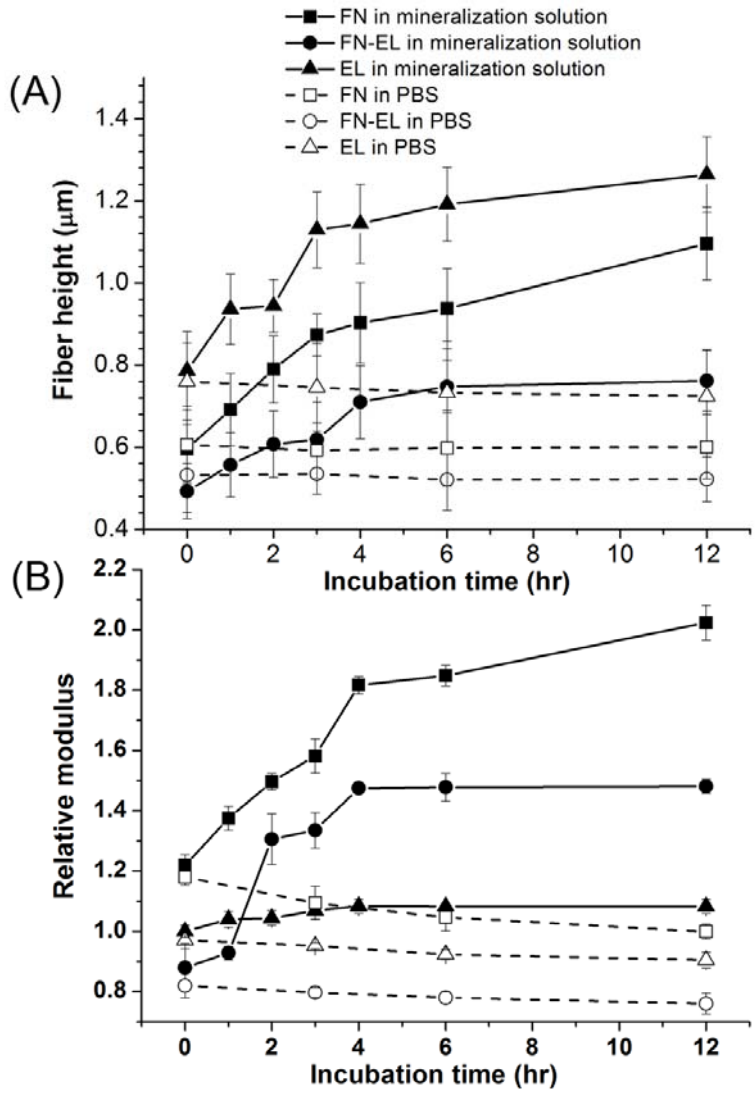

Figure 2.4 (A) Average fiber heights measured by SPM for FN, FN-EL, and EL networks as function of time immersed in calcium phosphate solution (closed symbols) or buffer control solution (opened symbols). See figure key for symbols. Lines are guides for the eye. (B) Relative elastic modulus of protein fibers measured by SMFM technique under each condition (see figure key). All values are normalized to the response of EL in calcium phosphate solution at $t = 0$, prior to mineralization.

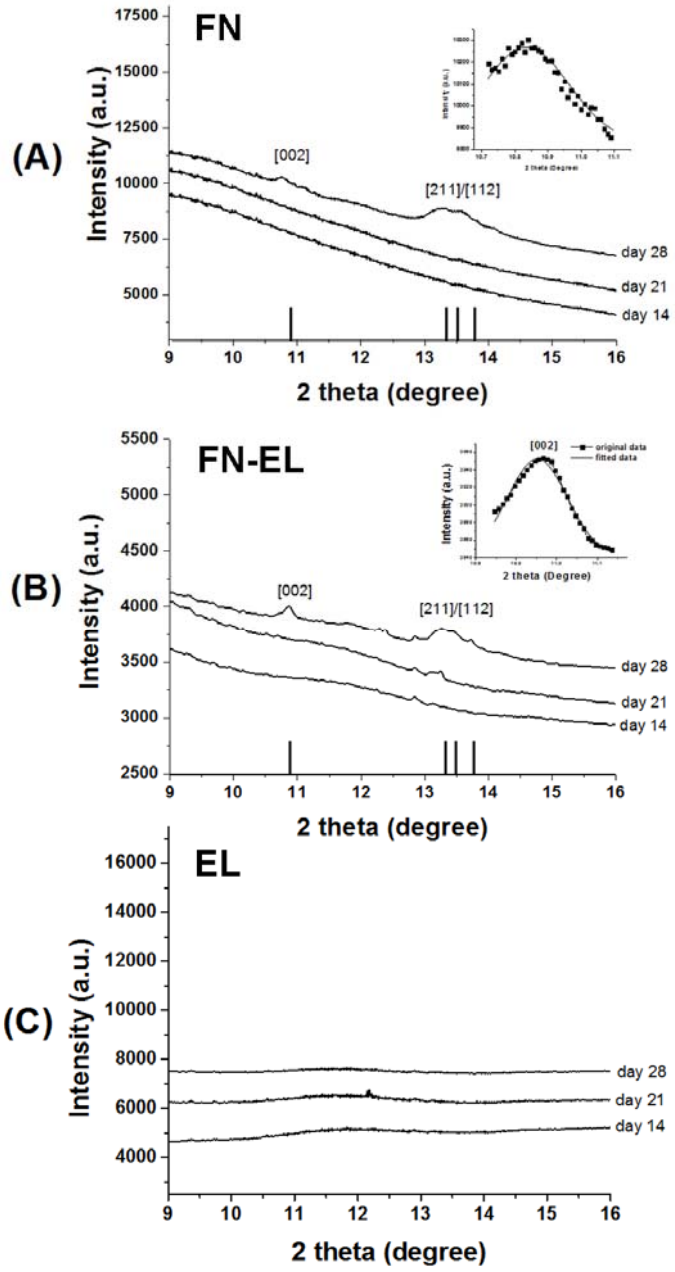

Figure 2.5 Synchrotron Grazing Incidence X-ray Diffraction (GIXD) patterns of 14-, 21-, 28-day (A) FN; (B) FN-EL and (C) EL on SPS-coated silicon wafer (Wavelength = 0.65255 Å). Inset: Gaussian fitting of (002) diffraction peak on 28-day samples. Lines on 2-theta axis indicate the intense lines of the standard HAP diffraction pattern.

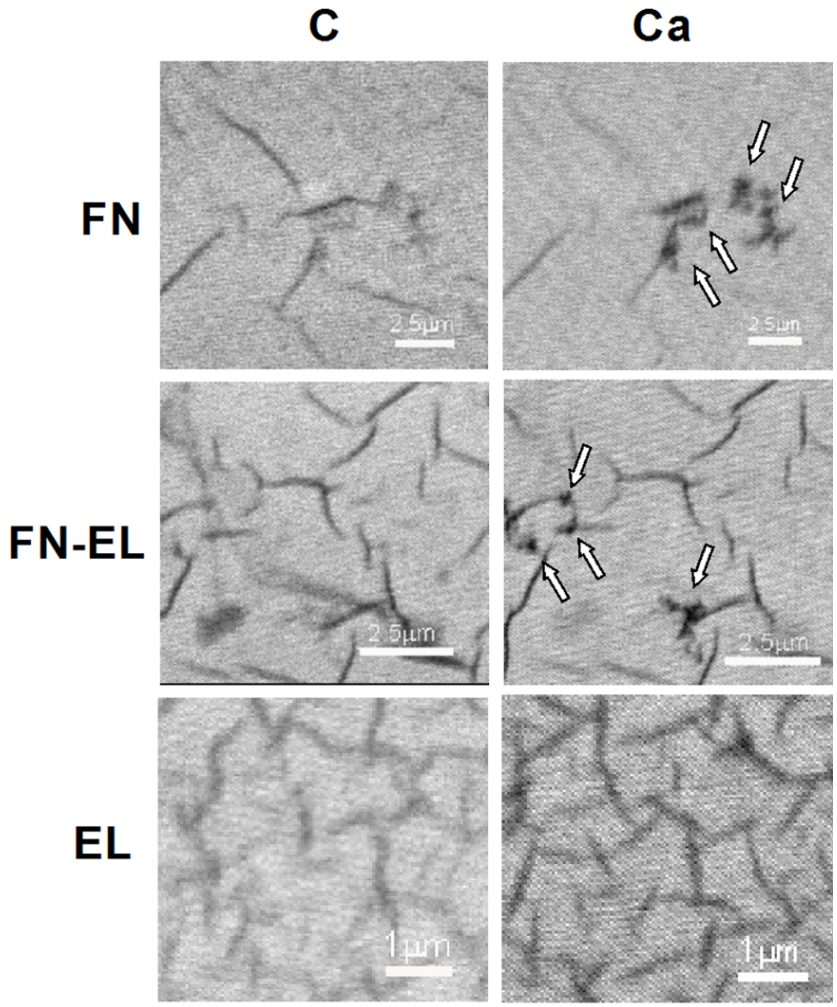

Figure 2.6 STXM images of self-assembled protein matrices after 7 days' incubation in calcium phosphate mineralization media. Left column: C K-edge map at 288.2 eV, highlighting protein-dense regions. Right column: Ca L-edge map at 349.3 eV. Rows: FN network, FN-EL mixture, and EL network as labeled. Arrows show where calcium-rich deposits appear as submicron-scale particles, in samples containing FN. The EL sample fibers are calcium-rich (darkest in the EL Ca L-edge map) but no discrete Ca-bearing particles separate from fibers are observed. Image intensity scales in each column have been set to identical range and contrast parameters and have been taken under comparable beam currents.

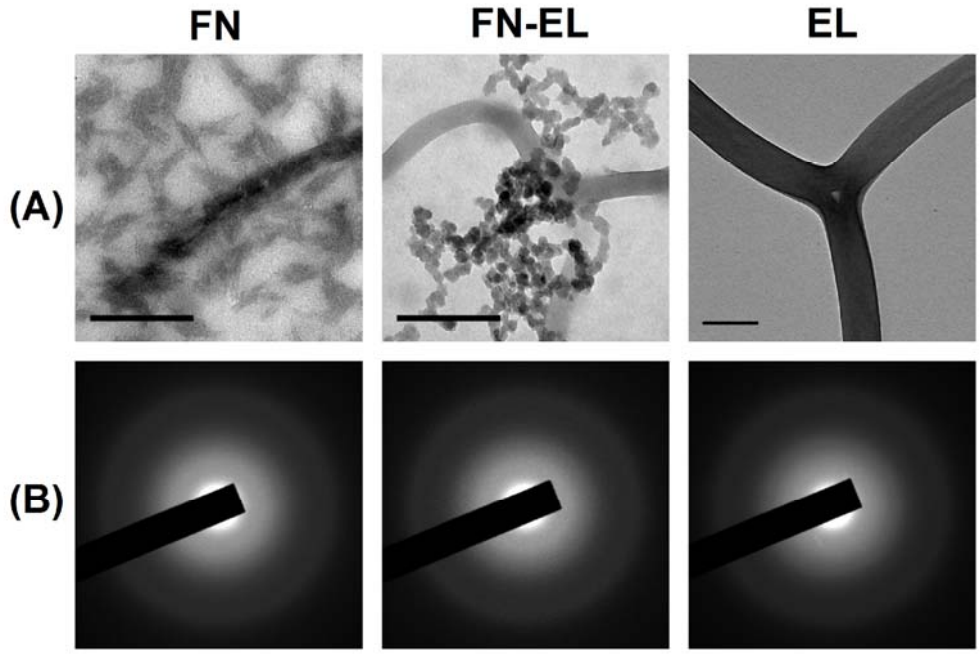

Figure 2.7 (A) High-resolution TEM images and (B) SAED pattern of mineral particle morphologies in different protein matrices after 7 days' incubation in calcium phosphate mineralization media. Columns: FN network, FN-EL mixture and EL network as labeled. (Scale bar: 250 nm). Corresponding SAED patterns exhibit diffuse background scattering only.

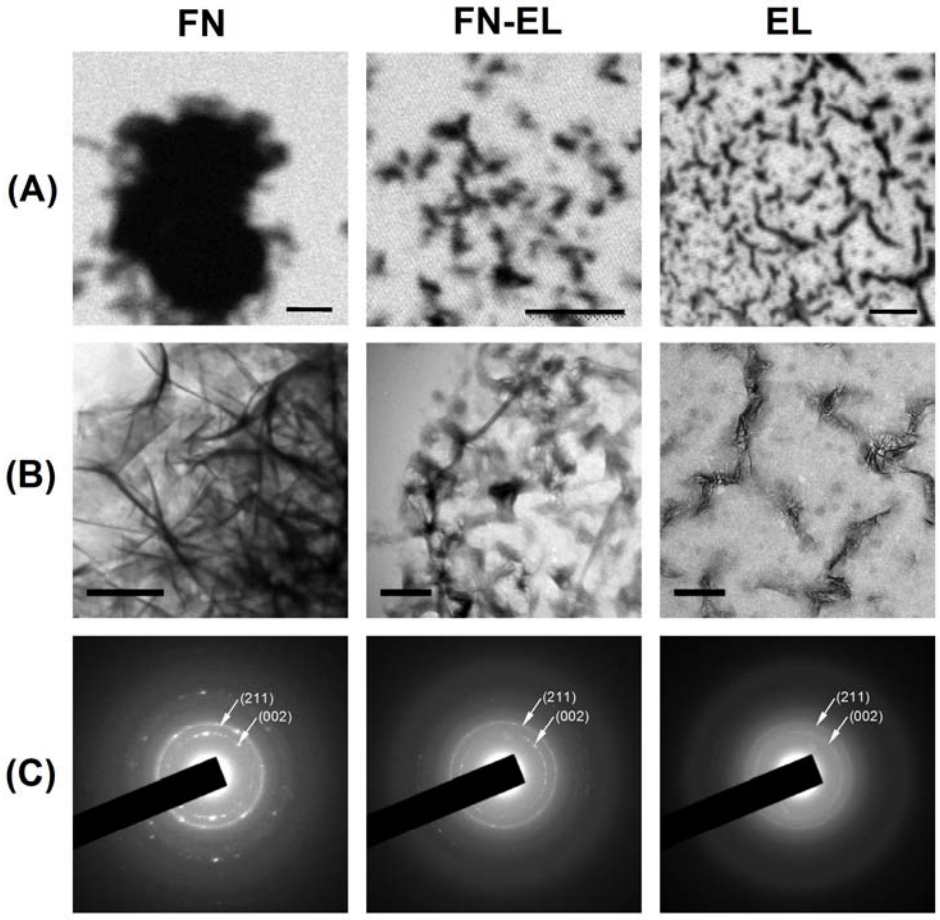

Figure 2.8 (A) STXM images correlated with (B) High-resolution TEM and (C) SAED of mineral templated on protein matrices after 21 days' incubation in calcium phosphate mineralization media. Columns: FN network, FN-EL mixture, and EL network as labeled. Scale bar in (A): 2.5 μm. TEM images show the detail morphology of crystals and protein fibers. (Scale bar in (B): 0.3 μm in FN and 1 μm in FN-EL and EL).

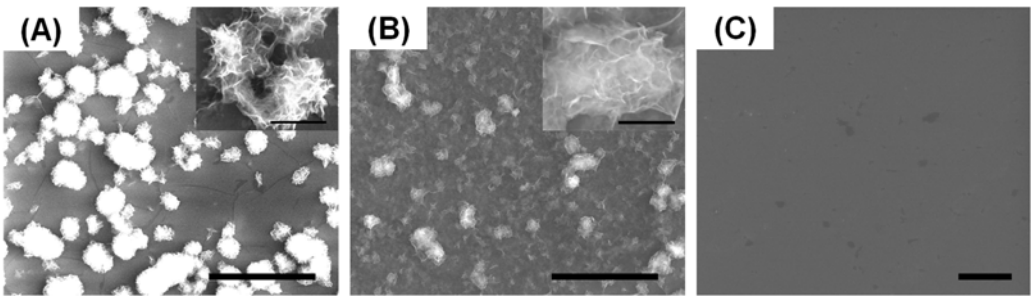

Figure 2.9 SEM micrographs of mineralized samples on day 28. The low-magnification images (×1000) of mineralized self-assembled protein matrices: (A) FN, (B) FN-EL and (C) EL. (Scale bar = 20 μm). Inset magnification (A and B): ×10,000. (Scale bar = 2 μm.) No particles were found at low or high magnification for EL.

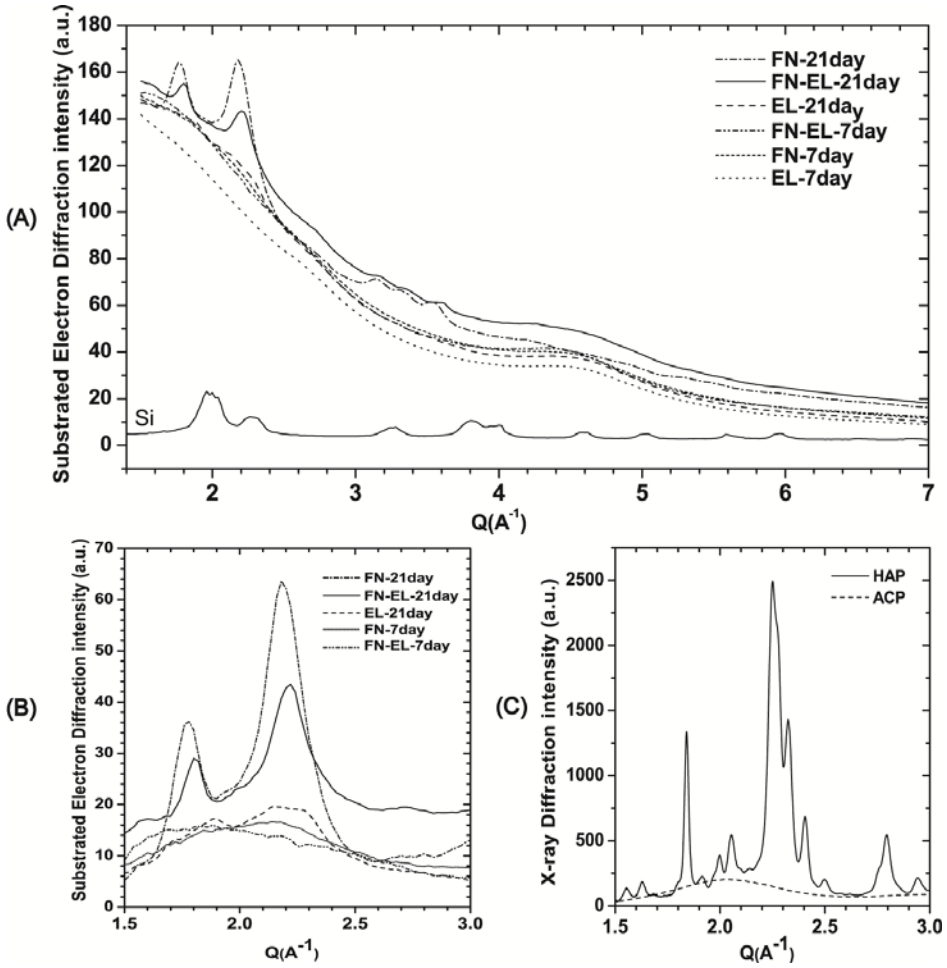

Figure 2.10 (A) Integrated TEM diffraction spectra of mineralized samples (Fig.6 and Fig.7) with Si wafer for calibration. (B) Integrated TEM diffraction spectra subtracted by the spectrum of EL-7day. (C) Synchrotron powder X-ray diffraction patterns of synthetic hydroxyapatite (HAP) and amorphous calcium phosphate (ACP). (A), (B) and (C) are plotted in equivalent units of momentum transfer *q*.

Chapter 3

Scanning Transmission Microscopy and XANES Study on Self-assembled Extracellular Matrix Protein Biomineralization *in vitro*

3.1 Introduce:

Mineralized tissues such as bone or dentin use complex, biologically regulated processes with many feedback loops to create microenvironments that induce nucleation and growth of minerals. This is often achieved at the cellular level by generating organic templates such as extracellular matrix (ECM) and in turn those organic templates control crystallization. In matrix mediated mineralization, organic molecules do not just induce nucleation and act as gross volume checks but they decide the pattern of growth of the mineral phase, selecting the faces of mineral crystallites, and the packing of these crystallites [66]. Biogenic hydroxyapatite, which is the one of most interesting minerals in biology, has been under study. Typically, biogenic calcium phosphate is not pure and non-stoichiometric, but rather is substituted by different ions as shown for the hydroxyapatite existed in bone, enamel and dentin [67-70].

The key to exploiting the materials construction strategies controlled by biomineralizing organisms is to understanding what occurs at the interface where biomacromolecules and inorganic minerals coexist [71-73]. However, early stage of biomineralization is difficult to investigate because small spatial scale and amorphous structure of mineral involved. To analyze

both protein and minerals during the bimineralization, the ultimate and most realistic approach would be to analyze the interplay between organic and inorganic components *in situ* in submicrometer-sized scale. Transmission electron microscopy is a unique technique for characterizing crystalline structure of minerals at the required spatial scale. However, structure of organic molecules associated with minerals in nanometer-sized object is much more difficult. Therefore, we need an alternative and high-resolution technique which is sensitive to both organic and inorganic molecules.

Scanning transmission X-ray microscopy (STXM), which uses X-ray near-edge absorption spectroscopy (XANES) as its contrast mechanism, is a powerful new tool that can be applied to fully hydrated biological materials [74]. STXM is a synchrotron based microscopy shown in Fig 3.1 that combined zone plate optics with the chemical specificity of XANES. As a soft x-ray imaging technique, STXM is quantifiable and imparts relatively low damage to polymeric or biological systems. Contrast in STXM is achieved by measuring differences in the photo absorption of X-rays within matter which can distinguish unlike materials due to their chemical, elemental, orientation or density variations. The absorption of monochromatic x-rays in matter generally follows a Beer's law exponential decay, which is a consequence of the imaginary part of the dielectric response function:

$$I = I_0 e^{-\mu(Z,E)\cdot\rho\cdot t} \qquad \text{Eq. (3.1)}$$

Where I_0 and I are the incident and transmitted X-ray intensities, ρ is the density, t is the thickness, and μ(Z,E) is an energy (E) and composition (Z) dependent mass absorption coefficient. The mass absorption coefficient predicts the total photo absorption and scattering of X-rays of a given material at a specific energy. A fundamental assumption of Eq. (3.1) is that the X-ray absorption processes of each photon in the absorbing material are independent of each

other. This assumption, which holds experimentally for most materials, means that X-ray transmission through any material can be determined with a linear combination of the absorbance from all of its constituent components and thus provides the mathematical description from which quantitative characterization is obtained.

Here we demonstrate the capacity of STXM for characterizing directly both the mineral and the organic content of protein fibers at the same time. The objective of this study is to determine if spectroscopic signature for mineralized protein fibers can be used to decipher the nature of protein fibers and minerals deposited on the protein fibers.

3.2 Materials and Methods:

3.2.1 Sample Preparation:

TEM grids with 100 nm thick silicon nitride windows were obtained from Silson Ltd., Northampton, England. The substrates were spin-coated with sulfonated polystyrene: SPS, $M_w \sim$ 175k from Polymer Source Inc., Dorval, Canada was dissolved in N, N-Dimethylformamide (Sigma-Aldrich, Inc., St. Louis, MO), spun-cast, and vacuum dried as described in our previous work [20, 74]. Fibronectin (FN) from bovine plasma and Elastin (EL) from bovine neck ligament (Sigma-Aldrich, Inc., St. Louis, MO) were dissolved in Phosphate-Buffered Saline (PBS) without calcium or magnesium (Invitrogen, Carlsbad, CA). Prepared SPS-coated wafers were incubated in the solutions of FN, EL, and FN-EL in PBS buffer (FN: 100 mg/ml, EL: 5 mg/ml, FN-EL: FN 100mg/ml and EL 5mg/ml) for four days at 37°C and 100% RH in 24-well dishes (BD, Franklin Lakes, NJ). After the self-assembled protein network formed, samples were rinsed three times by DI water to remove the unabsorbed protein and salts in the PBS. Samples were immersed into metastable calcium phosphate solution at room temperature to mimic the

biomineralization process. The technical details regarding the biomimic mineralzation in metastable calcium phosphate solution can be found in our previous work [75, 76].

Samples assembled onto 100nm-thick silicon-nitride membrane windows were used as sample mounts for X-ray transmission. These samples were air dried before the STXM experiments. For the wet cell samples, FN and EL were dissolved in PBS buffer with the concentration of 1mg/ml and 10μg/ml respectively and the droplets were sealed between two silicon nitride membrane windows used as protein standard.

3.2.2 Scanning Transmission X-ray Microscopy

STXM imaging and XANES spectroscopy were performed using the STXM on beamline X1A1 at the National Synchrotron Light Source (NSLS) at Brookhaven National Laboratory (BNL). The schematic is shown in Fig 3.1A. A monochromatic soft X-ray beam is focused to 50nm or less by a Fresnel zone plate [75], and the sample is scanned through the focal point in two dimensions while recording the intensity of transmitted X-rays. Single-energy images at selected energies were recorded for navigation. The image contrast results from differential absorption of X-rays depend on the chemical composition of the sample. All the recorded transmission images presented in subsequent figures were converted to optical density (OD, absorbance) images, where $\mathrm{OD} = -\ln\left(I \cdot I_0^{-1}\right)$, where I is the intensity at any pixel on the sample and I_0 is the incident intensity measured in an empty area adjacent to the sample.

Detailed information of the chemical composition of each sample was also obtained simultaneously through XANES spectroscopy near the carbon K-edge (283 eV) and calcium L-edge (350 eV). XANES spectra were generated by calculating the natural logarithm of the ratio in optical density (absorbance) of the sample and background areas. Stacks (series of images

taking at different energies) were generally conducted from the pre-edge range of energy (280 eV for C K-edge and 342 eV for Ca L-edge) to the post-edge range of energy (310 eV for C K-edge and 360 eV for Ca L-edge). The soft x-ray beam with the energy range from 270 to 8000 eV does not cause mineral sublimation through specimen heating. Samples and all microscope components are kept in a helium-filled chamber to prevent CO_2, O_2 or N_2 from absorbing X-ray photons [62, 77].

IDL 6.0 was used to align image stacks and extract XANES spectra from image stack or spot scan measurements. No further scaling, normalization or baseline corrections are applied. Thus any differences in overall intensity are due to loss of carbon or calcium, and loss or gain of a specific function group. Maps of carbon and calcium distributions were obtained by subtracting the image below the C K-edge (≈ 283 eV) or Ca $L_{2,3}$-edge (≈ 350 eV) respectively from the image of the same area above the edge.

3.3 Results and discussion

STXM enables us to obtain protein and calcium distribution maps for self-assembled protein matrices before and after mineralization. Soft X-rays of STXM can provide spatial resolution of 50 nm, which is suitable for imaging protein fibers which are micro- or submicro-size. The true advantage of STXM is that any area of interest in the image can be also analyzed to obtain the C K-edge and Ca $L_{2,3}$-edge X-ray absorption near-edge structure (XANES) spectra to provide additional information about protein and minerals at the same time. The spectral resolution is on the order of 100 meV, which is combination with their intrinsic spectral properties is sufficient to provide good differentiation of classes of biomolecules [78, 79].

3.3.1 Carbon K-edge XANES spectra of reference proteins

To distinguish the different C K-edge absorption energies of the protein and the polymer base film, standard samples were investigated. A blank SPS-coated silicon nitride membrane window was used as polymer standard. FN and EL were dissolved in PBS buffer with the concentration of 1mg/ml and 10μg/ml respectively and the droplets were sealed between two silicon nitride membrane windows used as protein standard. To compare the effects of different protein conformations between in the solution and on the surface, the self-assembled FN or EL protein fibers on SPS-coated silicon nitride membrane window was also investigated. The spectra in Fig 3.2 show which C K-edge peaks can be assigned to the C-containing components (detail shown in Table 3.2). The XANES spectrum of SPS thin film on silicon nitride membrane window has only one peak at 285.3 eV in Fig 3.2E, which is related to C=C bonds in the aromatic groups abundant in the SPS. The EL and FN solutions in PBS share the similar spectra in Fig 3.2C and D with the major peak at at 287.5 corresponding the aliphatic CH_2/CH_3 (mostly due to amino acid side chains in protein) with a shoulder peak at 286.6 eV corresponding to the phenolic C-OH. However, when EL or FN self assembled onto the SPS thin film, the major protein peak changes to 288.2 eV corresponding to amide carbonyl group (C=O) in proteins. The spectrum of FN on SPS also has two minor peaks at 287.5 eV and 289.9 eV. Protein molecules in buffer solution usually prefer to be globular conformation to lower the entropy. When the protein molecules are absorbed onto the SPS surface, the electric field created by the negative surface charge can be expected to polarize the molecule [80, 81] changing the protein conformation into a more elongate structure and thus self-assembled into the fibers. Thus we propose that the difference of conformation between globular shape and fibers might be related to the major peak shift in XANES spectra. So we can assign the peak at 288.2 eV as the

signature peak of self-assembled proteins on the surface. The disadvantage of XANES spectra is that FN and EL cannot be resolved, unfortunately, since their C K-edge XANES spectra overlap.

3.3.2 STXM images of Protein fiber at Carbon K-edge

The synchrotron-based STXM focuses a soft X-ray beam to a 50 nm spot size and photons are transmitted through our fiber samples as shown in Fig 3.1C. In this measurement, samples have been air-dried, which has the effect of shrinking the fiber height to less than a micron and enabling the soft x-rays to transmit through them. The dried proteins also exhibit a shift in absorption peak, which appears instead at 288.2 eV (point c in Fig 3.3D). The small beam is an excellent probe of the micron-scale fibers, sensitive to absorption contrast at and around the C K-edge. The morphology of samples is imaged from the variation of the optical density, as shown in Fig 3.3A for an unmineralized FN sample on SPS thin film. At 290 eV (point a in Fig 3.3D), above most resonant Carbon peaks, organic components including protein and SPS film absorb x-rays in proportion to their thickness and absorption coefficients, making fiber areas appear darker. The morphology is similar to that observed by SPM shown in Fig 3.1B. Chemical contrast can be varied by selecting the X-ray energy for the image. The SPS distribution map (Fig 3.3B) shows that the thin film is nearly uniform on the surface. In the protein distribution map of the same area (Fig 3.3C), the protein is more concentrated in the fibers than in the space between them. These types of images confirm that the fibers are composed of protein and also will allow us to co-locate any Ca after different periods of mineralization. The results have been already shown in Chapter 2, Fig 2.5.

3.3.3 XANES spectra of biominerals template on protein fibers at Calcium $L_{2,3}$-edge

In order to determine whether the chemical environment of the calcium in the fibers and particles is different, the calcium $L_{2,3}$-edge XANES spectra of mineralized protein fibers were measured. As shown in Fig 3.4, we observe that the calcium absorption (plotted as optical density) increases with the mineralization time for all of the protein fibers. Before the samples are immersed in mineralization media, no calcium absorption peaks are seen on any of the protein matrices. After 7-day incubation in mineralization media, the two main Ca $L_{2,3}$ edge absorption peaks at 349.1 eV and 352.4 eV are just discernable above the background. At day 14, the magnitude of calcium absorption increases significantly, with minor peaks preceding the main calcium $L_{2,3}$ absorption peaks appearing on the FN-containing samples. At day 21, the calcium absorption spectra for the protein matrices are very intense and distinct 100-nm scale particles are observed on FN and FN-EL. Representative Ca-dense regions are shown in Fig 3.4A and B for day 21. On EL, the calcium distribution is localized only on the protein fibers, with no distinct particles observed (Fig 3.4C).

These differences prompted further study of calcium edge XANES spectra on day-21 specimens. Reference spectra of commercial hydroxyapatite powder (HAP) and amorphous calcium phosphate powder (ACP) were also obtained by STXM. Fig 3.5D shows XANES spectra for HAP, ACP, and day-21 FN, FN-EL, and EL samples. The L_2, L_3 and various spin orbit peaks are observed. We fit all five visible peaks simultaneously to a Voigt form (constrained to fit the same width for all peaks; fit curves shown as lines) to quantify the spin-orbit peak positions and magnitudes. Significant differences are observed in the peaks near 346.9 eV, 348.1 eV and 351.3 eV. Note that the energy separation L_2-L_3 (Table 3.3) indicates that the

EL sample is an outlier, compared with FN-containing fibers and with reference minerals. The same is true for the spin-orbit splittings (a_2-a_1) and (b_2-b_1). Finally, EL and FN-EL have much lower relative magnitudes for these secondary peaks, as shown quantitatively in Fig 3.5E. The previous works [82, 83] show that the multi-peak pattern of the Ca $L_{2,3}$-edge is the result of the crystal field whose magnitude and symmetry arise from the arrangement of atoms in the first coordination sphere surrounding Ca^{2+}. Our result is strong evidence that the Ca coordination found in the mineral samples, where symmetry is reduced, is not present in the EL sample. Instead, for EL the Ca is bound in some structurally amorphous way to the proteins themselves, a completely different situation than for FN, which yields XANES spectra very similar to those of the pure mineral powders.

3.4 Summary

In this chapter, I demonstrated that STXM is a powerful instrument to obtain protein and calcium distribution maps for self-assembled protein matrices before and after mineralization. We can use C K-edge absorption images to identify the protein fibers at 288.2 eV. And Ca $L_{2,3}$-edge XANES spectra can be used to distinguish among different Ca-containing minerals important in biomineralization process. However, the drawback of STXM is that FN and EL cannot be resolved, unfortunately, since their C K-edge XANES spectra overlap.

Tables:

Table 3.1 Approximate energy ranges for primary absorption peaks of different functional groups at the carbon K-edge [84-87]

Energy (eV)	Functionality
284	Quinine
284.9-285.5	Unsaturated/aromatic
285.8-286.4	Aromatic C-OH
286.6	Phenolic C-OH
287.1-287.5	Aliphatic
287.7-288.6	Carbonyl
289.3-289.6	Alcohol
290.3-290.6	Carbonate

Table 3.2 Peak assignments and energy position (in eV) for C K-edge XANES of samples in Fig 3.2

Sample in Fig 4.1	**Peak assignments (eV)**				
	Aromatic C=C	Phenolic C-OH	Aliphatic CH_2/CH_3	Amide carbonyl C=O	Alcohol C-OH
EL-SPS	285.3	—	—	288.2	—
FN-SPS	285.3	—	287.5	288.2	289.6
EL-W	—	286.6	287.5	—	—
FN-W	—	286.6	287.5	—	—
SPS	285.3	—	287.5	288.2	—

Table 3.3 Energy splitting (Δ, eV) of calcium $L_{2,3}$ absorption edge

Sample	L_2-L_3	Δ_3 (eV)	Δ_2 (eV)
HAP	3.28	1.02	1.00
ACP	3.33	1.05	1.02
FN 3W	3.25	1.04	1.00
FN-EL 3W	3.26	1.07	0.99
EL 3W	3.20	1.11	0.98

Figures:

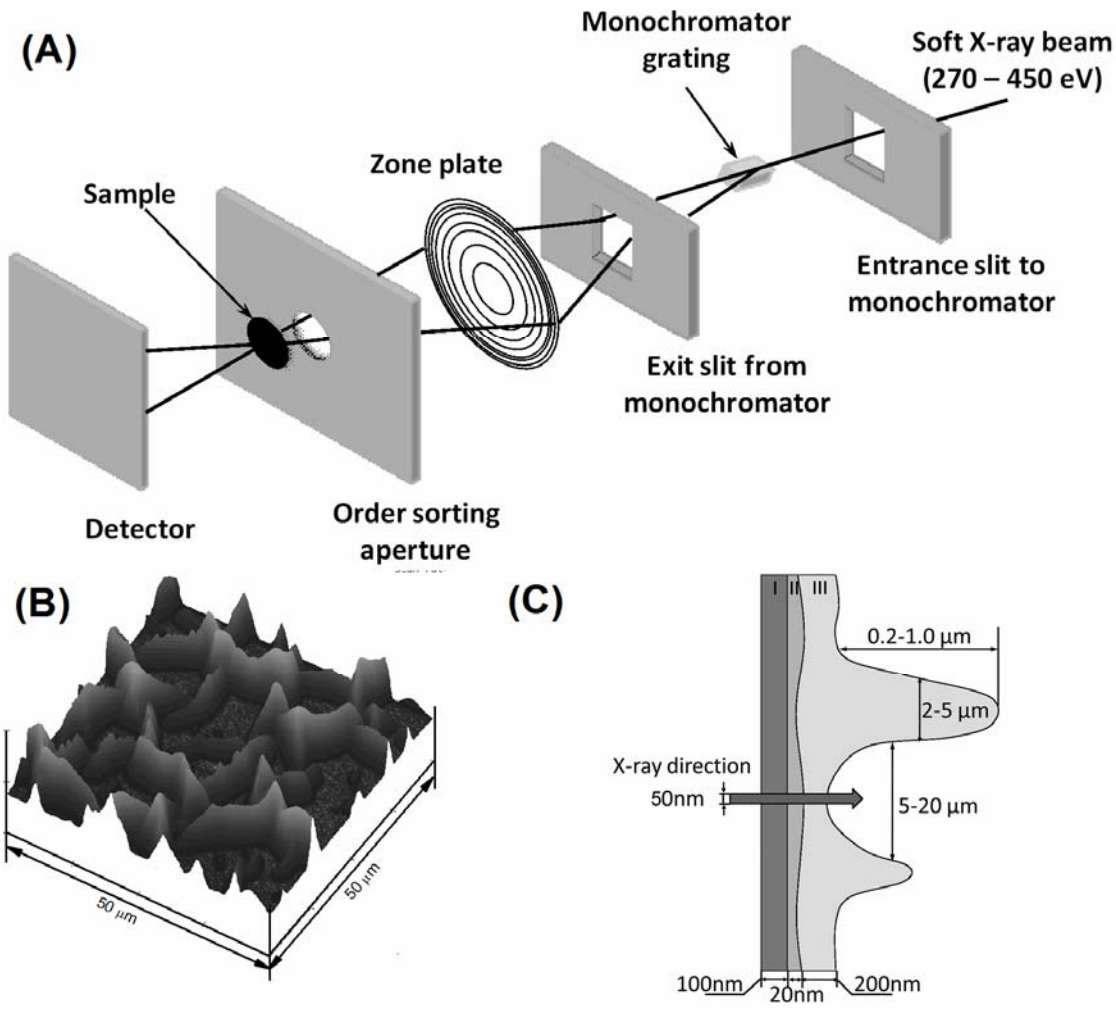

Figure 3.1 (A) Schematic set-up of STXM at X1A beamline at Brookhaven National laboratory. The monochromator selects the desired energy. The zone plate focuses the monochromatized beam to a 30nm spot. Order sorting mirrors are used to block higher energy photons and an oder sorting aperture is mounted downstream of the zoneplate to block higher orders from the zone plate. The sample is placed in the focal spot and raster scanned for image acquisition. (B) 3D AFM image of protein network (C) Schematic cross-section of the protein fiber network self-assembled upon a thin protein layer on spin-coated SPS silicon nitride window.

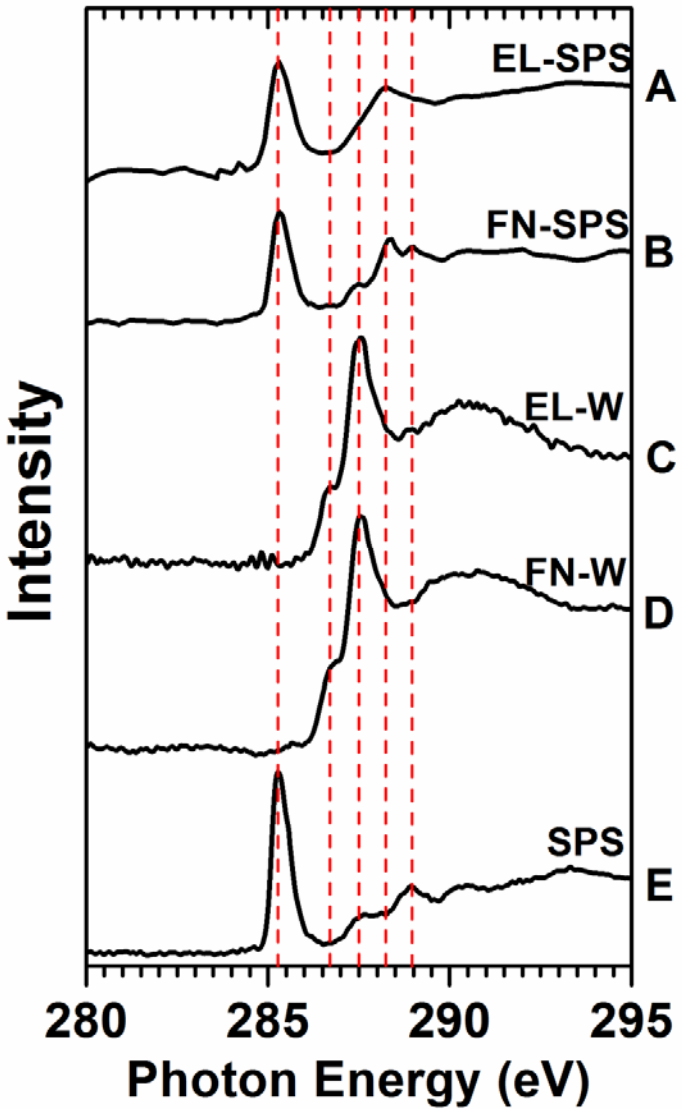

Figure 3.2 Carbon K-edge XANES spectrum of (A) EL on SPS thin film, (B) FN on SPS thin film, (C) EL solution in PBS, (D) FN solution in PBS and (E) SPS. The red dash lines indicate the energies of 285.3 eV, 286.7 eV, 287.5 eV, 288.2 eV and 288.9 eV (from left to right)

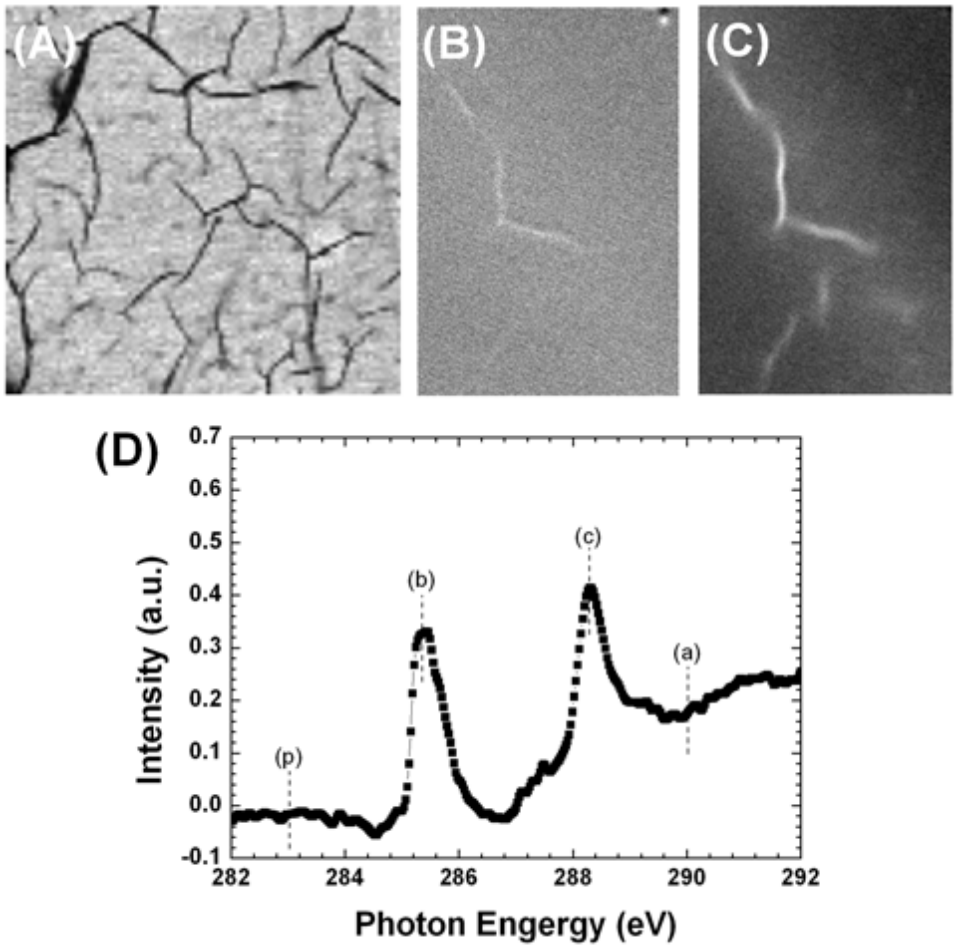

Figure 3.3 STXM image and Carbon K-edge XANES spectrum of non-mineralized protein matrix confirmed that protein fibers were deposited on the surface of SPS thin film. (A) STXM of FN-EL image recorded at 290 eV (point a). (Scale bar= 10 μm). (B) SPS distribution mapping of single protein fiber was obtained by ratioing point b (285.3 eV) and p (283.0 eV). (Scale bar= 2.5 μm). (C) Protein concentration mapping of single protein fiber was obtained by ratioing of point c (288.2 eV) and p (283.0 eV). (Scale bar= 2.5 μm). (D) Carbon K-edge XANES spectrum labeled with point p, a, b and c.

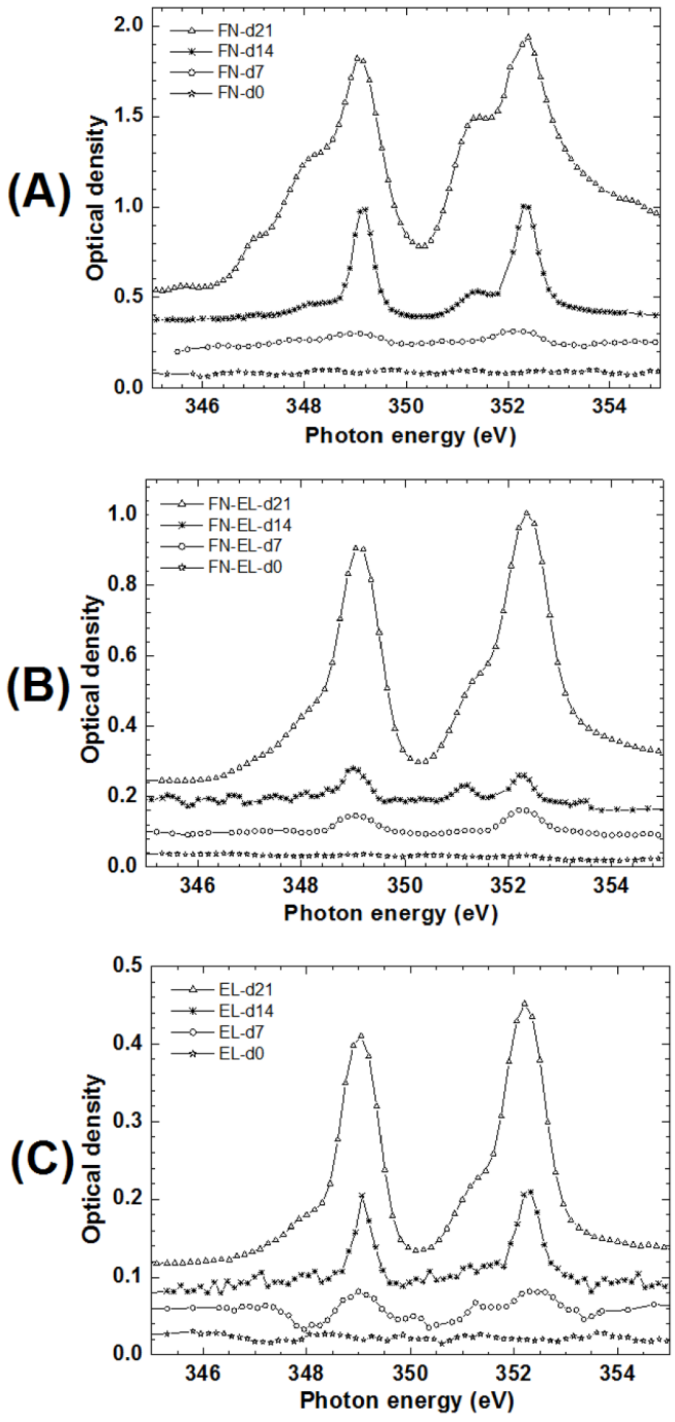

Figure 3.4 Calcium L-edge XANES spectra acquired using STXM on different self-assembled protein matrices at day 0, day 7, day 14 and day 21. (A) FN; (B) FN-EL and (C) EL.

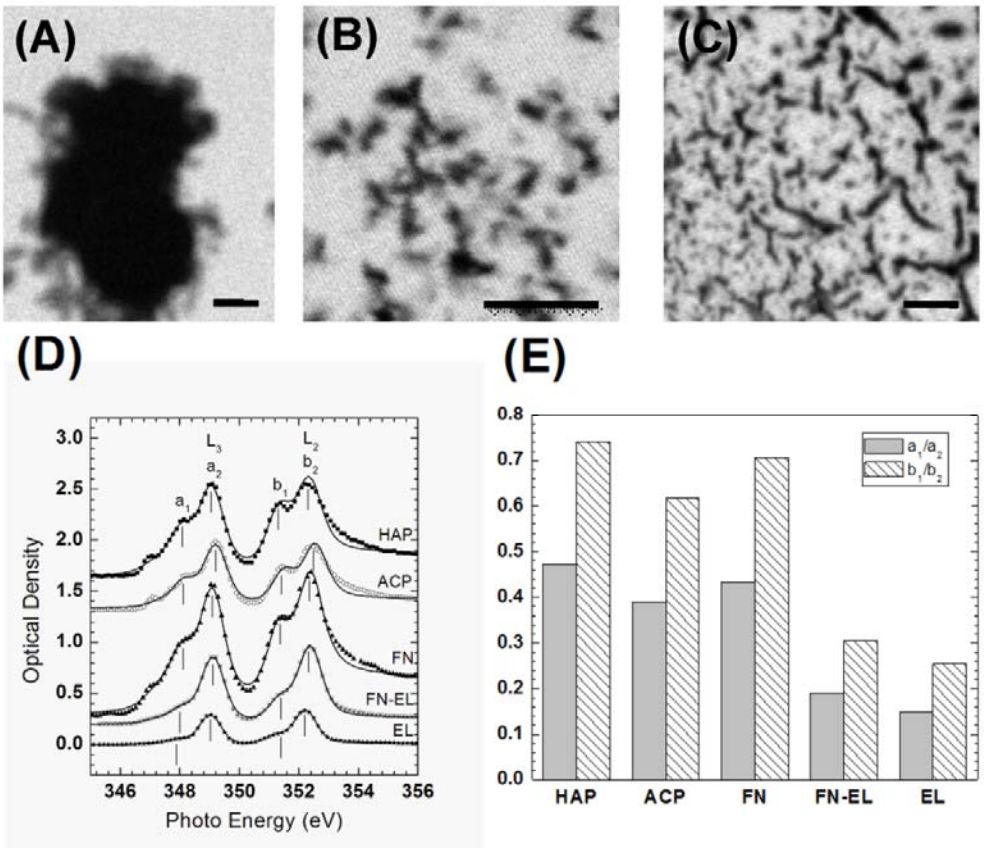

Figure 3.5 STXM images of self-assembled protein matrices after 21-day incubation in mineralization solution recorded at calcium-edge energy of 347.6 eV showed the different morphology of calcium complex. (A) FN; (B) FN-EL and (C) EL. (scale bar = 2.5 μm) (D) Calcium L-edge XANES spectra from different 21-day mineralized protein matrices acquired at X1A compared with synthetic HAP and ACP. (Symbols indicated the raw data and lines indicated the fitted data). (E) Integrated area ration of calcium $L_{2,3}$ absorption peaks with minor peaks.

Chapter 4

Effects of Type I Collagen Combined with Noncollagenous Proteins on Hydroxyapatite Formation *in vitro*

4.1 Introduction

Biomineralization refers to the formation of inorganic materials by living organisms, which is a widespread and important biological process [88]. It is a subject of constant scientific interest due to the broad potential application in materials and biomedical engineering. Extracellular matrix (ECM) plays critical roles during biomineralization, not only providing a space to deposit mineral crystals but also conducting nucleation, crystal morphology and orientation of the biominerals with regard to hard tissue growth [89, 90]. Although numerous studies have been designed to elucidate the mechanisms that determine where, when, and how mineral crystals form in ECM of different hard tissues *in vitro* or *in vivo* [91-93], the fundamental mechanism of ECM-mediated biomineralization in hard tissues remains uncertain.

As the most abundant component in ECM of hard tissues, the mineralization of type I collagen is of special interest for the understanding of the mechanism underlying biominerlization in bone and dentin as well as for the synthesis of improved bone grafts and maybe for the design of other medical devices. Type I collagen constitutes more than 90% of the total organic matrix of bone or dentin [94], which exists as an extended triple helix that

aggregates *in vivo* to form fibrils [95, 96]. These fibrils exhibit a banding pattern resulting from the alternation of hole (or gap) regions and overlap regions. The long-standing proposed theory is that initial mineral deposition occurred at the hole zones [97-99]. However, the more recent controversy has been arisen to include the noncollagenous matrix proteins (NCPs) associated with the Type I collagen during the biomineralization. A proposed mechanism for mineral formation in bone involves the NCP nucleator binding to type I collagen and then initiating mineral deposition [100, 101]. And Gajjeraman et al. [102] also claimed that the NCPs of hard tissues are intimately involved both temporally and spatially in mineralization, including the processes of mineral nucleation and control of crystal growth. To better understand the mechanism of ECM-mediated biomineralization in hard tissues, it is important to determine whether the collagen itself causes the biomineralization to start or whether NCPs associated with the collagen are regulating biomineralization.

In this paper, we successfully present an approach to mimic the ECM *in vitro*. Using a charged polymer substrate we show that the pure type I collagen and collagen binding with two noncollagenous proteins (NCPs), fibronectin and elastin, self assemble into a common fiber network. Our previous work has demonstrated that those two NCPs have different functions during biomineralization [74]. To improve the understanding of the interaction between organic molecules and biominerals during the initial stage of biomineralization, we demonstrate complementary surface sensitive techniques to study the process of biomimetic mineralization from the earliest stages. By exposing the fibers to calcium phosphate solution at physiological pH and ionic concentration, we are able to track the subtle changes of mechanical property of protein fibers by scanning probe microscopy (SPM) and shear modulation force microscopy

(SMFM). Grazing incidence X-ray diffraction (GIXD) is used to determine crystalline property of mineral.

4.2 Materials and methods

4.2.1 Surface preparation

Polished 200 μm thick ‹100› Silicon wafers (Wafer World Corporation, West Palm Beach, FL) were cut into 1×1 cm^2 size and spin-coated with Sulfonated Polystyrene: SPS, $M_w \sim 175k$ (Polymer Source Inc., Dorval, Canada) which was dissolved in N, N-Dimethylformamide (Sigma-Aldrich, Inc., St. Louis, MO), spun-cast, and vacuum dried as described in our previous work [57]. Type I collagen (COL) from rat tail, Fibronectin (FN) from bovine plasma and Elastin (EL) from bovine neck ligament (Sigma-Aldrich, Inc., St. Louis, MO) were dissolved in Phosphate-Buffered Saline (PBS) without calcium or magnesium (Invitrogen, Carlsbad, CA). Prepared SPS-coated wafers were incubated in the solutions of COL, COL-FN and COL-EL in PBS buffer (COL: 100 μg/ml, COL-FN: COL 100 μg/ml and FN 100 μg/ml, COL-EL: COL 100 μg/ml and EL 5 μg/ml) for four days at 37°C and 100% RH in 24-well shaped dishes (BD, Franklin Lakes, NJ). After the self-assembled protein network formed, samples were rinsed three times with DI water to remove the unabsorbed protein and salts in the PBS. Samples were rinsed twice by DI water to remove unabsorbed protein and immersed in metastable calcium phosphate solution as described in Sikiric's paper [57].

4.2.2 Scanning Probe Microscopy (SPM) and Shear Modulation Force Microscopy (SMFM)

The early-stage imaging and height measurements were made using a Dimension 3100 SPM (Veeco, Santa Barbara, CA) in contact mode with a silicon nitride tip (Veeco, Santa Barbara, CA). The sample was kept in a 35 mm petri-dish (BD, Franklin Lakes, NJ) with PBS to maintain the fibrillar protein structure. The fiber height was evaluated using SPM cross-sectional images by measuring fiber heights referenced to flat base regions as shown in Fig 4.1. Use of the SMFM, which is based on the SPM, to measure shear modulus response relies on lateral modulation of the cantilever buried ~3 nm deep into the sample, and measurement of the amplitude response, as detailed previously [17, 20].

4.2.3 Grazing Incidence X-ray Diffraction (GIXD)

Synchrotron grazing incidence X-ray diffraction (GIXD) experiments were carried out on NSLS X6B Beamline at BNL. The x-ray wavelength $\lambda = 0.6525$ Å, and spot size with 0.25 mm high and 0.4 mm wide, were used. The sample was mounted on a goniometer head at a distance of 150 mm from the detector screen. Grazing incidence diffraction patterns with an incident angle of 2.0º were recorded using an X-ray CCD detector (Princeton Instruments, Trenton, NJ). The detector geometry (distance from sample, tilt of detector, center of diffraction pattern) was calibrated using a transmission diffraction pattern of standard Al_2O_3 plate. Measurements were made in air on dried samples.

4.2.4 Transmission Electron Microscopy (TEM)

Samples on Silicon Nitride membrane windows were observed after 7-day and 21-day mineralization intervals by using a JEOL JEM2100F high-resolution analytical TEM (Center for

Functional Nanomaterials, BNL) operating at 200 kV. The electron diffraction patterns of the particles were recorded by using a selected-area aperture allowing observation of a circular area of 1.36-μm diameter. Caution was taken regarding the size and thickness of the examined aggregates, because these parameters may influence the quality of the diffraction patterns.

4.2.5 Scanning Electron Microscopy (SEM)

SEM measurements (Helios Nanolab, FEI, Hillsboro, OR) were conducted at the Center for Functional Nanomaterials, BNL. The morphology of crystals on the protein matrices after 28 days in calcium phosphate mineralization solution was investigated at 15 kV acceleration voltage and 4 mm working distance.

4.3 Results and discussions

4.3.1 Self-assembled matrix formation

After 4 days of incubation at 37ºC, proteins from solution are absorbed and self-assembled on the SPS-coated silicon surface. As seen in Fig 4.2A-C, either FN or EL with COL self-assembles into fiber networks, of slightly different dimension and fiber height shown in Fig 4.2D (black bar). The mechanical property of different protein fibers were measured at the same time by SMFM shown in Fig 4.2D (red bar). The relative modulus of COL-EL fiber (1.00) doesn't change compared with COL which is 1.00. However, after combining with FN, the relative modulus of COL-FN (1.14) increases by 14%.

4.3.2 Early stage of mineralization

To investigate the subtle changes during early stage of mineralization, the fiber height was measured at different mineralization times from 0 hr to 12 hr after the protein matrices were

immersed into calcium phosphate mineralization solution. In Fig 4.3A, fiber height increases linearly with mineralization time for all three protein fibers during the first 12-hr mineralization. The result shown in Fig 4.3B indicates that the increase rate of fiber height of COL-FN (0.0059 $\mu m \cdot hr^{-1}$) is similar to that of COL (0.0068 $\mu m \cdot hr^{-1}$). However, the fiber height of COL-EL increases slightly quicker, at 0.0114 $\mu m \cdot hr^{-1}$, than those of COL and COL-FN during the first 12-hr mineralization. The effects of specific mineral ion on the protein fibers were discussed in the Chapter 2.3. We demonstrated that only specific mineral ions such as calcium or phosphate ion are required for the time-dependent changes of protein fiber height.

Shear modulation force microscopy (SMFM) measurements were done to monitor the relative change in modulus of the protein fibers from 0 hr to 12 hr after the protein matrices were immersed into calcium phosphate mineralization solution. In Fig 4.4, we show the modulii of protein fibers as a function of mineralization time, where the scale is relative to the response of non-mineralized COL. From the figure we see that the modulii of all the protein fibers increase linearly with mineralization time. However the increase rate of the COL-EL protein fibers is slightly higher than those of the COL and COL-FN protein fibers.

4.3.3 Late stage of mineralization

The late-stage of mineralization on three different protein matrices were characterized by Synchrotron Grazing Incidence X-ray Diffraction (GIXD). The synchrotron X-ray diffraction patterns of three different protein matrices with 7-, 14-, 21- and 28-day mineralization are shown in Fig 4.5A-C. As a reference, the diffraction peak positions of Hydroxyapatite (HAP) are plotted in Fig 4.5D. The results show that minerals formed on the protein matrices are HAP with different crystallinity degree and the area underneath the peaks of three different protein matrices increase with mineralization time in different rates shown in Fig 4.6. On day 7, small and broad

diffraction peaks corresponding to the (002) and (112) planes can be only observed on COL-EL. From day 14 to day 21, the peak area of COL increases more rapidly than those of COL-EL and COL-FN. And more diffraction peaks appear on the spectra of three protein matrices, corresponding to (211), (300), (202) and (130) planes of HAP. On day 28, the peak areas of COL-FN and COL-EL are larger than that of COL. The final crystallite size of HAP formed on protein matrices after 28-day mineralization, estimated by Scherrer's equation using (002) peak [103, 104], exhibit a small crystallite size (< 13 nm) which was comparable with the crystals found in bone [61].

SEM images from the back-scattered electron signal for day-28 mineralization are shown in Fig 4.7. From the figure, we find that the scattered HAP particles deposite on the COL in Fig 4.7A. However, highly mineralized HAP particles are found on the COL-FN and COL-EL with different morphology shown in Fig 4.7B and C. Needle-shape HAP crystals uniformly cover the COL-FN surface while globular-shape HAP cluster with needle-shape crystals uniformly cover the COL-EL surface.

4.4 Conclusion

In this study, the successful use of self-assembled ECM proteins network on SPS monolayer thin film as templates for bio-mimic mineralization *in vitro* has been demonstrated. COL can self-assemble into network on SPS thin film with negative charge. After introducing the secondary noncollagenous protein such as FN or EL, the single network with similar morphology can be observed. At the early stage of mineralization, the effect of metastable calcium phosphate solution on the protein fiber was clearly established using SPM, by measuring the fiber height during the first 12 hours. The increase rate of COL-EL protein fiber is larger than

the one of COL or COL-FN. GIXD spectra confirm that the Hydroxyapatite particles can be observed only on COL-EL after 7-day mineralization. At day 28, the mineral on COL-FN and COL-EL has high crystallinity than on COL. Those results indicate that cooperative interaction between type I collagen and noncollagenous protein could be essential for the biomineralization *in vitro*.

Figures:

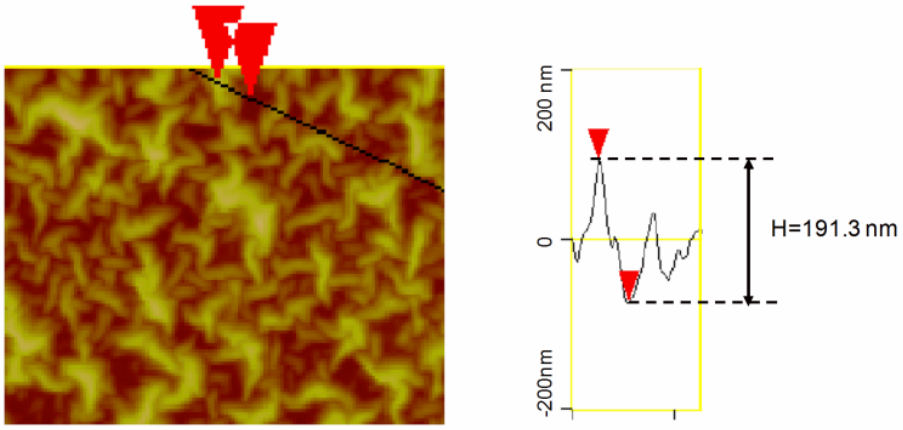

Figure 4.1 Analysis technique used to determine protein fiber height on surfaces. Height profile (right) shows the fiber height of collagen along the black line in the cross-section of SPM image (left).

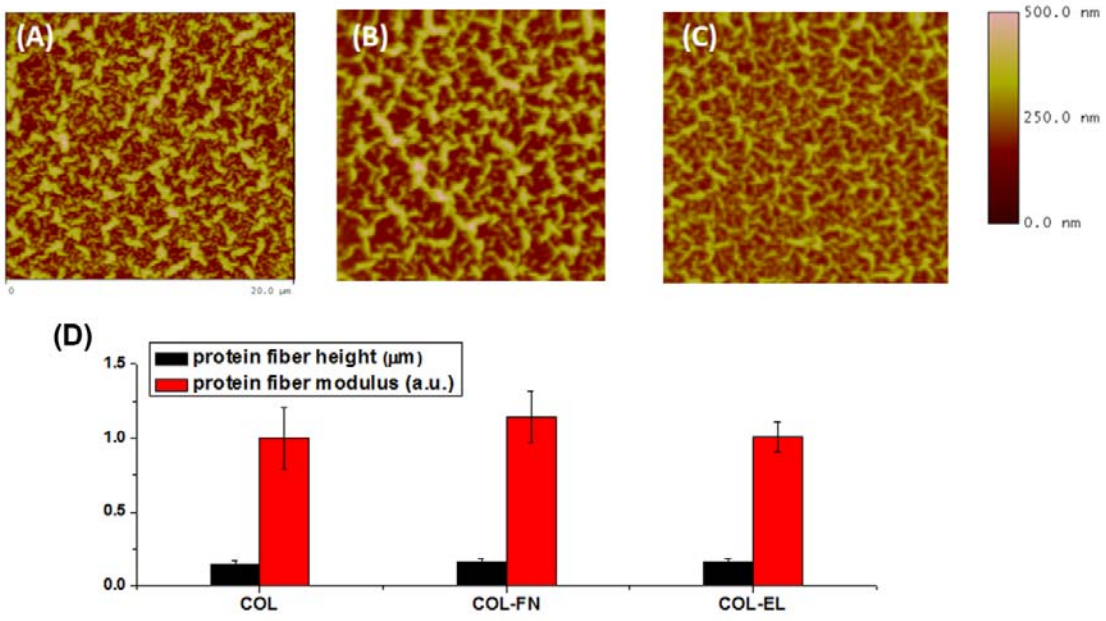

Figure 4.2 SPM images (20×20 μm) of (A) COL, (B) COL-FN and (C) COL-EL. Color bar shows the thickness scale from 0 to 500 nm. (D) Average fiber height and relative modulii of different protein fibers before mineralization.

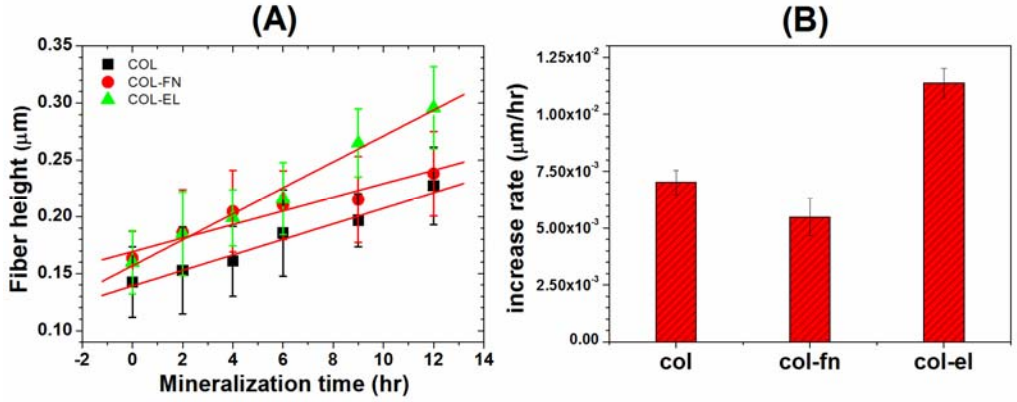

Figure 4.3 (A) Average fiber heights measured by SPM for COL, COL-FN, and COL-EL networks as function of time immersed in calcium phosphate solution. Red lines are the linear fitting by Origin 8.0. (B) Increase rate of fiber heights from different protein matrices.

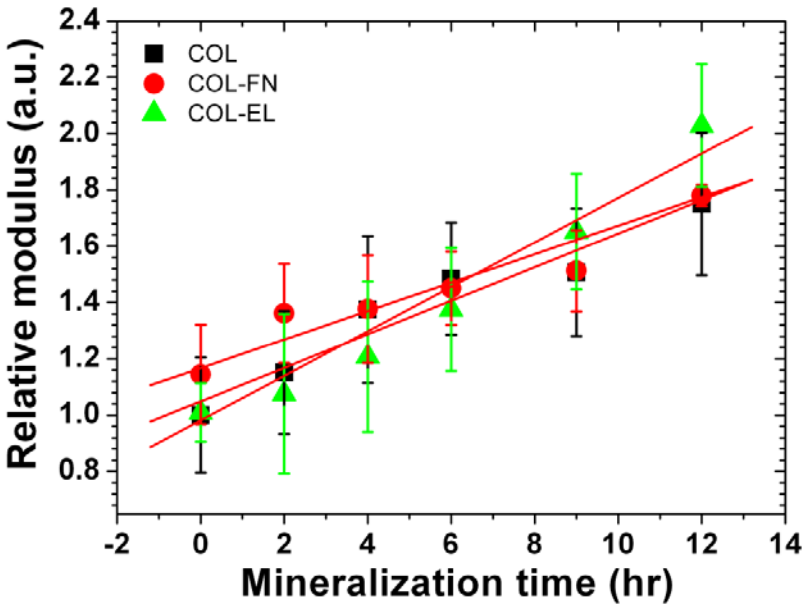

Figure 4.4 Relative modulii measured by SMFM for COL, COL-FN, and COL-EL networks as function of time immersed in calcium phosphate solution. Red lines are the linear fitting by Origin 8.0.

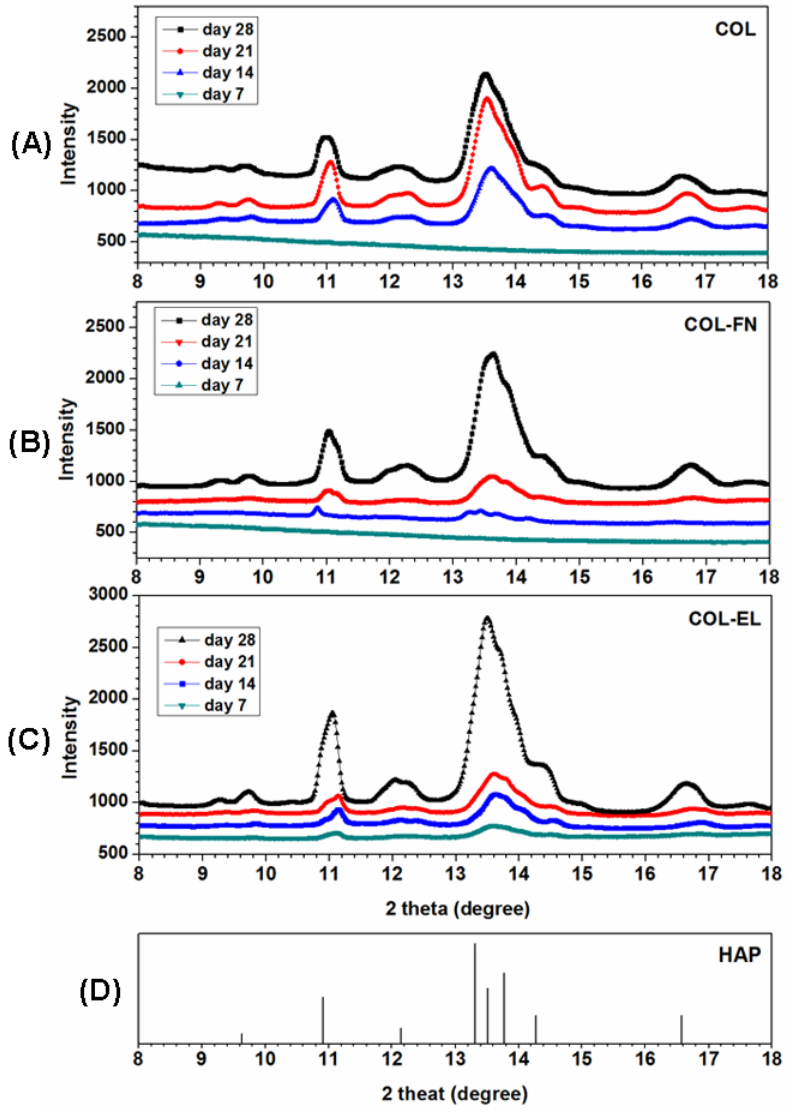

Figure 4.5 Synchrotron Grazing Incidence X-ray Diffraction (GIXD) spectra of (A) COL, (B) COL-FN and (C) COL-EL after 7-, 14-, 21- and 28-day mineralization on SPS-coated silicon wafer (Wavelength=0.65255 Å). (D) The major diffraction peaks' position of Hydroxyapatite (HAP) at wavelength=0.65255 Å. The lines in (D) from left to right corresponding to (111), (002), (210), (211), (112), (300), (202) and (130) planes respectively. The length of line in (D) indicates the intensity of diffraction.

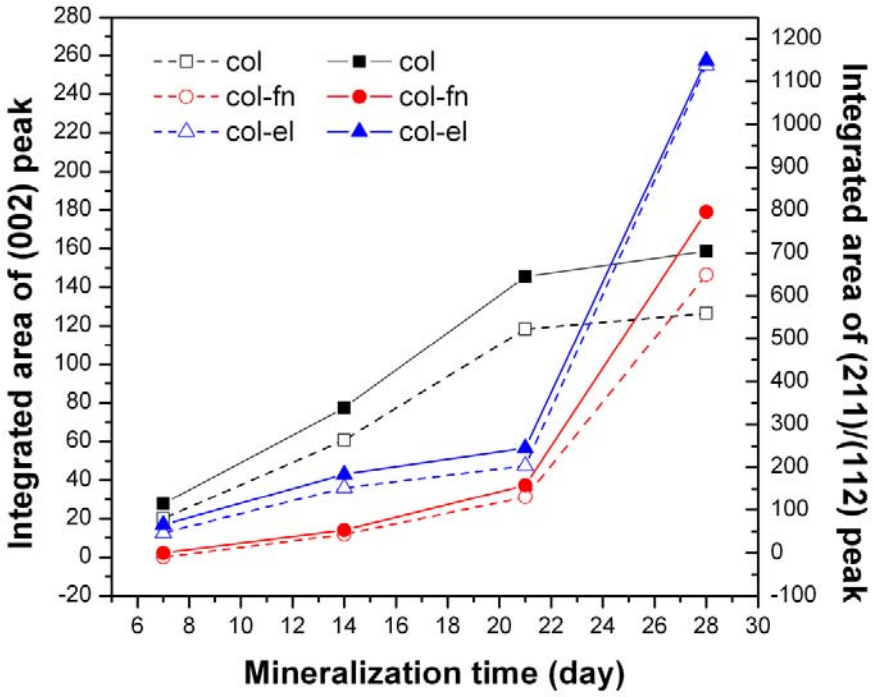

Figure 4.6 Integrated area under the peaks in GIXD spectra of different protein matrices shown in Fig 4.5. Dash lines with open symbols show the integrated area under (002) peak and solid lines with closed symbols show the integrated area under (211)/(112) peaks.

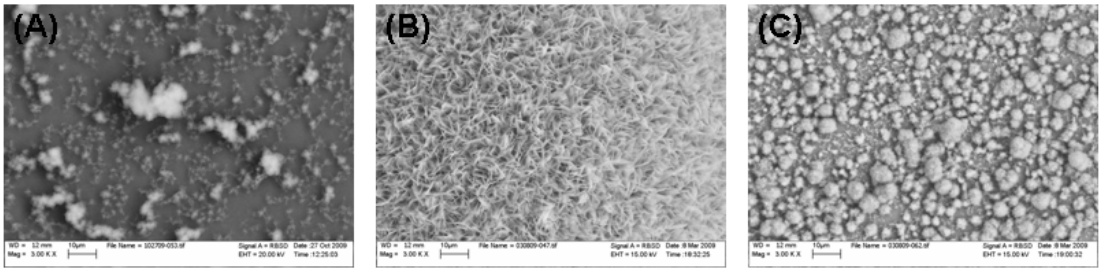

Figure 4.7 SEM images of (A) COL, (B) COL-FN and (C) COL-EL after 21-day mineralization

Chapter 5

Moderate static magnetic field promotes osteoblast differentiation and biomineralization *in vitro*

5.1 Introduction

The influence of static magnetic fields (SMFs) on biological systems has been a research topic of considerable interest for many years, since it is by now well established that SMFs can prevent decreases in bone mineral density [105] and promote healing of bone fractures [106, 107]. Studies on the effects of SMFs have been classified according to the field strength as follows: weak (< 1 mT), moderate (1 mT to 1 T), strong (1-5 T) and ultrastrong (>5 T). Even though not much influence on cell functions has been reported for weak magnetic fields [108], there are substantial evidence indicating that moderate-intensity SMFs (1mT to 1 T) are capable of influencing a number of biological phenomena such as cell proliferation [109], migration [110], orientation [111], and intracellular Ca^{2+} signaling [112]. This region is particularly interesting since it is easily achieved with rare earth magnets at room temperature, and hence easily applied in a number of therapies, especially orthodontic treatments, where electromagnets or superconducting coils cannot be used.

It has recently been proposed that many of these effects may be due to the diamagnetic properties of the cell membrane [113, 114]. Since the ECM proteins are also diamagnetic, it has

been proposed that the external magnetic field would also influence their properties. Yet, since it is very difficult to observe the ECM structure in vitro, very little data exists regarding these speculations. Pernodet et al [16] first showed that proteins, which normally constitute the extra cellular matrix, could be adsorbed from solution onto sulfonated polystyrene thin films of a minimum charge, and self assemble into fibers. Subburaman et al [115] later demonstrated that mineral deposits from biomineralization solution were template only on the fibers, and not on the flat protein films adjacent to the fibers. In this paper we show that sulfonated PS substrates could also be used to image the ECM fibrils formed from osteoblast cells and allow us to simultaneously study the effects of external magnetic fields, on the biominerlization of the cells and the underlying ECM.

Bone pathologies as well as bone loss associated with aging, has resulted in increased research efforts focused on understanding cell-matrix interactions required for promoting biomineralization. Bone tissue engineering strategies are targeted at developing new therapeutical methods in bone repair and regeneration. Application of Static Magnetic fields (SMFs) is a promising therapy to promote bone formation. Degen & Stetsula [106] demonstrated the promoting effect of SMF on fracture repair. Bruce et al. [107] reported that the mechanical strength of fractured bone of rabbits was increased by SMF exposure. Camilleri and McDonald [116] studied SMF effects using a rat model with a neodymiumion-boron magnet placed over their skull suture by a cyanoacrylate adhesive and suggested that SMF potentially affected the cell mitotic activity. Recently it is reported that SMF enhanced the radiographic and histopathological aspects of bone healing in dogs [117]. Although several studies have demonstrated its clinical and experimental usefulness for treatment of bone injuries, the underlying mechanism of how the SMFs affect the bone formation or regeneration is still unclear.

Experimental studies evaluating SMF effects *in vivo* have the limitation that the effect of magnetic field alone on bone formation cannot be demonstrated owing to various factors participating in the osteogenesis. In contrast, *in vitro* study by controlling the environmental factors (magnetic field flux and direction, pH, surface conductivity, etc) and using osteoblast-like cells, we can investigate the SMF effect on the initial steps of biomineralization and interrelation among cells, ECM and biominerals. The purpose of this study is to investigate the effects of moderate-intensity SMF (150 mT) on bone formation using negative charged polymer thin film during biomimic mineralization *in vitro*. A complementary approach is developed to compare the early- and late-stage mineralization of osteoblasts and their ECM in the absence and presence of long-term local SMF stimulation.

5.2 Materials and Methods

5.2.1 Static magnetic field exposure system

The experimental apparatus is sketched in Fig.1. An aluminum frame was constructed to support two opposing banks of adjacent Neodymium magnets, with a gap of 1 cm. A standard 24 well plate was fit into the frame and the magnetic field was measured using a Bell 640 Incremental Gauss meter. The magnetic field profile is also sketched in Fig 5.1, where we find that the field at the surface of the dish, where the cells were placed was 150mT. The entire assembly was placed in an incubator with 5% CO_2, held at 37 ^{o}C. The control samples were also cultured in a 24 well plate, placed 20cm below the shelf holding the magnet assembly, and where the field was measured to be less than 1G , approximately, that of the earth.

5.2.2 Cell culture

MC3T3-E1 cells were maintained at 37 °C (5% CO_2, humidified) in α-MEM culture medium (Thermo Scientific Hyclone, Logan, UT) supplemented with 10% fetal bovine serum (FBS) (Invitrogen, Carlsbad, CA), 100 units/mL penicillin and 100 μg/mL streptomycin (Invitrogen, Carlsbad, CA). Fresh medium was given every 2 or 3 days. Cells were seeded at an initial density of 50,000 cells/cm^2 in 24-well tissue culture plates (BD Biosciences, Franklin Lakes, NJ). For ECM visualization and proliferation assay, cells were seeded at a lower density (2000 cells/cm^2). Differentiation and mineralization were induced by the addition of 50 μg/mL L-ascorbic acid (Sigma, St. Louis, MO), and 2 mM sodium phosphate (Sigma) after 24 h of cell attachment (day 1). After different time points, cells were rinsed with phosphate-buffered saline (PBS) three times. For SEM and GIXD experiment, cells were air-dried after a series of ethanol rinsing.

5.2.3 Proliferation Assay

Numbers of cells that were growing with or without SMF exposure on day 0, 1, 3, 5 and 7 were determined by counting cell nuclei stained with 4'-6-Diamidino-2-phenylindole (DAPI). Three different types of substrates were used for each group: glass cover slip, sulfonated polystyrene thin film, and tissue culture petri-dish (BD Biosciences, Franklin Lakes, NJ). The cell cultures were then imaged using a digital camera attached to the Fluorescent Microscope (Olympus IX51, Center Valley, PA) with 10X objective lens. 50 images of each culture were imported into Image J (available at http://rsbweb.nih.gov/ij/download.html) for cell counting. Counting was performed in 3 independent cultures for each sample.

5.2.4 Scanning Probe Microscopy (SPM) and Shear Modulation Force Microscopy (SMFM)

SPM imaging and SMFM measurements were done at room temperature on ECM fiber and living cells using a Dimension 3100 SPM (Veeco, Santa Barbara, CA) in contact mode with a silicon nitride tip (Veeco, Santa Barbara, CA). Use of the SMFM to measure shear modulus response relies on lateral modulation of the cantilever buried ~3 nm deep into the living cell or ECM fiber, and measurement of the amplitude response, as detailed previously [41, 118]. After the specific mineralization time point, the sample was immediately measured, in CO_2-independent medium (Invitrogen), with scanning force microscopy in a 35 mm petri-dish (BD, Franklin Lakes, NJ). The ECM fiber height was evaluated using SPM cross-sectional images by measuring fiber heights referenced to flat base regions as shown previously [115]. For every time point, two different samples were imaged for each time point and 30 fibers on each sample were analyzed. The error bars shown for fiber height data represent the standard deviation obtained from approximately 60 measurements.

5.2.5 Confocal laser scanning microscopy

MC3T3-E1 cells cultured for 1, 7, 14, 21, and 28 days were rinsed with PBS, fixed with 3.7% formaldehyde (in PBS), and stained with 20 μg/mL propidium iodide (in PBS) for nuclei visualization. A 1% solution of Alexa Fluor 488 Phalloidin (Invitrogen) in PBS was added to the cells for F-actin visualization. Cells immersed in PBS were imaged using a Leica Confocal Laser Scanning Microscope with a 63× objective lens.

5.2.6 Protein assay and Gene expression

Alkaline phosphatase (ALP) activity was measured on days 1-14 of the cell culture with and without SMF exposure. Cells were washed with phosphate-buffered saline (PBS) three times and lysed in the buffer solution (0.1% Triton X-100, 25 mM Tris-HCl buffer). Thereafter, cells were scraped off and transferred to eppendorf tube and centrifuged for 30 min at 10, 000 × g. The supernatants were collected and added to *p*-nitrophenyl phosphate as the substrate to react for 2 hr at 37 °C. The reaction was stopped with 0.2 N NaOH and the absorbance was determined by means of a spectrophotometer at 405 nm. The aliquote of the cell lysates was also analyzed for protein content by means of a Bichinonic acid (BCA) protein assay kit (Sigma-Aldrich, Inc., St Louis, MO), and ALP activity was normalized with total protein concentration.

The Osteocalcin EIA kit was purchased from Biomedical Technologies Inc. (Stoughton, MA) for analysis of the osteocalcin in the media. Manufacturers' protocols were followed carefully. The optical densities were determined using a microplate reader set at 450 nm. Prior to placing the substrates into cell culture petri-dish, the surfaces of petri-dish were blocked by 2% Bovine Serum Albumin (Sigma-Aldrich, Inc., St Louis, MO). This prevented cells on the surface of petri-dish not on the substrates from growing and releasing osteocalcin into the media. The total protein concentrations were quantified by means of a Bichinonic acid (BCA) protein assay kit (Sigma-Aldrich, Inc., St Louis, MO), and osteocalcin activities were normalized with total protein concentration at each time point.

To quantify levels of gene expression, quantitative reverse transcriptase polymerase chain reaction (qRT-PCR) was used. Cells were cultured as described above and lysized at the selected time points (day 14 and day 28) for their total RNA using the RNeasy Mini Kit (Quiagen, Valencia, CA). RNA was purified according to the manufacturer's protocol. Purified RNA was

quantified by UV-Vis spectrophotometer (Beckman Coulter Inc., Brea, CA) and A_{260}/A_{280} is above 1.9. In addition, a reference pool was generated by combining equivalent amounts of RNA from all the samples used from the various wells. Primers were custom designed to amplify 150 ~ 215 bp fragment within the coding sequences of osteocalcin (forward primer: 5'-TGAGGACCCTCTCTCTGCTC-3' and reverse primer: 5'-AGGTAGCGCCGGAGTCTATT-3') (Invitrogen, Carlsbad, CA). All the reactions utilized the One-Step QuantiTect SYBR Green RT-PCR Kit (Qiagen, Valencia, CA) and were performed using a Light Cycler (Roche, Branford, CT). Reaction conditions were optimized for each of the genes studied using an annealing temperature of 57°C and RNA concentration (10 ng/rxn). Each experimental run consisted of the experimental sample as well as a 5 point serial dilution of the reference pools for both genes. The calculated concentration values for the experimental samples for osteocalcin were normalized to the corresponding total RNA. Each run was replicated 3-4 times and the results are reported as average fold change ± standard deviation.

5.2.7 Scanning Electron Microscopy (SEM) and Grazing Incidence X-ray Diffraction (GIXD)

SEM measurements (Helios Nanolab, FEI, Hillsboro, OR) were conducted at the Center for Functional Nanomaterials, BNL. The morphology of crystals on the protein matrices after 28 days was investigated at 15 kV acceleration voltage and 4 mm working distance. Energy dispersive X-ray spectroscopy (EDS) was used to map the distribution of calcium and phosphate in the ECM fibers and calculate the Ca/P ratio of the minerals.

Synchrotron grazing incidence X-ray diffraction (GIXD) experiments were carried out on NSLS Beamline X6B at BNL. The X-ray wavelength $\lambda = 0.6525$ Å and spot size 0.25 mm vertical × 0.4 mm horizontal were used. MC3T3-E1 cells cultured for 1, 7, 14, 21 and 28 days on

SPS-coated Si substrates were rinsed by PBS twice and DI water twice before investigation. The sample was mounted on a goniometer head at a distance of 150 mm from the detector screen. Grazing incidence diffraction patterns with an incident angle of 1.0º were recorded using an X-ray CCD detector (Princeton Instruments, Trenton, NJ). The detector geometry (distance from sample, tilt of detector, center of diffraction pattern) was calibrated using a transmission diffraction pattern of standard Al_2O_3 plate. In addition, synthetic Hydroxyapatite (HAP) powders (Sigma-Aldrich, Inc., St. Louis, MO) as controls were investigated for reference in both glass capillary tubes (1.0 mm diam.) and as compressed powders on a blank SPS substrate [118]. The degree of crystallinity of hydroxyapatite crystals template on the cell cultures after 28 days was calculated by Debye-Scherrer's equation: $\beta_{002} \times \sqrt[3]{X_c} = K' \ (K' = 0.24)$ [103, 104].

5.2.8 Statistical analysis

Results are presented as the mean ± standard error of the mean. The statistical significance of the differences between the experimental groups was evaluated using a Student's *t*-test for unpaired values. A value of $p < 0.05$ was considered statistically significant.

5.3 Results and Discussion

5.3.1 Proliferation

To analyze the effect of the static magnetic field (SMF), we first compared the proliferation rates of MC3T3-E1 plated in induction media and exposed or not exposed to the SMF. In each group, the cells were cultured on two different substrates: sulfonated polystyrene (SPS) thin films coated onto Si wafer substrates and tissue culture petri-dish (TC) which is commonly used as the standard control. The cell density in each case is plotted as a function of incubation time in Fig 5.2. From the figure we can see that initially there is no significant

difference between any of the cell cultures, regardless of SMF exposure, on days 0 and 1, indicating that the plating efficiency does not appear to be affected by the applied SMF.

On day 3, a slight increase in the cell density for the cells exposed to the SMF relative to those which are not exposed, becomes apparent on both the SPS coated and the TC substrates. On day 5 the difference becomes much larger, with the cultures exposed to the SMF having 40% and 20%, respectively, higher cell densities on the SPS coated and TC substrates. The much larger value observed on the SPS surface indicates that the response to the external SMF is not just an intrinsic property of a particular cell phenotype, but rather also a strong function of the biomaterial on which the cell culture is plated.

On day 7 all samples were becoming confluent explaining the decrease in the overall proliferation rates and the corresponding differences in cell density between the exposed and unexposed cultures. In the inset of Fig 5.2 the cell counts are plotted on a semi-log scale from which we can calculate the doubling times. Even in the absence of the SMF, the doubling on the SPS was shorter or 19.8 ± 0.5 hr, versus 20.4 ± 0.5 hr on the TC standard. Application of the SMF further accentuates the difference between the substrates, where the doubling time was reduced to 16.9 ± 0.1 hr on the SPS substrate and 18.2 ± 0.2 hr on the TC substrates. Furthermore, we find that the data is well fit by a single exponential function starting from six hours after plating, indicating that the combined influence of the SMF and the substrate is felt by the cells almost immediately.

5.3.2 Morphology and mechanics of the ECM:

The interaction of the cells with the substrates is mediated by the extra cellular matrix that is first deposited on the surface upon which the cell attachment occurs. Hence the

morphology of the adsorbed proteins can play an important role in cell function. Pernodet et al [16] have shown that if ECM proteins are adsorbed on TC, they form a featureless flat layer. On SPS, on the other hand, when the degree of sulfonation, or the surface charge density, exceeds 12% or -0.08 C/m^2, a large increase in protein absorption occurs and the proteins can self assemble into a fibril network, where the fiber dimensions are similar to those found in the ECM formed in vivo [119]. Since the ECM proteins are difficult to image on TC, very few reports directly address the influence of the SMF on the ECM. Kotani et al [111] have demonstrated that when 1.5 mg of collagen was added into 250 μl of culture media with MC3T3-E1 cells, both the collagen and the cells were aligned when a 8T SMF was applied. Rosen [113] explained this phenomena in terms of possible diamagnetic orientation of the ECM and cell membrane proteins. In order to determine whether a moderate SMF of 150 mT, can influence the adsorbed ECM proteins, we studied the morphology of the fibers formed when the MC3T3-E1 cells were plated on the SPS coated substrates with and without the external SMF. The images are shown in Fig 5.3A, where we can see that even after day 1 the fibers formed in the applied SMF were slightly larger than those formed in the absence of the applied field. On day 3 it was clear that the applied SMF caused the ECM to assemble in a lattice with much larger dimensions. In Fig 5.3B we plot the fiber heights as a function of time and find that the height grows rapidly between days 1and 3, and then plateaus. On the other hand, integration over the volume of all the fibers formed shows that the total amount of protein is nearly identical regardless of the exposure to the SMF, at least up to day 10. Hence at early times the predominant effect of the SMF is observed mostly in the surface organization of the ECM, rather than in its production.

In Fig 5.3C we plot the modulii of the fibers formed with and without the applied SMF. In both cases we find a power law increase with incubation time, which is most likely due to

increased mineral content in the fibers as the biomineralization process progresses. From the figure we find that up to day 5 only a small difference is observed where the fibers formed in the SMF are slightly harder. After day 5 the rate of hardening is seen to increase for the fibers grown in the SMF. In Fig 5.4 we show the SEM images of the fibers after 7-day incubation, where distinct electron contrast is observed between the fibers and the surrounding materials for the sample exposed to the SMF. The fiber network is also visible in the samples which were not exposed, but the electron contrast is much smaller. EDXS mapping analysis indicates that the source of the electron contrast is calcium and phosphate, and placing a digital window on the corresponding x-ray peaks shows that, for the samples exposed to the SMF, the mineral is distributed, at this early stage, mostly inside the ECM fibers. Very little electron contrast is observed after 7 days in the samples which were not exposed to the SMF, and no biomineralized deposits are observed in the Ca or P mapping scans. These observations are consistent with the increase in the rate of hardening of the ECM fibers measured by the SPM method after 7 days. Furthermore, these results clearly indicate that as was previously reported by Ba et al [120] for fibers formed on SPS surfaces from solution, at early times, biomineralization is templated along the protein fibers.

5.3.3 Cell morphology and mechanics

In Fig 5.5 we show confocal microscope images of the osteoblasts after 1-, 5- and 7- day incubation with and without the external SMF. From the image we can see that despite the large differences in the underlying ECM, changes in the orientation of the cells is barely discernable only on day 7, when the cells appear slightly more elongated in the external field. In Fig 5.6A we plot the modulii of the MC3T3-E1 cells plated on the SPS coated surfaces, where we can see that even at day 7 there is nearly no discernable difference in the cell modulus, which is

consistent with the lack of difference in the overall cell morphology. For time longer than 7 days, the modulus of the cells exposed to the SMF begins to increase at a more rapid rate than the modulus of the cells which are not exposed, such that after 28 days the modulus of the cells which were not exposed to SMF has doubled, while the modulus of the cells that were exposed has almost quadrupled. Comparing the modulii of the MC3T3-E1 cells to a non-mineralizing clone, Meng et al [118] found a similar increase only for the MC3T3-E1 cells and no increase for the non biomineralizing clones. The even larger increase observed when the SMF is present, indicates that more biomineralization may be occurring.

5.3.4 Protein Assay and Gene Expression

In order to determine whether increased expression of proteins or genes associated with the biomineralization process are being expressed in the presence of the SMF, we also measured the amount of ALP and Osteocalcin being expressed into the media by the cells. The results are shown in Fig 5.6B, where we find only a slight increase in ALP expression relative to the total protein production before day 14. In Fig 5.6C we plot the amount of osteocalcin expressed in the media, and we find that very little is produced prior to day 14 by cells, regardless of the presence of the SMF. After day 14 though, the rate of production increases dramatically for the cells in the presence of the SMF, such that the amount of osteocalcin present in the media by day 28 is more than a factor of five larger. The effect was further confirmed using RT-PCR to measure the difference in expression of the osteocalcin gene, where we found nearly no difference in the level of expression at day 14, and an increase of nearly a factor of 6 in the expression at day 28. Comparing Fig 5.6A-C, we find that the increase in the modulus, with time and external SMF, tracks with the increased osteocalcin production and gene expression. Even though numerous instances of increased osteocalcin production due to the presence of SMF have been reported in

the literature [121], none have been larger than 50%. Here we postulate that the major difference between this paper and previous work, both in moderate and strong SMF, is the substrate upon which the cells were cultured. All prior work was conducted on TC, whereas in this paper the cultures were performed on SPS where large differences in the distribution of the biomineral deposits from very early times in the biomineralization process were observed. These effects are only possible when ECM fibers are formed to template the biomineralization, and may possibly be inducing further differentiation and gene expression in cells at later stages of the process.

5.3.5 Crystalline property of minerals

The nature of the biomineralized deposits was further investigated using glancing incidence x-ray diffraction (GIXD). The scattering intensity is plotted as a function of diffraction angle (2θ) for the cells cultured with and without the SMF present in Fig 5.7A and B respectively. From the figure, we see that in all cultures, two discernable peaks become apparent after day 7 corresponding to the [002] and the combined [211] and [112] reflections of crystalline Hydroxyapatite (HAP). The relative amount of HA on the samples can be estimated by integrating the intensity under the [002] peak, which is plotted in Fig 5.7C. From the figure we find that the functional form of the increase in mineral deposition in time is similar in both cultures, namely slow monotonic increase at early times followed by the onset of a rapid exponential increase at later times. In the absence of the external SMF the onset occurs around day 20, while in the samples cultures in the presence of the SMF, the onset occurs earlier, around day 15 and the rate of increase is much steeper. This behaviour is similar to that of the osteocalcin expression, where we had noted a large difference in expression with application of the SMF and since osteocalcin is known to be a protein involved in regulation of the biomineralization process, the sharp increase in expression around day 15 may also be

responsible for the onset of the increase in biomineralization, whereas the much more gradual increase observed in the absence of the SMF, may be responsible for the slower rate of biomineralization and the later onset.

In Fig 5.7D we plot the full width at half maximum (FWHM) of the intensity in the [002] diffraction peak. The peak width is related to the degree of crystallinity , where decreased width is associated with increased the degree of crystallinity. From the figure we find that in the absence of SMF the peak width is nearly constant till day 28, whereas when the SMF is present a continual decrease in the peak width is observed. Using Debye-Scherrer's equation, we can estimate the degree of crystallinity of HAP and find that the degree of crystallinity of HAP on the cells exposed to SMF, which is 66%, is higher than the one on the cells unexposed (37%). In Fig 5.8 we show SEM images of the mineral deposits observed at day 28, together with the EDXS spectra of a typical cluster such as the ones shown in the inset. From the image we find that at this time most of the deposits in both cultures have formed large clusters outside the ECM fibers. Even though the morphology of the clusters is similar their composition, as shown in Fig.8, the EDXS spectra is different. The clusters formed in the presence of the SMF have a higher Ca/P ratio of 1.28 versus 0.98 without the SMF, which is closer to the ideal HAP value (1.67). Hence, not only does the SMF induce the cells to produce more HAP, the products formed have a higher degree of crystallinity and Ca content.

5.4 Conclusions

In conclusion, we have found that moderate SMFs can exert a significant influence on the process of biomineralization of mouse MC3T3-E1 ostoeblasts. The magnitude of the effect is not only a function of the magnetic field or the cell phenotype, but also of the particular material

upon which the cells are plated. In this case, we plated on SPS substrates, which have been shown to induce fibrillogenesis of the ECM proteins. Since the ECM proteins are diamagnetic, changes in the morphology of the fibers induced by the SMF can be observed as early as the first day following exposure. The ECM fibers produced in the presence of the SMF are better able to template mineral deposits during the early stages of the biomineralizing process and may responsible for the 30% decrease in the doubling time of the cells observed during the same time period (days 0-5). The SMF was also observed to influence the biomineralization at later stages as well. After 15 days, cells cultured in the presence of the SMF also exhibited a large increase in the rate of osteocalcin production and gene expression, which correlated with a large increase in mineral deposition, and an increase in cell modulus. GIXD and EDXS analysis of the mineral deposits indicated that those formed in the presence of the SMF had a higher degree of crytallinity and larger Ca/P ratio. Even though the effects of moderate magnetic fields had been studied before, none of the work in vitro considered the influence of the SMF on the structure of the ECM fibers. Our ability to form these fibers has allowed us explore this additional effect and highlight its significance in the biomineralization process. The ability to simulate the production of the ECM can bring us closer to simulating the actual process which occurs in vivo.

Figures:

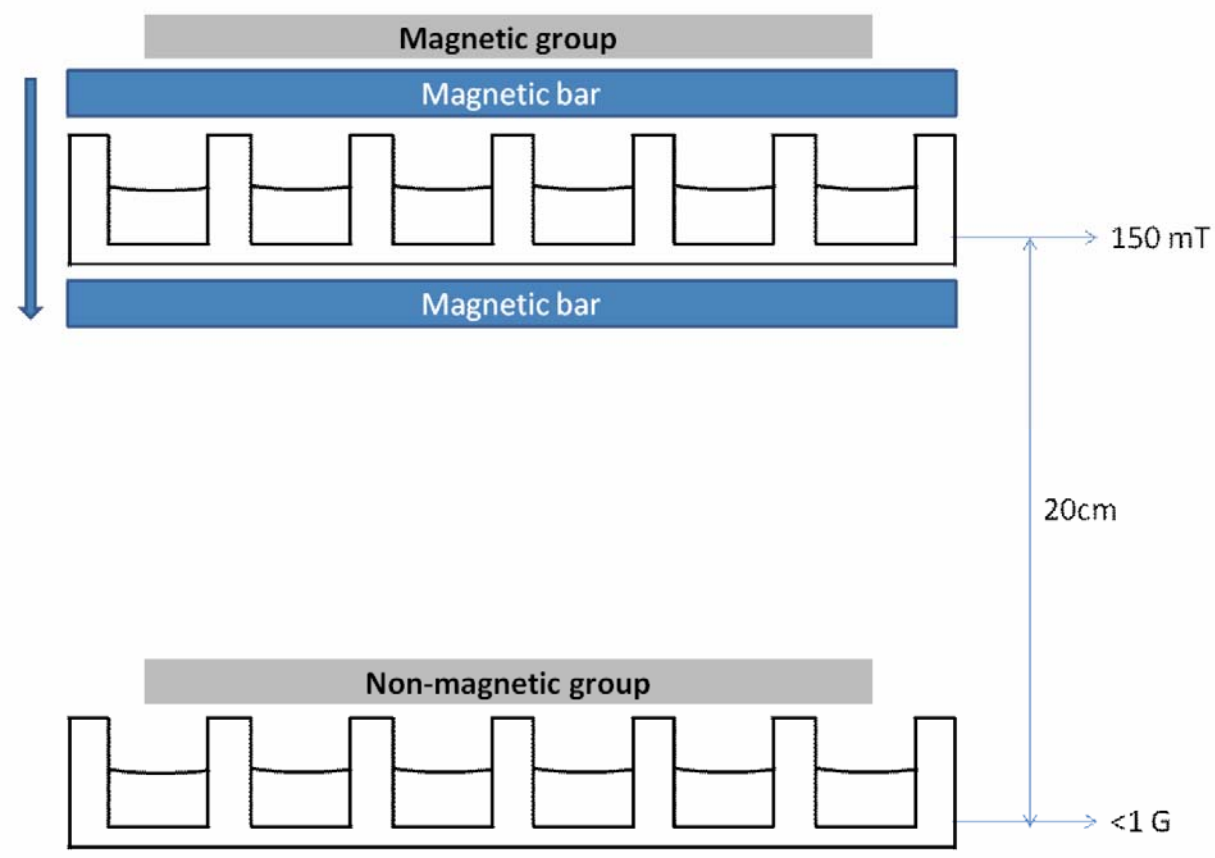

Figure 5.1 Schematic representation of magnet bar and sample placement. Arrow in the image indicates the direction of magnetic field.

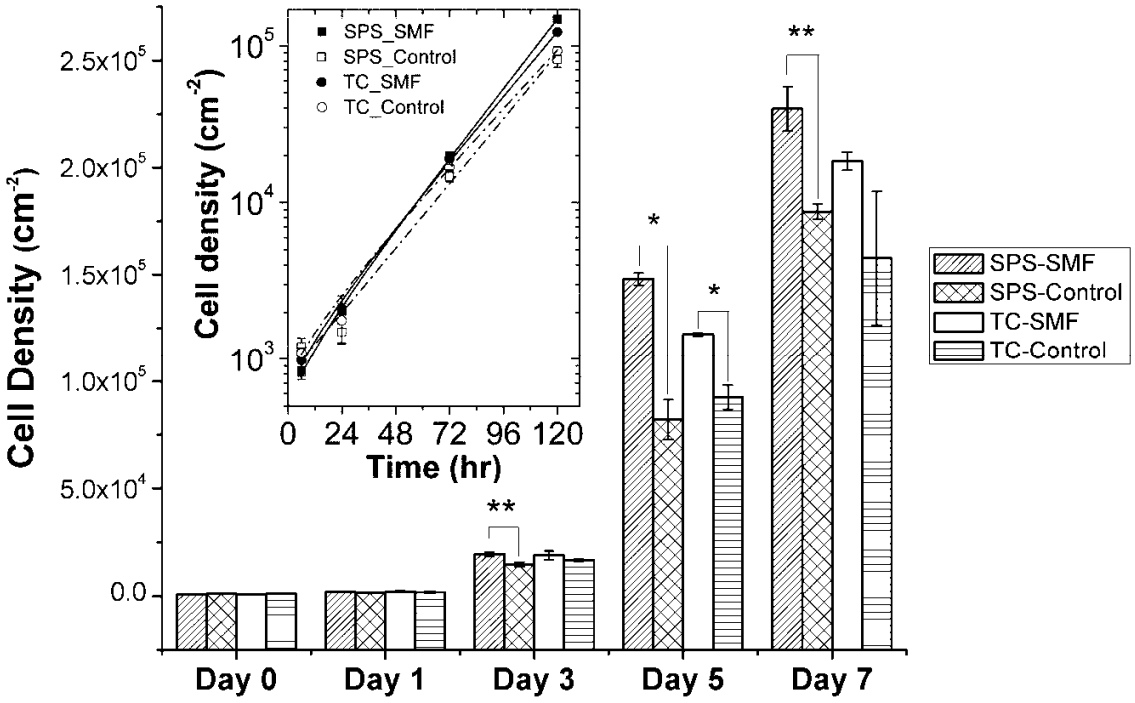

Figure 5.2 Effects of magnetic field on MC3T3-E1 cell proliferation on different substrates: Sulfonated Polystyrene thin film (SPS) and tissue culture petri-dish (TC). Significant increases of MC3T3-E1 cell density under magnetic field exposure compared with the control are indicated by * ($p < 0.05$) and ** ($p < 0.01$). Inset: doubling time fitting of cell proliferation plotted on a semi-log scale (solid line: SMF; dash dot line: Control)

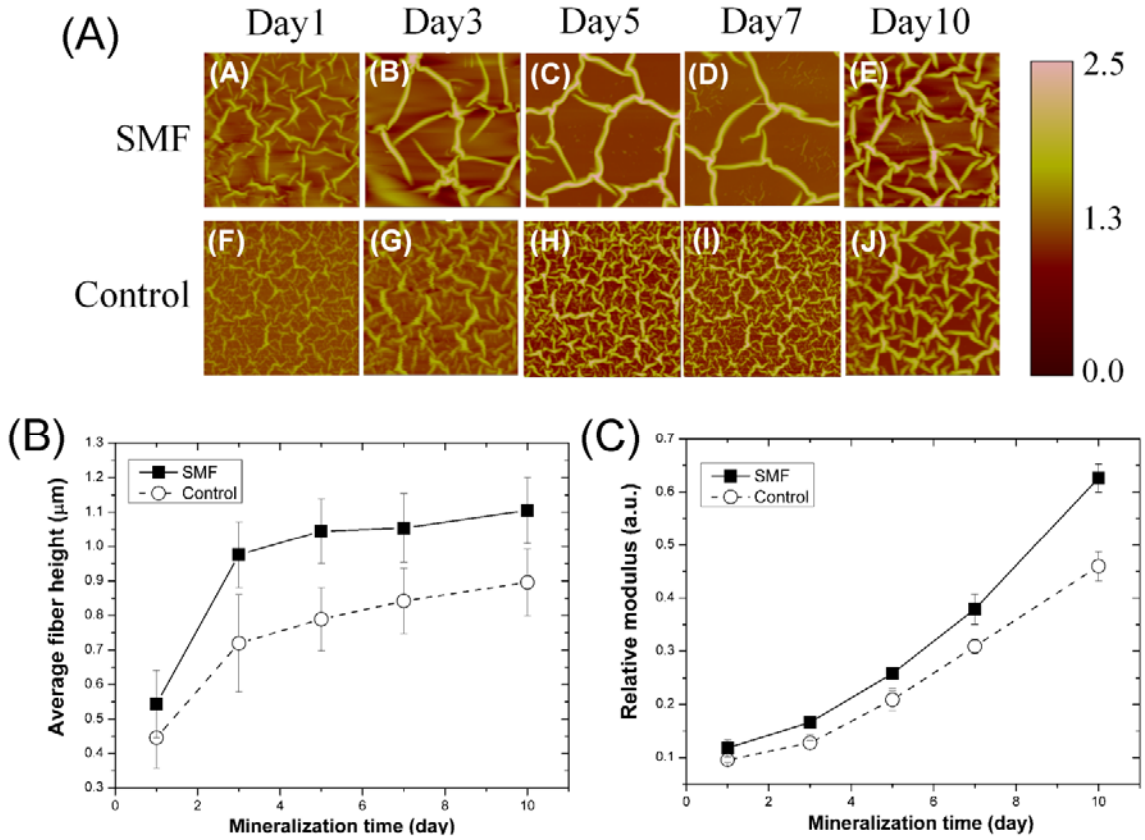

Figure 5.3 (A) Scanning Probe Microscopy topography images (50 × 50 μm) of intercellular regions on mineralizing MC3T3-E1 cells with 1-, 3-, 5-, 7- and 10-day-exposure under static magnetic field (SMF: A-E) and without static magnetic field exposure (Control: F-J). All the images share the same scale bar shown in (J), scale bar = 20 μm. (B) Mean values (±SE) of average ECM fiber heights on day 1, 3, 5, 7 and 10 from the regions shown in Figure 3. After day 10, the ECM fibers were occluded by the cells (data not shown). (C) Mean values (±SE) of the relative elastic modulus of the ECM fibers in the intercellular regions of MC3T3-E1 on day1, 3, 5, 7 and 10. Modulus values were normalized relative to the day 1 value of cells in SMF group.

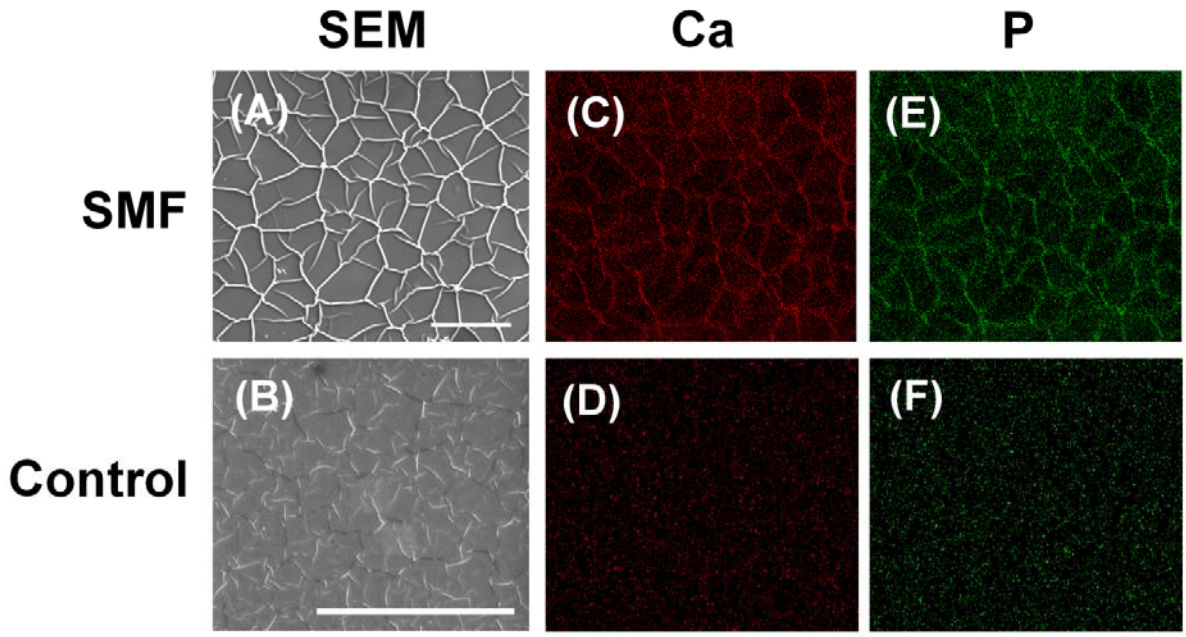

Figure 5.4 SEM images and EDXS mapping images of ECM after 7 days of mineralization. Scale bar = 50 μm.

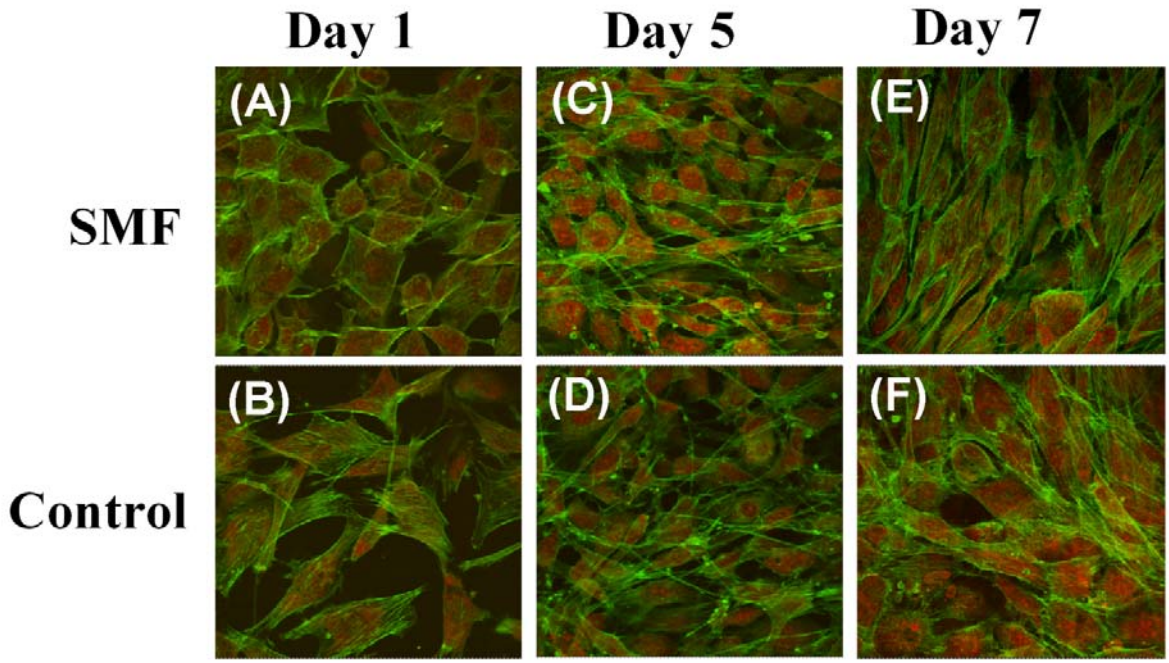

Figure 5.5 Confocal laser scanning micrographs of mineralizing MC3T3-E1 cells cultured on SPS for 1, 5, 7 days. F-actin is visualized in the green channel, and the nuclei are visualized in the red channel.

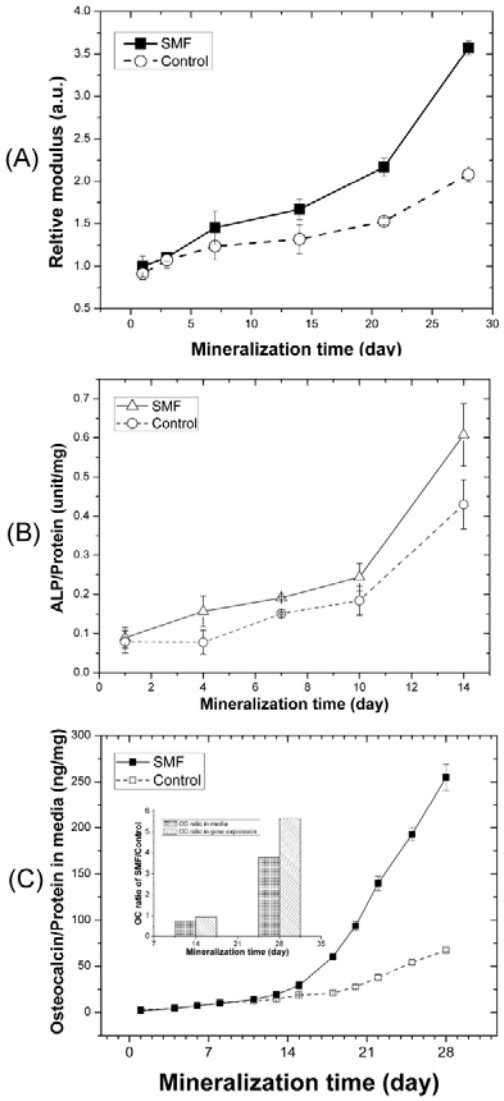

Figure 5.6 (A) Mean values (±SE) of the relative elastic modulus of MC3T3-E1 living cells in SMF group (―■―) and control group (-○-) from day1 to day 28. Modulus values were normalized relative to the day 1 value of cells in SMF group. (B) ALP activity of cell cultures on SPS thin film with mineralization time. The amount of ALP is normalized by total protein concentration. (C) Osteocalcin concentration in the media normalized by total protein from day 0 to day 30. Inset: osteocalcin ratio of SMF/Control samples.

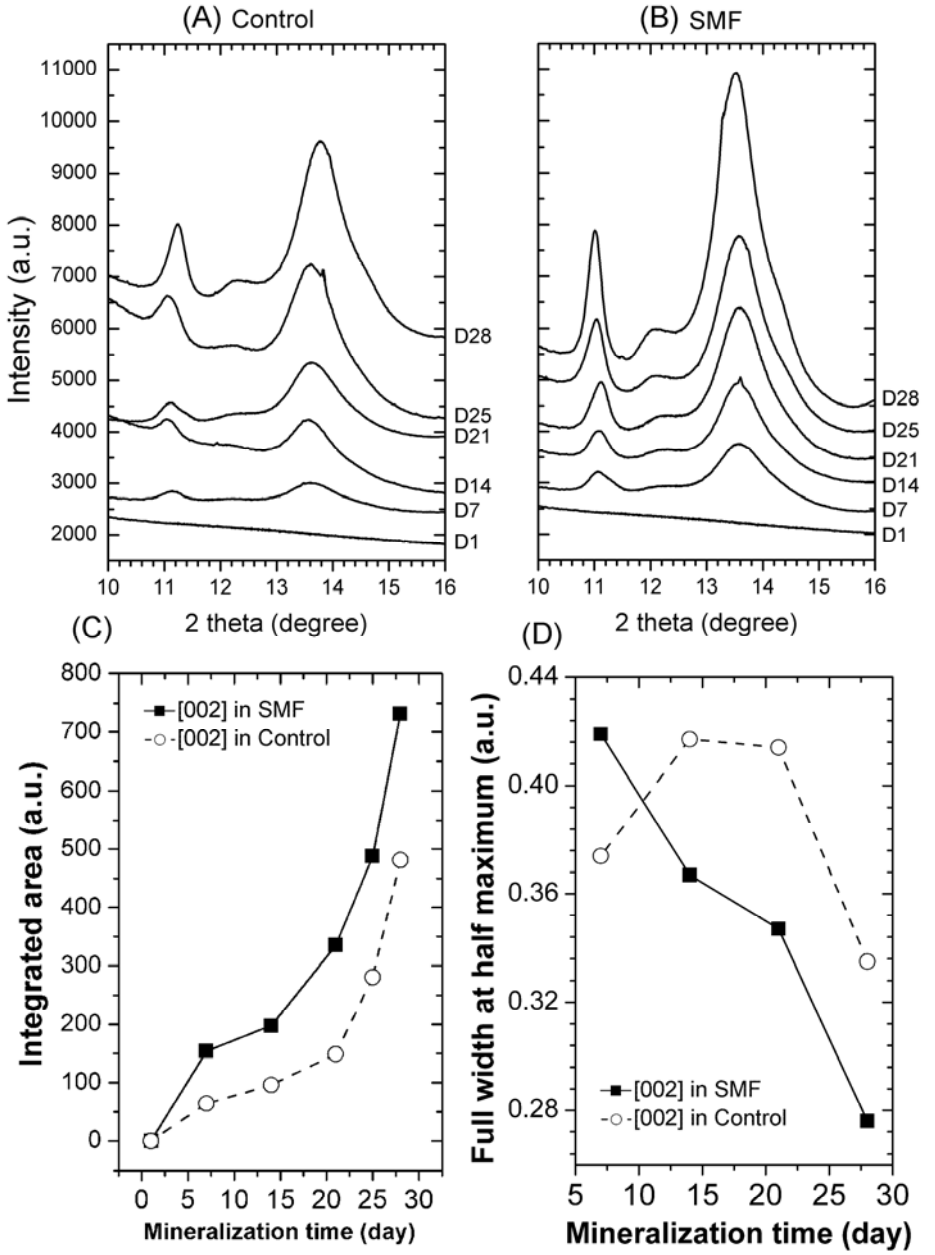

Figure 5.7 Synchrotron GIXD spectra (λ=0.65255 Å) of 1-, 7-, 14-, 21-, 25- and 28-day MC3T3-E1 cultures (A) control group: without any magnetic field exposure and (B) SMF group: continuously with magnetic field exposure. (C) Integrated area under the peaks corresponding to the [002] of HAP. (D) Full width at half maximum (FWHM) of the peaks corresponding to the [002] of HAP.

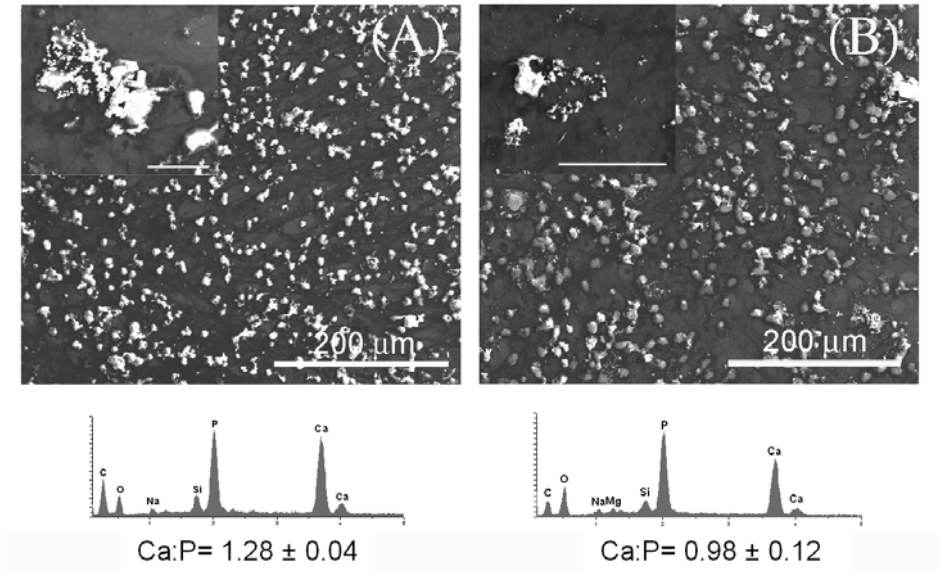

Figure 5.8 SEM images of cell culture with SMF exposure (A) and without SMF exposure (B) at day 28. Insert: EDS spectra of minerals deposited on the cell culture. Inset: high magnification images of minerals (Scale bar: 20 µm)

Chapter 6

Substrate conductivity directed the protein absorption and patterning

6.1 Introduction

The controlling and understanding of protein-surface interactions is of great interest in biomedical application such as implant medicine, biosensor design, food processing, and chromatographic separations. The adsorbed protein significantly determines the performance of biomaterials in a biological environment. Recent studies have suggested that the preservation of the native secondary structure of protein adsorbed is essential for biological application [122-124]. In order to manipulate protein adsorption and design biocompatible materials, the mechanisms underlying protein-surface interactions, especially how surface properties of materials induce conformational changes of adsorbed proteins, needs to be well understood.

Fibronectin (FN) is one plasma protein that has received much attention due to its functionality in tissue engineering. As shown in Fig 6.1, FN usually exists as a dimer composed of two nearly identical ~250 kDa subunits linked covalently near their C-termini by a pair of disulfide bonds. Each monomer consists of three types of repeating units (termed FN repeats): type I, type II and type III domains. All three domains are composed of two anti-parallel β-sheets; however, type I and type II are stablilized by intro-chain disulfide bonds, while type III

domains do not contain any disulfide bridges. The absence of disulfide bonds in type III domains allows them to partially unfold under applied force [125]. FN exists in fibrillar formation in vivo, several nanometers in diameter [126, 127]. Stimulating fibrillogenesis in vitro therefore requires large amounts of adsorbed proteins with unperturbed secondary structures which allow them to recognize the self assembling domains. Pernodet et al [16] demonstrated that sufficiently large amount of protein can be adsorbed onto the surface to initiate fibrillar self assembly into fibers only on sulfonated polystyrene (SPS) covered surfaces, where the degree of sulfonation exceeded 12%. Further experiment in our group demonstrated that only the fibrillar formations can induce biomineralization both in physiological mineralization solution [20, 74] and in cell culture [17]. Here we demonstrated that even though SPS is a necessary condition, it is not sufficient. We show that low substrate conductivity as well as proper salt concentration are also critical in sustained protein adsorption continuously.

Numerous groups have shown that selective protein adsorption on surfaces can be accomplished by grafting surface with functional groups specific interaction for different proteins [128-130]. While these methods are very effective in forming monolayer of proteins, the conformation of the proteins is often distorted by the adsorption process and the amount of adsorbed proteins is limited by the surface to be covered. Hence the process is self limiting for monolayer quantities. It is far more difficult to pattern the quantity of proteins adsorbed and the protein conformation. Kim et al have shown using cyclic voltammetry, that the amount of protein can be varied by the application of external electric fields, which can also be achieved by imposing a pattern of electrodes [131]. In this case protein multi-layers were achieved, but still not sufficient for spontaneous fibril formation. Here we show that using substrate conductivity it is possible to pattern fibril formation, and control regions where physical process can occur.

In this paper, we report that the influence of the nature of substrates on the self-assembly of FN. When SPS films with 33% sulfonation degree were spun cast onto Si wafers with a 20nm thick layer of Au, only a monolayer of proteins was adsorbed, even though the surface in contact with the protein was unchanged. In order to exclude the possibility that the SPS was in a different conformation due to interactions with the different substrates, we also conducted the same experiments where we coated Si wafers of different conductivities with 20 nm of SPS. We found that for conductivities less than 0.005 Ω·cm, similar to metals under ambient conditions, no fibers were formed, whereas fibers formed in all samples with resistivity above C=0.07 Ω·cm. Hence even though the protein solutions were exposed to surfaces with covered with polymer films of identical the charges, and chemical composition, the charge of the substrate determined the protein adsorption. In order to eliminate all other sources, such as incubation temperature, we also made patterned substrates, where an Au grating was imprinted onto Si surfaces. Separate grating were formed with spacing of 22 μm and 2.5 μm, and a single grating where the pattern was continuously reduced from 50microns to 2.5 microns was also produced. The gratings were all covered with SPS. The results showed unambiguously that only a single layer adsorbed onto the areas where Au was underneath, and a much larger amount of protein was adsorbed onto the areas where Si was beneath the coating. Furthermore, in the large areas, where the Si spacing exceeds 20microns, the standard lattice was observed. As the Si area was decreased the lattice became progressively more distorted, till the protein from a sinusoidal like pattern. All fibers were then exposed to biomineralizing solutions, and the effects of fiber morphology on the biomineralized deposits were explored. The data indicate that the patterns just need to differ in electrical conductivity, rather than surface chemistry, we propose that the creation of transient image charges, due to incomplete charge screening, may be responsible for sustain the driving

force for continual protein absorption. These factors allow one to pattern regions of different conducting properties and for the first time patterns physiologically relevant protein structures. Here we show that we can achieve patterned biomineralized regimes, both with plasma proteins as well as osteoblast induction in a simple and robust manner without additional fictionalization or application of electrochemical gradients.

6.2 Materials and Methods

6.2.1 Au/Si pattern preparation

Fig 6.2 shows the schematic procedure to prepare Au/Si pattern. To prepare the Au/Si gratings, polished 200 μm thick ‹100› Si wafers were spin-coated with S1811 photo resist (Shipley Company, Marlboro, MA) followed by post bake at 110 °C for 45 s. The substrates with photo resist were exposed under UV using a Mask Aligner (MJB-3 UV, Suss MicroTec Inc., Waterbury Center, VT) for 6 sec. Post-exposure bake in all cases was 110 C for 2 min. The development solvent of MF312 and H_2O (1:1) was used for 45 sec, followed rinsing by DI water, and drying by nitrogen. Then the substrates were coated by Chromium with 5 nm followed by gold with 20 nm using E-beam evaporator (75 vacuum deposition system, Kurt J. Lesker, Philadelphia, PA). After that, the substrates were sonicated in Acetone for 10 min to do lift-off, followed rinsing by methanol and drying by nitrogen gas.

6.2.2 Sample preparation and protein absorption

Polished 200 μm thick ‹100› Si wafers with different conductivity were obtained from University Wafer Corporation, South Boston, MA. The conductivity of Si wafer was measured using Sigatone Pro4 4-point probe (Sigatone Co., Gilroy, CA). The Si wafers with different

conductivity and Au/Si patterned wafers were spin-coated with Sulfonated Polystyrene: SPS, M_w ~ 175k (Polymer Source Inc., Dorval, Canada) which was dissolved in N, N-Dimethylformamide (Sigma-Aldrich, Inc., St. Louis, MO), spun-cast, and vacuum dried as described in our previous work [20]. FN from bovine plasma (Sigma-Aldrich, Inc., St. Louis, MO) was dissolved in 1X Phosphate-Buffered Saline (PBS) without calcium or magnesium (Invitrogen, Carlsbad, CA) for conductivity experiment. To study the effect of contour ions concentration on protein absorption, FN is dissolved in the PBS with different concentration (0.5X, 1X, 2X and 4X). Prepared SPS-coated wafers were incubated in the solutions of FN in PBS buffer (FN: 100 μg/ml) for four days at 37°C and 100% RH in 24-well dishes (BD, Franklin Lakes, NJ). After the self-assembled protein network formed, samples were rinsed three times with deionized (DI) water to remove the unabsorbed protein and salts in the PBS.

6.2.3 Scanning Probe Microscopy (SPM) and Shear Modulation Force Microscopy (SMFM)

The early-stage imaging and height measurements were made using a Dimension 3100 SPM (Veeco, Santa Barbara, CA) in contact mode with a silicon nitride tip (Veeco, Santa Barbara, CA). After the specific mineralization time point, the sample was rinsed twice by PBS and then immediately measured, in PBS, with scanning force microscopy in a 35 mm petri-dish (BD, Franklin Lakes, NJ). The fiber height was evaluated using SPM cross-sectional images by measuring fiber heights referenced to flat base regions as shown previously [20, 41]. Use of the SMFM to measure shear modulus response relies on lateral modulation of the cantilever buried ~3 nm deep into the sample, and measurement of the amplitude response, as detailed previously [74].

6.2.4 Protein Assay

The Bicinchoninic acid (BCA) protein assay kit (Sigma-Aldrich, Inc., St Louis, MO) was used to determine the quantity of adsorbed protein onto the surface. After incubation of FN onto the surface, surfaces were taken out of the incubator and washed 3 times with PBS to remove the unabsorbed protein. 500 µl of reagent was added to react with the adsorbed protein. The reagent-protein mixture was incubated for 2 hr at 37 ºC after which the reaction product between BCA and protein was removed and placed into wells of a 96-well dish. Spectrophotometric quantitation at 562 nm was obtained using a microplate reader (Model EL309 from Bio-Tek Instruments, Vermont). Six independent measurements were used for each sample. To determine the mass of adsorbed protein, we obtained a calibration curve for FN at concentration from 0 to 500 µg/ml.

6.2.5 Biomineralization

Samples were immersed in a metastable calcium phosphate solution which was prepared as follows: Salts were purchased from Mallinckrodt Baker Inc., Phillipsburg, NJ. Solutions were made in HEPES buffer, 1M, (Mediatech Inc., Manassas, VA) and diluted to 25 mM with DI water. NaCl solution (137 mM) in 25 mM HEPES buffer was prepared and the pH was adjusted to 7.4. $CaCl_2$ and Na_2HPO_4 stock solutions with the concentrations of 5.6 mM and 4 mM, respectively, were prepared separately in the above NaCl solution and the pH was readjusted to 7.4. Each of the stock solutions contained in addition 0.05 % (w/v) sodium azide (Sigma-Aldrich, Inc., St. Louis, MO) to avoid bacterial contamination. The metastable calcium phosphate solution was freshly prepared before use by rapidly mixing equal volumes of $CaCl_2$ and Na_2HPO_4 stock solutions. All the mineralization experiments were carried out at room

temperature, at which the solution is known to be metastable and does not precipitate mineral observed by SEM onto bare Silicon wafers or polymer films up to 28 days. After 28 days, samples were rinsed by DI water twice, air-dried overnight and stored in desiccators for further characterization by SEM and EDXS.

6.2.6 Scanning Electron Microscopy (SEM) and Energy Dispersive X-ray spectroscopy (EDXS)

SEM measurements (LEO1550, LEO, Germany) were conducted at the Center for Functional Nanomaterials, BNL. The morphology of crystals on the protein matrices after 28 days in calcium phosphate mineralization solution was investigated at 15 kV acceleration voltage and 4 mm working distance.

6.3 Results and Discussion

After 3-day incubation at 37°C, we compare the morphologies of the adsorbed proteins following incubation of an uncoated Si surface and one coated with a 5 nm layer of thermally evaporated Cr followed by 20 nm of Au. Both substrates are covered by identical spun cast films. As seen by SPM height imaging , FN self-assemble into fiber networks on SPS-coated silicon surface (Fig 6.3A), while only flat layer of FN is observed on SPS-coated Au surface (Fig 6.3B) even though the surface in contact with the protein was unchanged. To understand this phenomenon, we tested the SPS thin film by Neutron scattering. Our previous work demonstrated that SPS thin film is similar on Si and Au surface. Based on the same surface charge provided by SPS thin film, we proposed that the conductivity of substrate determines the dissipation of surface charge.

To investigate the effect of conductivity of substrates on protein absorption with SPS thin film coating, different Si wafers were chosen with a series of conductivity from 0.003 Ω·cm to 5000 Ω·cm. The morphology of FN absorbed onto the surfaces was investigated shown in Fig 6.4A. We found that when the conductivity of the substrate is no larger than 0.005 Ω·cm, similar to metals under ambient conditions, no fibers formed while the morphology of protein absorbed onto the surface is in globular shape. Whereas the protein absorbed onto the surface can self-assemble into fiber form with the resistivity of substrate is from 0.07 Ω·cm to 5000 Ω·cm shown in Fig 6.4A. To quantify the amount of protein absorbed on the surface, BCA assay was used to determine the absorbed FN shown in Fig 6.4B. The result shows that the absorbed FN mass is increasing with increasing the conductivity of the substrates. Hence even though the protein solutions were exposed to surfaces with covered with polymer films of identical the charges and chemical composition, the charge of the substrate determined the protein adsorption.

To better understand the process of protein absorption, we also changed the concentration of contour ions in protein solution by changing the concentration of buffer solution. The morphology of absorbed protein is shown in Fig 6.5A. The BCA data shown in Fig 6.5B indicate that the absorbed FN mass is decreasing with increasing the concentration of contour ions. Our results indicate that substrate image charges, possibly created by the approaching charged molecules, the dielectric constant of the polymer coating as well as concentration of contour ions can play a role in protein adsorption onto the surface.

Based on the above results, we can develop a novel method to patterning the protein onto the surface. We made patterned substrates, where an Au grating was imprinted onto Si surfaces by photolithography (see Fig 6.6). Separate grating were formed with spacing of 22 μm and 2.5 μm with the coating of SPS. The results showed unambiguously that only a single layer adsorbed

onto the areas where Au was underneath, and a much larger amount of protein was adsorbed onto the areas where Si was beneath the coating shown in Fig 6.4B. Control on SPS-coated Si wafer without any pattern was covered with standard protein network shown in Fig 6.7A. Furthermore, in the large areas, where the Si spacing exceeds 20 μm, the standard lattice was observed shown in Fig 6.7 B. As the Si area was decreased the lattice became progressively more distorted, till the protein from a sinusoidal like pattern and finally a single long fiber shown in Fig 6.7C. Since the mechanics of these fibers can be indicative of the protein conformation, we also measured the modulii as a function of the confining pattern dimension. We found that as the confinement became more severe the modulii of the fibers decreased, as shown in Fig 6.8, indicating that the internal organization of the fibrils may be different, when the intrinsic network is forced into a pattern smaller than its natural network dimension. We also studied the unusual sinusoidal pattern in more detail and mapped the modulus along the fiber. In contrast to the large fibers, where the modulii were nearly the same all along the fibers, in the case of the confined fibers, the straight sections were harder than the bent section.

The structural conformation of the fibronectin is essential in the properties of the protein. We had previous shown that only the fibrillar sections of FN are responsible for biomineralization [20] clearly differentiating between the structure of the flat and fibrillar regions. The patterned surfaces were also exposed of physiological biomineralizing solution as described preciously [74]. From the data shown in Fig 6.9 we see that biomineral deposits abruptly stop when the confinement becomes smaller than 10 μm, at which point the modulus also becomes smaller, indicating a change in conformation.

6.4 Conclusion

In conclusions we have demonstrated the critical nature of the electronic properties of the substrate on protein adsorption even in buried interfaces. The adsorbed amount of protein onto the SPS thin film is dominated by the resistivity of substrates and salt concentration. With increasing the resisitivity and decreasing of salt concentration, the adsorbed protein amount increases. Using this preservation we have successfully patterned regions with different protein conformation and biological function. Based on our results, we proposed that mechanism of protein adsorption could be related to the image charge and salt concentration.

Figures:

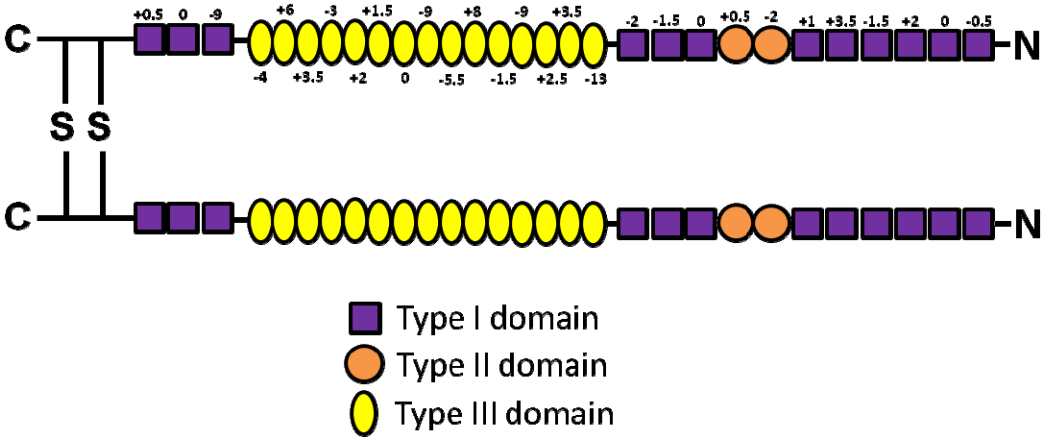

Figure 6.1 The schematic molecular structure of plasma fibronectin (FN). FN exists as a dimer composed of two nearly identical ~250 kDa subunits linked covalently near their C-termini by a pair of disulfide bonds. Each monomer consists of three types of repeating units: type I, type II and type III domains (12 type I domains, 2 type II domains and 15 type III domains) with net charge indicator for each module.

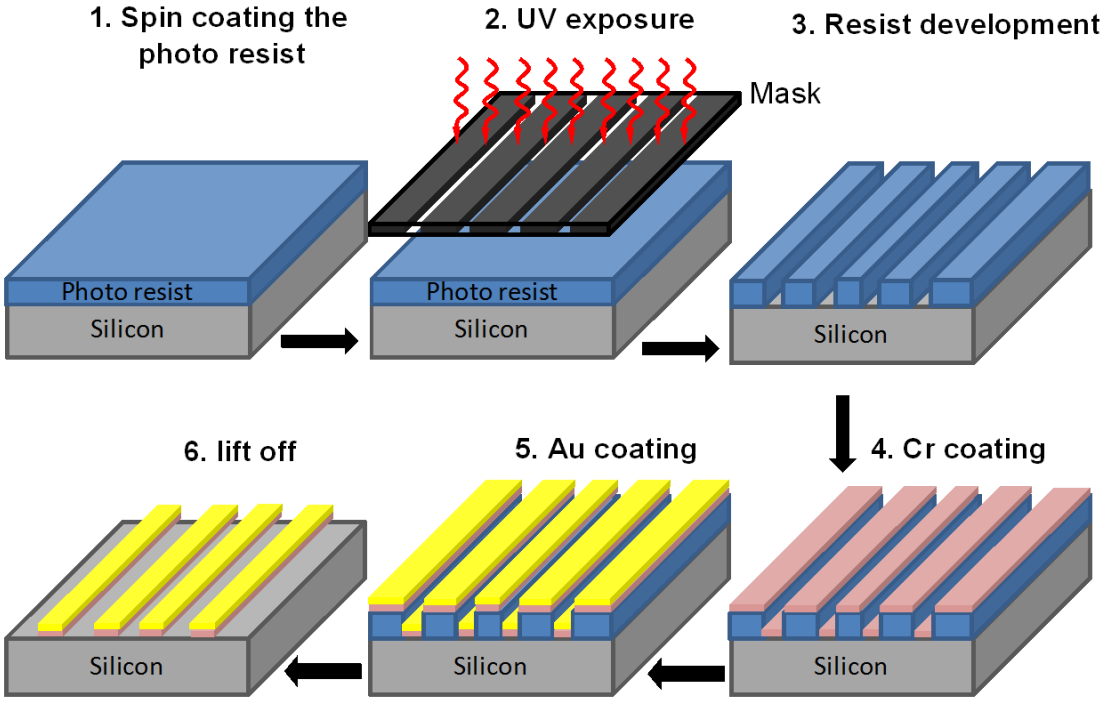

Figure 6.2 Schematic process of patterning.

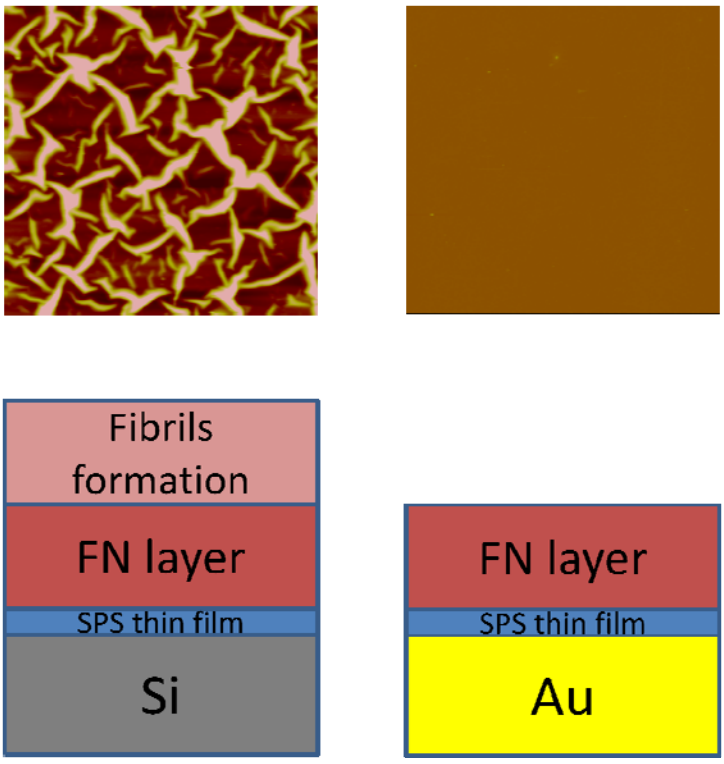

Figure 6.3 (A) Fibronectin on SPS-coated Silicon wafer. (B) Fibronectin on SPS-coated Au surface.

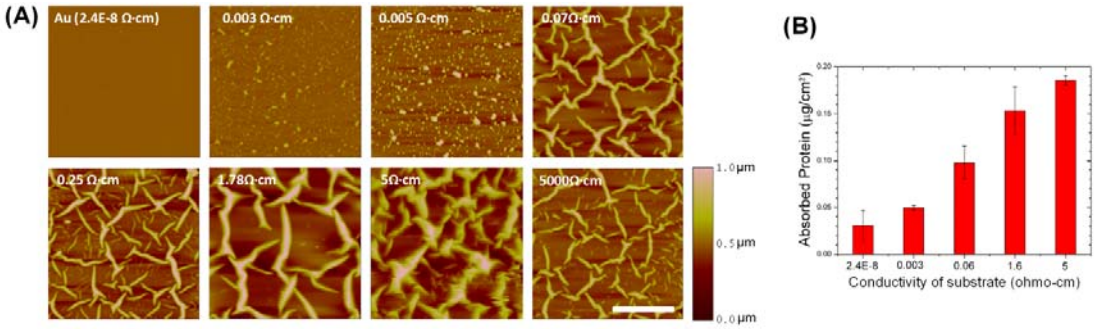

Figure 6.4 (A) Contact mode SPM topography images (50 μm×50 μm) of self-assembled fibronectin network on SPS-coated silicon wafer with different conductivity from 0.003 Ω·cm to 5000 Ω·cm. Scale bar = 20 μm. (B) Absorbed protein amount onto the substrates with different conductivity. The conductivity of Au is about 2.4×10^{8} from the reference.

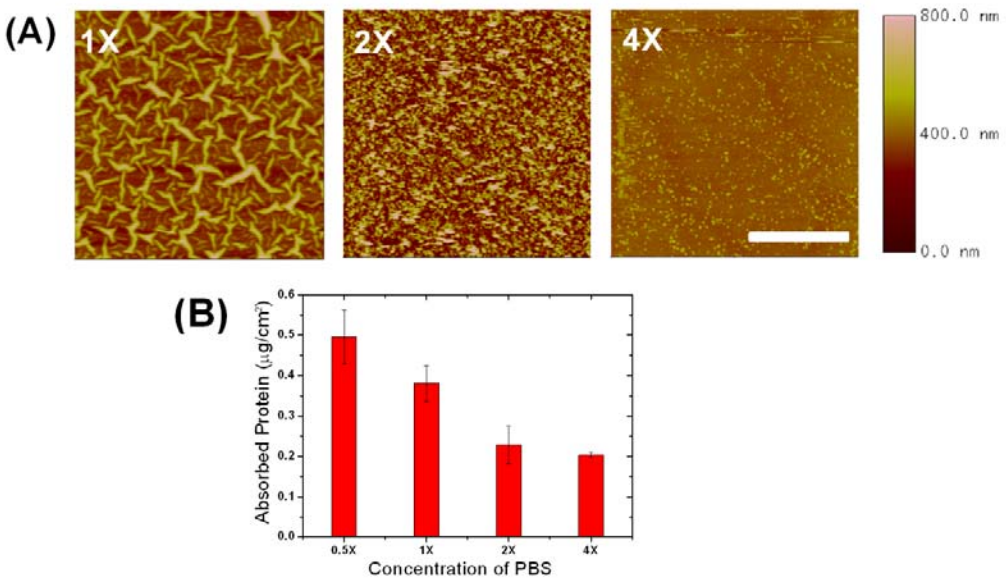

Figure 6.5 (A) Contact mode SPM topography images (50 μm×50 μm) of self-assembled fibronectin network on SPS-coated silicon wafer with different concentration of PBS. Scale bar = 20 μm. (B) Absorbed protein amount onto the substrates with different concentration of PBS.

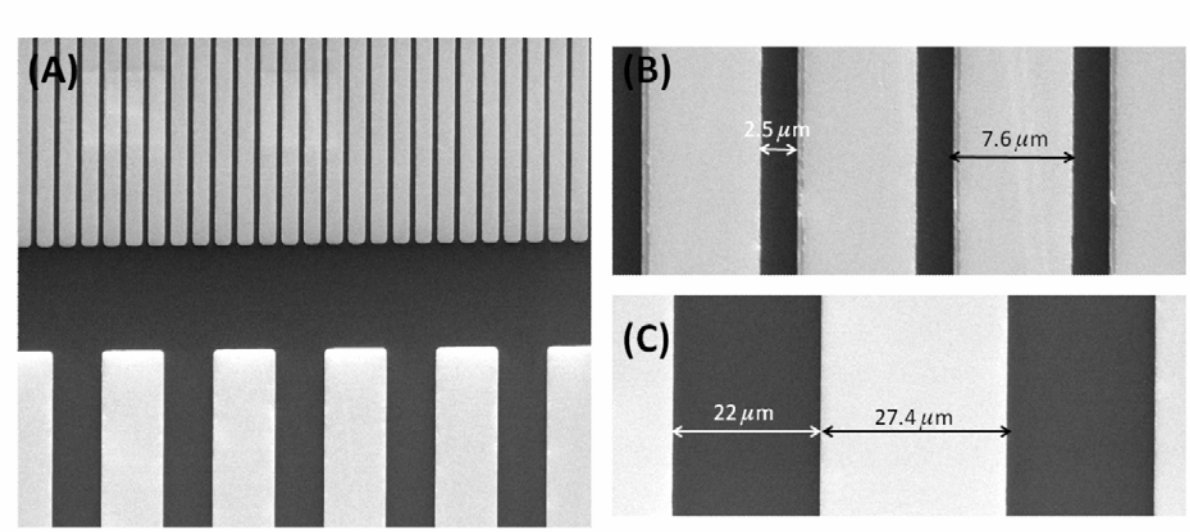

Figure 6.6 (A) Low magnification (×350) of SEM image of Si/Au gratings. High magnification (×3500) of SEM image of Si/Au gratings with (B) 2.5 μm of Si valley and 7.6 μm of Au hill; (C) 22 μm of Si valley and 27.4 μm hill.

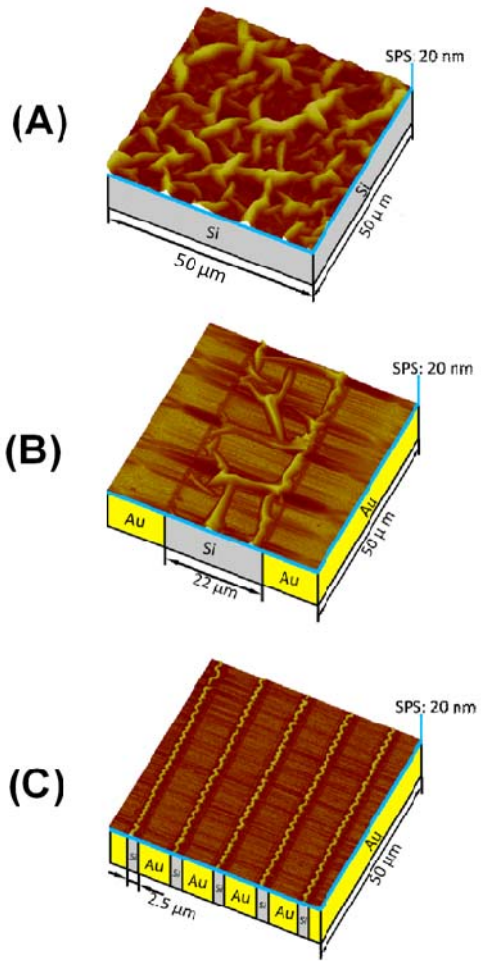

Figure 6.7 3D contact mode SPM topography images (50 µm×50 µm) of self-assembled fibronectin network on (A) SPS-coated silicon wafer without any pattern; (B) SPS-coated Si/Au gratings with 22 µm Si region; and (C) SPS-coated Si/Au gratings with 2.5 µm Si region

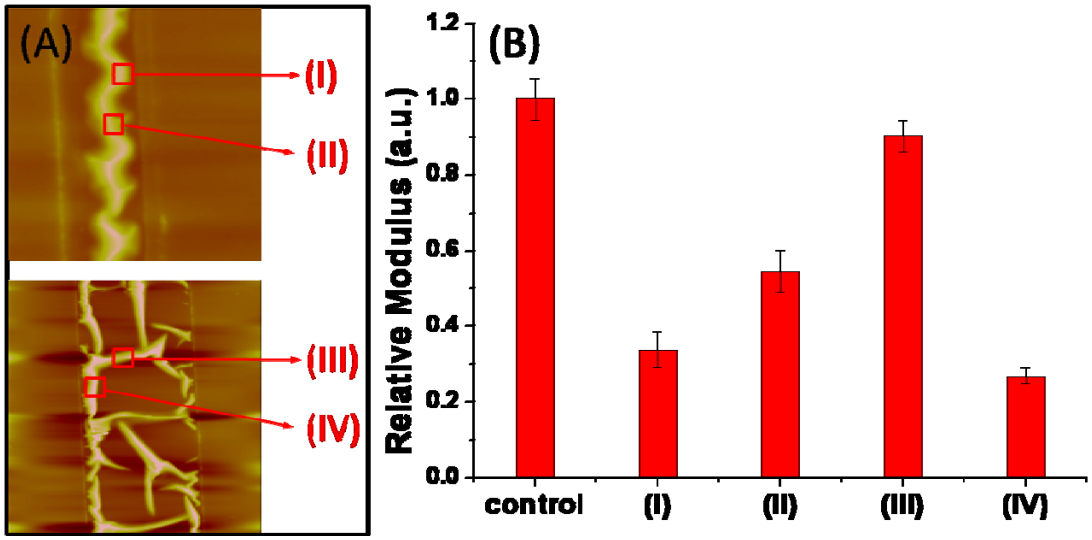

Figure 6.8 (A) 2D contact mode SPM topography images show the local positions of modulus measurements. (B) Relative moduli of protein fibers on different local positions. The protein fibers on Si without any confinement as control.

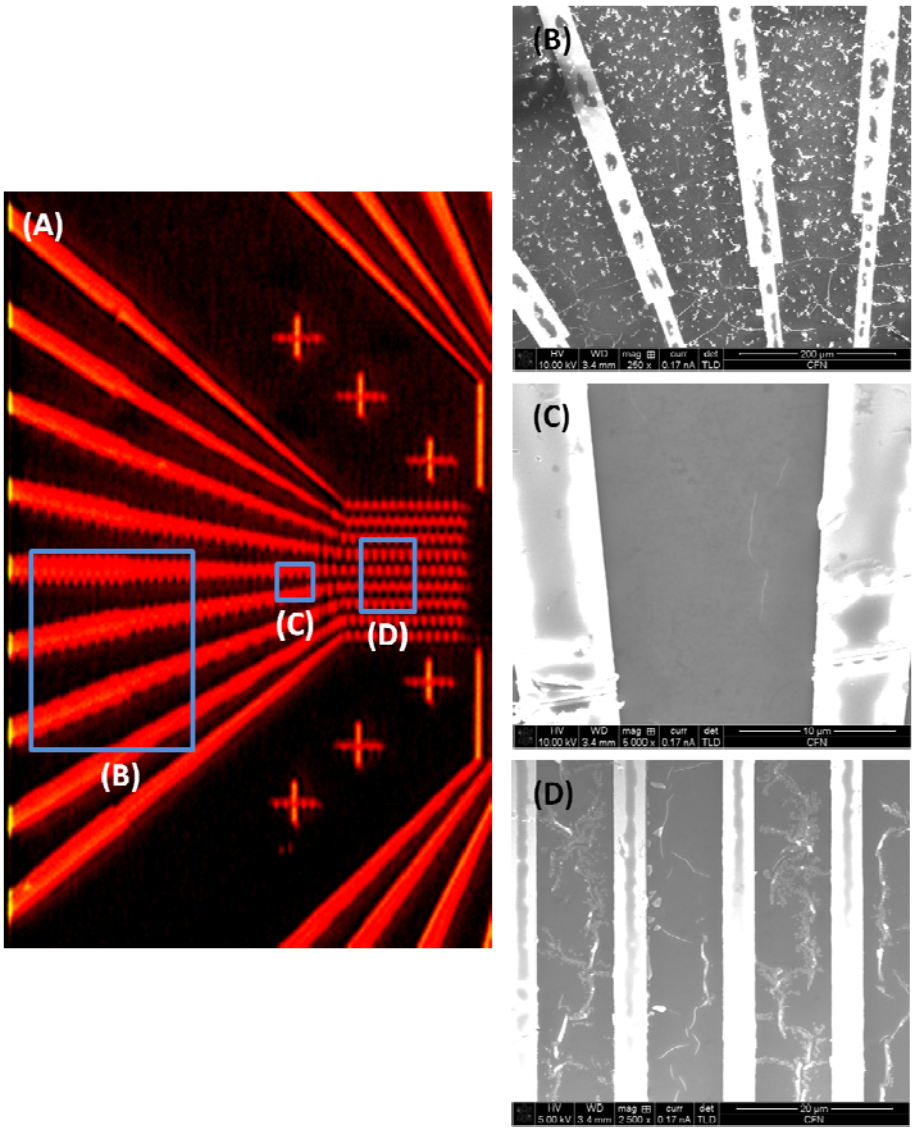

Figure 6.9 Biomineralization on the Au/Si pattern. Normal fiber in the big area can template the biomineral shown in (B). The disordered fiber in confine space can not template the biominerals shown in (C) and (D).

References:

1. Williams, D.F., *The Williams Dictionary of Biomaterials*. 1999, Liverpool University Press: Loverpool.

2. Vadgama, P., *Surface biocompatibility*, in *Annual Report on the Progress of Chemistry*. 2005. p. 14-52.

3. Schilick, S., ed. *Ionomers: characterization, theory, and applications*. 1996, CRC Press: Boca Raton.

4. Gebelein, C.G., ed. *Biomimetic Polymers*. 1990, Plenum Press: New York.

5. Macdonald, M., et al., *Release of a model protein from biodegradable self assembled films for surface delivery applications.* J Control Release, 2008. **131**(3): p. 228-34.

6. Kim, B.S., S.W. Park, and P.T. Hammond, *Hydrogen-bonding layer-by-layer-assembled biodegradable polymeric micelles as drug delivery vehicles from surfaces.* ACS Nano, 2008. **2**(2): p. 386-92.

7. Wood, K.C., et al., *Controlling interlayer diffusion to achieve sustained, multiagent delivery from layer-by-layer thin films.* Proc Natl Acad Sci U S A, 2006. **103**(27): p. 10207-12.

8. Balazs, A.C., C. Singh, and E. Zhulina, *Stabilizing properties of copolymers adsorbed on heterogeneous surfaces: A model for the interactions between a polymer-coated influenza virus and a cell.* Macromolecules, 1998. **31**(18): p. 6369-6379.

9. Ladam, G., et al., *Protein interactions with polyelectrolyte multilayers: interactions between human serum albumin and polystyrene sulfonate/polyallylamine multilayers.* Biomacromolecules, 2000. **1**(4): p. 674-87.

10. Boura, C., et al., *Endothelial cells grown on thin polyelectrolyte mutlilayered films: an evaluation of a new versatile surface modification.* Biomaterials, 2003. **24**(20): p. 3521-30.

11. Decher, G., *Fuzzy nanoassemblies: Toward layered polymeric multicomposites.* Science, 1997. **277**(5330): p. 1232-1237.

12. Gao, C.Y., et al., *Stability and mechanical properties of polyelectrolyte capsules obtained by stepwise assembly of poly(styrenesulfonate sodium salt) and poly(diallyldimethyl ammonium) chloride onto melamine resin particles.* Langmuir, 2001. **17**(11): p. 3491-3495.

13. Fleer, G.J., et al., *Polymer at Interfaces*. 1993, London: Chapman and Hall.

14. Park, S.Y., et al., *Anomalous adsorption of polyelectrolyte layers.* Macromolecules, 2001. **34**(10): p. 3384-3388.

15. Salloum, D.S. and J.B. Schlenoff, *Protein adsorption modalities on polyelectrolyte multilayers.* Biomacromolecules, 2004. **5**(3): p. 1089-96.

16. Pernodet, N., et al., *Fibronectin fibrillogenesis on sulfonated polystyrene surfaces.* Journal of Biomedical Materials Research Part A, 2003. **64A**(4): p. 684-692.

17. Meng, Y., et al., *Biomineralization of a Self-Assembled Extracellular Matrix for Bone Tissue Engineering.* Tissue Engineering Part A, 2009. **15**: p. 355-366.

18. Bauerlein, E., ed. *Biomineralization: From biology to biotechnology and medical application*. Second ed. 2004, WILEY-VCH: Weinheim.

19. Weiner, S. and L. Addadi, *Design strategies in mineralized biological materials.* Journal of Materials Chemistry, 1997. **7**(5): p. 689-702.

20. Subburaman, K., et al., *Templated biomineralization on self-assembled protein fibers.* Proceedings of the National Academy of Sciences of the United States of America, 2006. **103**(40): p. 14672-14677.

21. Mann, S., J.P. Hannington, and R.J.P. Williams, *Phospholipid-Vesicles as a Model System for Biomineralization.* Nature, 1986. **324**(6097): p. 565-567.

22. Archibald, D.D. and S. Mann, *Template Mineralization of Self-Assembled Anisotropic Lipid Microstructures.* Nature, 1993. **364**(6436): p. 430-433.

23. Stupp, S.I. and P.V. Braun, *Molecular manipulation of microstructures: Biomaterials, ceramics, and semiconductors.* Science, 1997. **277**(5330): p. 1242-1248.

24. Addadi, L. and S. Weiner, *Control and design principles in biological mineralization.* Angewandte Chemie-International Edition in English, 1992. **31**(2): p. 153-169.

25. Mann, S., *Biomineralization: the form(id)able part of bioinorganic chemistry!* Journal of the Chemical Society-Dalton Transactions, 1997(21): p. 3953-3961.

26. Aizenberg, J., A.J. Black, and G.M. Whitesides, *Control of crystal nucleation by patterned self-assembled monolayers.* Nature, 1999. **398**(6727): p. 495-498.

27. Travaille, A.M., et al., *Aligned growth of calcite crystals on a self-assembled monolayer.* Advanced Materials, 2002. **14**(7): p. 492-+.

28. Han, Y.J. and J. Aizenberg, *Face-selective nucleation of calcite on self-assembled monolayers of alkanethiols: Effect of the parity of the alkyl chain.* Angewandte Chemie-International Edition, 2003. **42**(31): p. 3668-3670.

29. Hutchens, S.A., et al., *Biomimetic synthesis of calcium-deficient hydroxyapatite in a natural hydrogel.* Biomaterials, 2006. **27**(26): p. 4661-4670.

30. Genge, B.R., L.N.Y. Wu, and R.E. Wuthier, *In vitro Modeling of matrix vesicle nucleation - Synergistic stimulation of mineral formation by annexin a5 and phosphatidylserine.* Journal of Biological Chemistry, 2007. **282**(36): p. 26035-26045.

31. He, G., et al., *Phosphorylation of phosphophoryn is crucial for its function as a mediator of biomineralization.* Journal of Biological Chemistry, 2005. **280**(39): p. 33109-33114.

32. Landis, W.J., F.H. Silver, and J.W. Freeman, *Collagen as a scaffold for biomimetic mineralization of vertebrate tissues.* Journal of Materials Chemistry, 2006. **16**(16): p. 1495-1503.

33. Kuther, J. and W. Tremel, *Template induced crystallization of biominerals on self-assembled monolayers of alkylthiols.* Thin Solid Films, 1998. **329**: p. 554-558.

34. Theobald, J.A., et al., *Controlling molecular deposition and layer structure with supramolecular surface assemblies.* Nature, 2003. **424**(6952): p. 1029-1031.

35. Shen, Q., et al., *Suspension effect of poly(styrene-ran-methacrylic acid) latex particles on crystal growth of calcium carbonate.* Crystal Growth & Design, 2005. **5**(4): p. 1387-1391.

36. Kwak, S.Y., et al., *Orientation and Mg incorporation of calcite grown on functionalized self-assembled monolayers: A synchrotron X-ray study.* Crystal Growth & Design, 2005. **5**(6): p. 2139-2145.

37. Zhang, L., et al., *Effects of crystalline phase on the biological properties of collagen-hydroxyapatite composites.* Acta Biomaterialia, 2010. **6**(6): p. 2189-2199.

38. Roveri, N., et al., *Biologically inspired growth of hydroxyapatite nanocrystals inside self-assembled collagen fibers.* Materials Science and Engineering: C, 2003. **23**(3): p. 441-446.

39. Gu, L.-s., et al., *Immobilization of a phosphonated analog of matrix phosphoproteins within cross-linked collagen as a templating mechanism for biomimetic mineralization.* Acta Biomaterialia, 2011. **7**(1): p. 268-277.

40. Kim, Y.K., et al., *Mineralisation of reconstituted collagen using polyvinylphosphonic acid/polyacrylic acid templating matrix protein analogues in the presence of calcium, phosphate and hydroxyl ions.* Biomaterials, 2010. **31**(25): p. 6618-6627.

41. Zhang, Y., et al., *Surface characterization of cross-linked elastomers by shear modulation force microscopy.* Polymer, 2003. **44**(11): p. 3327-3332.

42. Liu, Y., et al., *Wetting Behavior of Homopolymer Films on Chemically Similar Block-Copolymer Surfaces.* Physical Review Letters, 1994. **73**(3): p. 440-443.

43. Schinke, T., M.D. McKee, and G. Karsenty, *Extracellular matrix calcification: where is the action?* Nature Genetics, 1999. **21**(2): p. 150-151.

44. Luo, G., et al., *Spontaneous calcification of arteries and cartilage in mice lacking matrix GLA protein.* Nature, 1997. **386**(6620): p. 78-81.

45. Simionescu, A., D.T. Sirnionescu, and N.R. Vyavahare, *Osteogenic responses in fibroblasts activated by elastin degradation products and transforming growth factor-beta 1 - Role of*

myofibroblasts in vascular calcification. American Journal of Pathology, 2007. **171**(1): p. 116-123.

46. Pankov, R. and K.M. Yamada, *Fibronectin at a glance.* J Cell Sci, 2002. **115**(Pt 20): p. 3861-3.

47. Weiss, R.E. and A.H. Reddi, *Appearance of fibronectin during the differentiation of cartilage, bone, and bone-Marrow.* Journal of Cell Biology, 1981. **88**(3): p. 630-636.

48. Pellenc, D., H. Berry, and O. Gallet, *Adsorption-induced fibronectin aggregation and fibrillogenesis.* Journal of Colloid and Interface Science, 2006. **298**(1): p. 132-144.

49. Couchourel, D., et al., *Effects of fibronectin on hydroxyapatite formation.* Journal of Inorganic Biochemistry, 1999. **73**(3): p. 129-136.

50. Watson, K.E., et al., *Fibronectin and collagen I matrixes promote calcification of vascular cells in vitro, whereas collagen IV matrix is inhibitory.* Arteriosclerosis Thrombosis and Vascular Biology, 1998. **18**(2): p. 1964-1971.

51. Religa, P., et al., *Arteriosclerosis in rat aortic allografts: Dynamics of cell growth, apoptosis and expression of extracellular matrix proteins.* Molecular and Cellular Biochemistry, 2003. **249**(1-2): p. 75-83.

52. Merx, M.W., et al., *Myocardial stiffness, cardiac remodeling, and diastolic dysfunction in calcification-prone fetuin-A-deficient mice.* Journal of the American Society of Nephrology, 2005. **16**(11): p. 3357-3364.

53. Hai-Tao Ding, C.-G.W., Tian-Lan Zhang, Kui Wang,, *Fibronectin enhances in vitro vascular calcification by promoting osteoblastic differentiation of vascular smooth muscle cells via ERK pathway.* Journal of Cellular Biochemistry, 2006. **99**(5): p. 1343-1352.

54. Morla, A.O. and J.E. Mogford, *Control of smooth muscle cell proliferation and phenotype by integrin signaling through focal adhesion kinase.* Biochemical and Biophysical Research Communications, 2000. **272**(1): p. 298-302.

55. Bouvet, C., et al., *Sequential activation of matrix metalloproteinase 9 and transforming growth factor beta in arterial elastocalcinosis.* Arteriosclerosis Thrombosis and Vascular Biology, 2008. **28**(5): p. 856-862.

56. Daamen, W.F., et al., *A biomaterial composed of collagen and solubilized elastin enhances angiogenesis and elastic fiber formation without calcification.* Tissue Engineering Part A, 2008. **14**(3): p. 349-360.

57. Sikiric, M.D., et al., *Biomimetic organic-inorganic nanocomposite coatings for titanium implants: I. preparation, physicochemical and mechanical characterization.* Key Engineering Materials, 2007. **330-332**: p. 389-392.

58. Ma, Y., et al., *High-resolution K-shell photoabsorption measurements of simple molecules.* Physical Review A, 1991. **44**(3): p. 1848-1858.

59. Benzerara, K., et al. *Search for microbial signatures within human and microbial calcifications using soft X-ray spectromicroscopy*. 2006: Journal of Investigative Medicine.

60. Benzerara, K., et al., *Scanning transmission X-ray microscopy study of microbial calcification.* Geobiology, 2004. **2**(4): p. 249-259.

61. Kuhn, L.T., et al., *Structure, composition, and maturation of newly deposited calcium-phosphate crystals in chicken osteoblast cell cultures.* Journal of Bone and Mineral Research, 2000. **15**(7): p. 1301-1309.

62. Fanelli, C., Coppola, S., Barone, R., Colussi, C., Gualandi, G., Volpe P. and Ghibelli L., *Magnetic fields increase cell survival by inhibiting apoptosis via modulation of Ca2+ influx.* The Journal of the Federation of American Societies for Experimental Biology, 1999. **13**(1): p. 95-102.

63. Lowenstam, H.A. and S. Weiner, in *Biomineralization and biological metal accumulation*, P. Westbroek and E.W. De Jong, Editors. 1983, D. Reidel Publishing Company. p. 191.

64. Glimcher, M.J., *Recent studies of the mineral phase in bone and its possible linkage to the organic matrix by protein-bound phosphate bonds.* Philos Trans R Soc Lond B Biol Sci, 1984. **304**(1121): p. 479-508.

65. Ng, S.P., et al., *Designing an extracellular matrix protein with enhanced mechanical stability.* Proceedings of the National Academy of Sciences of the United States of America, 2007. **104**(23): p. 9633-9637.

66. Lowenstam, H.A., *Minerals formed by organisms.* Science, 1981. **211**(4487): p. 1126-31.

67. LeGeros, R.Z., *Calcium phosphates in oral biology and medicine*. Vol. 15. 1991, Basel: Karger.

68. Aoba, T., *Solubility properties of human tooth mineral and pathogenesis of dental caries.* Oral Diseases, 2004. **10**(5): p. 249-257.

69. Daculsi, G., J.M. Bouler, and R.Z. LeGeros, *Adaptive Crystal Formation in Normal and Pathological Calcifications in Synthetic Calcium Phosphate and Related Biomaterials*, in *International Review of Cytology*, W.J. Kwang, Editor. 1997, Academic Press. p. 129-191.

70. Finke, M., K.D. Jandt, and D.M. Parker, *The Early Stages of Native Enamel Dissolution Studied with Atomic Force Microscopy.* Journal of Colloid and Interface Science, 2000. **232**(1): p. 156-164.

71. Gilbert, P.U.P.A., M. Abrecht, and B.H. Frazer, *The organic-mineral interface in biominerals.* Molecular Geomicrobiology, 2005. **59**: p. 157-185.

72. Metzler, R.A., et al., *Probing the organic-mineral interface (OMI) at the molecular level in model biominerals.* Geochimica Et Cosmochimica Acta, 2007. **71**(15): p. A658-A658.

73. Metzler, R.A., et al., *Probing the organic-mineral interface at the molecular level in model biominerals.* Langmuir, 2008. **24**(6): p. 2680-2687.

74. Ba, X., et al., *Complementary effects of multi-protein components on biomineralization in vitro.* Journal of Structural Biology, 2010. **170**(1): p. 83-92.

75. Feser, M., et al., *Instrumentation Advances and Detector Development with the Stony Brook Scanning Transmission X-ray Microscope in X-ray Microscopy.* 2000: p. 367-372.

76. Jacobsen, C.B., T.; Feser, M.; Osanna, A.; Stein, A.; Wirick, S., *Spectromicroscopy of Biological and Environmental Systems at Stony Brook: Instrumentation and Analysis.* Surface Review and Letters, 2002. **9**(1): p. 185-191.

77. Zhang, X., et al., *Mapping and measuring DNA to protein ratios in mammalian sperm head by XANES imaging.* Journal of Structural Biology, 1996. **116**(3): p. 335-44.

78. Rothe, J., M. Plaschke, and M.A. Denecke, *Scanning transmission X-ray microscopy as a speciation tool for natural organic molecules.* Radiochimica Acta, 2004. **92**(9-11): p. 711-715.

79. Abramson, L., et al., *The use of soft X-ray spectromicroscopy to investigate the distribution and composition of organic matter in a diatom frustule and a biomimetic analog.* Deep-Sea Research Part Ii-Topical Studies in Oceanography, 2009. **56**(18): p. 1369-1380.

80. Netz, R.R. and J.F. Joanny, *Complexation behavior of polyampholytes and charged objects.* Macromolecules, 1998. **31**(15): p. 5123-5141.

81. Dobrynin, A.V., S.P. Obukhov, and M. Rubinstein, *Long-range multichain adsorption of polyampholytes on a charged surface.* Macromolecules, 1999. **32**(17): p. 5689-5700.

82. de Groot, F.M.F., et al., *L2,3 x-ray-absorption edges of d compounds: K+, Ca2+, Sc3+, and Ti4+ in Oh (octahedral) symmetry.* Physical Review B, 1990. **41**(2): p. 928.

83. Naftel, S.J., et al., *Calcium L-edge XANES study of some calcium compounds.* Journal of Synchrotron Radiation, 2001. **8**: p. 255- 257.

84. Francis, J.T. and A.P. Hitchcock, *Inner-Shell Spectroscopy of Para-Benzoquinone, Hydroquinone, and Phenol - Distinguishing Quinoid and Benzenoid Structures.* Journal of Physical Chemistry, 1992. **96**(16): p. 6598-6610.

85. Hitchcock, A.P., S.G. Urquhart, and E.G. Rightor, *Inner-Shell Spectroscopy of Benzaldehyde, Terephthalaldehyde, Ethyl Benzoate, Terephthaloyl Chloride, and Phosgene - Models for Core Excitation of Poly(Ethylene-Terephthalate).* Journal of Physical Chemistry, 1992. **96**(22): p. 8736-8750.

86. Hitchcock, A.P., et al., *Carbon K-Shell Excitation of Gaseous and Condensed Cyclic Hydrocarbons - C3h6, C4h8, C5h8, C5h10, C6h10, C6h12, and C8h8.* Journal of Chemical Physics, 1986. **85**(9): p. 4849-4862.

87. Urquhart, S.G. and H. Ade, *Trends in the carbonyl core (C 1s, O 1s) -> pi*c=o transition in the near-edge X-ray absorption fine structure spectra of organic molecules.* Journal of Physical Chemistry B, 2002. **106**(34): p. 8531-8538.

88. Boskey, A.L., *Biomineralization: An overview.* Connective Tissue Research, 2003. **44**: p. 5-9.

89. Boskey, A.L. *Matrix proteins and mineralization: An overview*. 1996: Gordon Breach Sci Publ Ltd.

90. Lowenstam, H.A. and S. Weiner, *Biomineralization and biological metal accumulation*, P.a.D.J. Westbroek, E. W. , Editor. 1983, D. Reidel Publishing Company: Dordrecht. p. 191.

91. Veis, A., *A window on biomineralization.* Science, 2005. **307**(5714): p. 1419-1420.

92. McKee, M.D., W.N. Addison, and M.T. Kaartinen, *Hierarchies of extracellular matrix and mineral organization in bone of the craniofacial complex and skeleton.* Cells Tissues Organs, 2005. **181**(3-4): p. 176-188.

93. Weiner, S. and W. Traub, *Macromolecules in Mollusk Shells and Their Functions in Biomineralization.* Philosophical Transactions of the Royal Society of London Series B-Biological Sciences, 1984. **304**(1121): p. 425-&.

94. Knott, L. and A.J. Bailey, *Collagen cross-links in mineralizing tissues: A review of their chemistry, function, and clinical relevance.* Bone, 1998. **22**(3): p. 181-187.

95. Orgel, J.P.R.O., et al., *Microfibrillar Structure of Type I Collagen in situ.* Proceedings of the National Academy of Sciences of the United States of America, 2006. **103**(24): p. 9001-9005.

96. Velling, T., et al., *Polymerization of type I and III collagens is dependent on fibronectin and enhanced by integrins alpha 11beta 1 and alpha 2beta 1.* J Biol Chem, 2002. **277**(40): p. 37377-81.

97. Fratzl, P., et al., *Nucleation and Growth of Mineral Crystals in Bone Studied by Small-Angle X-Ray-Scattering.* Calcified Tissue International, 1991. **48**(6): p. 407-413.

98. Traub, W., T. Arad, and S. Weiner, *Origin of Mineral Crystal-Growth in Collagen Fibrils.* Matrix, 1992. **12**(4): p. 251-255.

99. Robinson, R.A., *An electron-microscopic study of the crystalline inorganic component of bone and its relationship to the organic matrix.* Journal of Bone and Joint Surgery-American Volume, 1952. **34-A**(2): p. 389-435; passim.

100. Glimcher, M.J., *Mechanism of calcification: role of collagen fibrils and collagen-phosphoprotein complexes in vitro and in vivo.* Anat Rec, 1989. **224**(2): p. 139-53.

101. Veis, A. and A. Perry, *Phosphoprotein of Dentin Matrix.* Biochemistry, 1967. **6**(8): p. 2409-&.

102. Gajjeraman, S., et al., *Matrix macromolecules in hard tissues control the nucleation and hierarchical assembly of hydroxyapatite.* Journal of Biological Chemistry, 2007. **282**(2): p. 1193-1204.

103. Rusu, V.M., et al., *Size-controlled hydroxyapatite nanoparticles as self-organized organic-inorganic composite materials.* Biomaterials, 2005. **26**(26): p. 5414-5426.

104. Danilchenko, S.N., et al., *Determination of the bone mineral crystallite size and lattice strain from diffraction line broadening.* Crystal Research and Technology, 2002. **37**(11): p. 1234-1240.

105. Yan, Q.C., N. Tomita, and Y. Ikada, *Effects of static magnetic field on bone formation of rat femurs.* Med Eng Phys, 1998. **20**(6): p. 397-402.

106. Degen, I.L. and V.I. Stetsula, *Consolidation of bone fragments in a constant magnetic field.* Ortopediia Travmatologiia Protezirovanie, 1971. **32**(9): p. 45-8.

107. Bruce, J.N., et al., *Vascular permeability induced by protein product of malignant brain tumors: inhibition by dexamethasone.* Journal of Neurosurgery, 1987. **67**(6): p. 880-4.

108. Kim, H.J., et al., *Effect of magnetic field on the fibronectin adsorption, cell attachment and proliferation on titanium surface.* Clinical Oral Implants Research, 2005. **16**(5): p. 557-62.

109. Ross, S.M., *Combined DC and ELF magnetic fields can alter cell proliferation.* Bioelectromagnetics, 1990. **11**(1): p. 27-36.

110. Hashimoto, Y., M. Kawasumi, and M. Saito, *Effect of Static Magnetic Field on Cell Migration.* Electrical Engineering in Japan, 2007. **160**(2): p. 46-52.

111. Kotani, H., et al., *Strong static magnetic field stimulates bone formation to a definite orientation in vitro and in vivo.* Journal of Bone Mineral Research, 2002. **17**(10): p. 1814-21.

112. Lyle, D.B., et al., *Intracellular calcium signaling by Jurkat T-lymphocytes exposed to a 60 Hz magnetic field.* Bioelectromagnetics, 1997. **18**(6): p. 439-45.

113. Rosen, A.D., *Mechanism of action of moderate-intensity static magnetic fields on biological systems.* Cell Biochem Biophys, 2003. **39**(2): p. 163-73.

114. Rosen, A.D., *Membrane response to static magnetic fields: effect of exposure duration.* Biochimica et Biophysica Acta, 1993. **1148**(2): p. 317-20.

115. Subburaman, K., et al., *Templated biomineralization on self-assembled protein fibers.* Proc Natl Acad Sci U S A, 2006. **103**(40): p. 14672-7.

116. Camilleri, S. and F. McDonald, *Static magnetic field effects on the sagittal suture in Rattus Norvegicus.* American Journal of Orthodontics and Dentofacial Orthopedics, 1993. **103**(3): p. 240-246.

117. Saifzadeh, S.H., R.; Shokouhi Sabet Jalali, F. and Kabiri, B., *Effect of a static magnetic field on bone healing in the dog: radiographic and histopathological studies.* Iranian Journal of Veterinary Research, Univeristy of Shiraz, 2007. **8**(1): p. 8-15.

118. Meng, Y., et al., *Biomineralization of a self-assembled extracellular matrix for bone tissue engineering.* Tissue Engineering: Part A, 2009. **15**(2): p. 355-66.

119. Rubin, E. and J.L. Farber, *Pathology*. Second ed. 1994, Philadelphia: J.B. Lippincott Co.

120. Ba, X., et al., *Complementary effects of multi-protein components on biomineralization in vitro.* J Struct Biol, 2010. **170**(1): p. 83-92.

121. Yamamoto, Y., et al., *Effects of Static Magnetic Fields on Bone Formation in Rat Osteoblast Cultures.* Journal of Dental Research, 2003. **82**(12): p. 962-966.

122. Sivaraman, B., K.P. Fears, and R.A. Latour, *Investigation of the effects of surface chemistry and solution concentration on the conformation of adsorbed proteins using an improved circular dichroism method.* Langmuir, 2009. **25**(5): p. 3050-6.

123. Clarke, M.L., J. Wang, and Z. Chen, *Conformational changes of fibrinogen after adsorption.* J Phys Chem B, 2005. **109**(46): p. 22027-35.

124. Schwinte, P., et al., *Secondary structure of proteins adsorbed onto or embedded in polyelectrolyte multilayers.* Biomacromolecules, 2002. **3**(6): p. 1135-43.

125. Erickson, H.P., *Stretching fibronectin.* J Muscle Res Cell Motil, 2002. **23**(5-6): p. 575-80.

126. Dzamba, B.J. and D.M. Peters, *Arrangement of cellular fibronectin in noncollagenous fibrils in human fibroblast cultures.* J Cell Sci, 1991. **100 (Pt 3)**: p. 605-12.

127. Furcht, L.T., et al., *Fibronectin Presence in Native Collagen Fibrils of Human-Fibroblasts - Immunoperoxidase and Immunoferritin Localization.* Journal of Histochemistry & Cytochemistry, 1980. **28**(12): p. 1319-1333.

128. Veiseh, M., et al., *Guided cell patterning on gold-silicon dioxide substrates by surface molecular engineering.* Biomaterials, 2004. **25**(16): p. 3315-3324.

129. Lee, C.-S., et al., *Protein patterning on silicon-based surface using background hydrophobic thin film.* Biosensors and Bioelectronics, 2003. **18**(4): p. 437-444.

130. Malmstrom, J., et al., *Large area protein patterning reveals nanoscale control of focal adhesion development.* Nano Lett, 2010. **10**(2): p. 686-94.

131. Kim, K., et al., *Protein patterning based on electrochemical activation of bioinactive surfaces with hydroquinone-caged biotin.* J Am Chem Soc, 2004. **126**(47): p. 15368-9.

Appendix A:

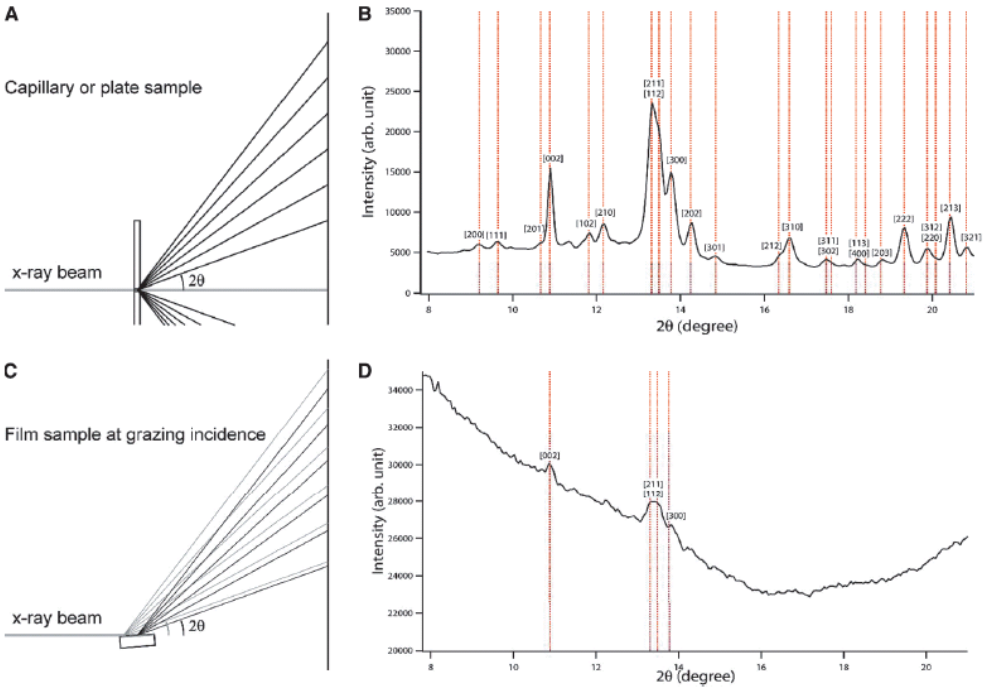

SUPPLEMENTAL FIG. 4. To demonstrate the difference in X-ray scattering between a powder sample in a glass capillary versus a thin film sample (as in the case of our cultured cells that were dried on SPS-coated Si), we here show schemes depicting the scattering and detector geometry along with experimental data from these two systems. The X-ray wavelength is 0.65255Å.In a transmission X-ray diffraction measurement from a capillary containing a powder sample of synthetic HAP (A), scattering from a very small volume is collected on an area detector screen, depicted by the plane at the right. After calibration with an alumina powder standard, the relationship between position of detected intensity on the detector and scattering angle 2y is known. The HAP powder peaks are broader than those of the standard, and allow us to estimate a particle size of 25 nm, as opposed to 33nm or greater for the resolution limited standard. The indexed experimental HAP powder data from the capillary are azimuthally averaged over the area detector and shown with Bragg peak indices in (B). Our synchrotron GIXD setup, appropriate for thin film samples, is illustrated in (C). The grazing angle prevents excessive background scattering from the substrate by minimizing bulk X-ray penetration. The illuminated spot extends to nearly the full length of the sample due to the finite X-ray beam height: in this case, the 0.25-mm-high beam incident at 18 creates an illuminated stripe 14-mm long, which illuminates as much of our very small sample volume as possible. The offset of the origin of the scattering causes the diffracted beams to hit the detector in a position displaced from the nominal, which appears as a broadening of the peaks when analyzed [see light and heavy rays in (C)]. The experimental diffraction pattern in (D) is of the same commercial HAP powder as (B), but dusted onto a blank SPS–Si wafer. There is an enormous scattering background from the polymer material, and the very thin powder coating shows only the strongest Bragg peaks, the [002] and the [211]/[112] that slightly overlap each other and the [300]. The geometry-induced broadening suggests a particle size of 12 nm, but this is a lower bound since the higher-resolution capillary measurement tells us that the particles are of order 25 nm. This type of thin-film diffraction pattern is what we have access to, for the tiny particles deposited on the surfaces by our mineralizing osteoblasts after at least 14 days of incubation in osteogenic medium. Hence our reported particle sizes in the manuscript represent a lower bound, and can only by analyzed at the well-separated [002] peak.